Electron Acceleration in Ultraintense Laser Pulse Interaction with Solid Targets

Inaugural-Dissertation

zur Erlangung des Doktorgrades
der Mathematisch-Naturwissenschaftichen Fakultät
der Heinrich-Heine-Universität Düsseldorf

vorgelegt von

Xiaoming Zhu

aus Jiangsu (China)

Düsseldorf, March 2017

Aus dem Institut für Laser- und Plasmaphysik
der Heinrich-Heine-Universität Düsseldorf

Gedruckt mit der Genehmigung der
Mathematisch-Naturwissenschaftlichen Fakultät der
Heinrich-Heine-Universität Düsseldorf

1. Gutachter: Prof. Dr. O. Willi

2. Gutachter: Prof. Dr. A. Pukhov

Tag der mündlichen Prüfung: to be decided

Abstract

The interaction of ultra-shot, high-intensity laser pulses with solid targets is an active topic of intensive theoretical and experimental studies in recent decades. Dense and collimated fast electron beams generated by laser-solid interactions are desired for a variety of applications including the fast-ignitior approach in inertial confinement fusion, ultra-short x-ray sources and ion acceleration. Modulations of target surface are an efficient method to improve the acceleration and collimation of the surface fast electrons. In this dissertation, the electron acceleration of grating targets with different groove spacings (double-, close- and sub-wavelength) irradiated by superintense ($\sim 2 \times 10^{20}\mathrm{W/cm^2}$), ultrashort ($\sim 28$ fs), high contrast (prepulse-to-pulse $\approx 10^{-11}$) laser pulses were investigated and compared with those of the flat mirror targets. An enhancement by a factor of 3.5 of the fast electron flux emitted along the grating surface direction with a modulation wavelength in the order of the laser wavelength was observed compared to the flat mirror target. The experimental results of double-wavelength gratings demonstrate the excitation of the surface plasma waves (SPWs) in the relativistic regime.

The angular distribution and energy spectra of fast electrons generated by thin foil targets were also investigated at normal and oblique incidence. The efficiency of the fast electron acceleration is strongly dependent on the target thickness and the laser incidence angle. The effective electron temperature decreases with the thickness of the targets for both cases, high and low contrast laser pulse.

The efficiency of the laser energy absorption by various types of targets was investigated and different kinds of target modulation were considered. The results are in agreement with the electron acceleration investigations. The optimal angle of incidence for energy absorption by grating targets is 45°, different from the flat targets of which the absorbed energy increases with the laser incidence angle.

The experimental results were compared with 2D simulations using EPOCH Particle-in-Cell code. Excellent agreement with the experimental data was found for the electron acceleration and absorption processes. An analytical model was developed to interpret the resonant angle shifting and non-linear effects of preplasma in SPWs excitation mechanism.

Zusammenfassung

Die Interaktion von ultrakurzen, hochintensiven Laserpulsen mit einem Festkörper-Target ist ein aktives Thema intensiver theoretischer und experimenteller Studien des letzen Jahrzehnts. Dichte, kollimierte, schnelle Elektronen, die bei der Interaktion entstehen sind für eine Vielzahl von Anwendungen von Bedeutung, zum Beispiel bei der Trägheitsfusion, ultrakurzen Röntgenquellen und der Ionenbeschleunigung. Die schnelle Zündung bei der Trägheitsfusion ist ein vielversprechendes Schema, bei dem die Fusionsreaktionen durch relativistische Elektronen, die durch einen superintensiven Laserpuls beschleunigt werden, ausgelöst werden. Eine Modulation in der Target Oberflächenstruktur ist ein effizientes Verfahren um sowohl die Beschleunigung als auch die Kollimation der schnellen Oberflächenelektronen zu verbessern. In dieser Arbeit wurde die Elektronenbeschleunigung von Gittern mit unterschiedlichen Rillenabständen (Doppel-, Nah- und Sub-Wellenlänge) mit der von flachen Spiegel-Targets verglichen. Dazu wurden die unterschiedlichen Targets mit hochintensiven ($\sim 2 \times 10^{20}$W/cm^2), ultrakurzen ($\sim$28 fs) (Prepuls-to-Puls$\approx 10^{-11}$) Laserpulsen beschossen. Es konnte ein Anstieg des Elektronenflusses entlang der Oberfläche des Nah-Wellenlängengitters um den Faktor 3,5 im Vergleich zu den flachen Spiegel-Targets beobachtet werden. Die Resultate der Doppel-Wellenlängengitter zeigen eine Anregung der Oberflächenplasmawellen (engl. Abkürzung SPWs) im relativistischen Regime.

Die Winkelverteilung und die Energiespektren von schnellen Elektronen, die durch Beschuss dünner Folien erzeugt wurden, wurden sowohl unter schrägem Lasereinfall als auch unter Einfall normal zur Target Oberfläche untersucht. Die Effizienz der schnellen Elektronenbeschleunigung hängt stark von der Targetdicke und dem Lasereinfallswinkel ab. Die effektive Elektronentemperatur sinkt mit der Targetdicke sowohl bei hohem als auch bei niedrigem Laserpulskontrast.

Die Absorptionseffizienz von Laserenergie in verschiedenen Target Typen wurde untersucht, dabei wurden unterschiedliche Arten von Target Modulationen berücksichtigt. Die Ergebnisse stimmen mit den Untersuchungen zur Elektronenbeschleunigung überein. Der optimale Einfallswinkel für die Energieabsorption durch Gittertargets beträgt 45°, anders als bei den flachen Targets, deren absorbierte Energie mit dem Lasereinfallswinkel ansteigt.

Die experimentellen Ergebnisse wurden mit 2D-Simulationen unter Verwendung des EPOCH Particle-in-Cell-Codes verglichen. Exzellente Übereinstimmung mit den experimentellen Daten für die Elektronenbeschleunigung und die Absorptionsprozesse wurde gefunden. Ein analytisches Modell wurde entwickelt, um die Resonanzwinkelverschiebung und die nichtlinearen Effekte vom sogenannten Pre-Plasma im SPW-Anregungsmechanismus zu interpretieren.

Contents

Chapter 1

Introduction

Highly collimated energetic electrons generated by an ultrashort ($\tau \leq 100\text{fs}$), high intensity ($I \geq 10^{18}\text{W/cm}^2$) laser pulse interacting with solid targets have attracted tremendous attention due to their potential applications, such as the fast ignition (FI) of inertial confinement fusion (ICF) [1, 2], laser driven high energy ion acceleration[3–8], ultrashort x-ray sources [9, 10], etc. There are specific requirements on the fast electron energy spectrum, the directionality and the energy conversion efficiency for each application. The concept of fast ignition uses a collimated fast electron beam which is accelerated by a relativistic laser pulse to trigger fusion reactions in inertial confinement fusion. For the study of the electron acceleration mechanisms, the conversion efficiency of laser energy coupling to fast electrons, the mean temperature and angular distribution of fast electrons are essential for optimizing the fast ignitor scheme.

The subject of this dissertation is the study of electron acceleration during the interaction of high-intensity ($I \geq 10^{20}\text{W/cm}^2$), ultra-short ($\tau \approx 28$ fs) laser pulses with solid matter. The work aims to investigate and characterize electrons generated on the target surface and to improve the efficiency and quality of fast electron beams to achieve the requirements of fast ignition. The recent development of ultrashort high power laser systems opens opportunities for such experimental investigations.

High efficiency of energy conversation from the incident laser to hot electrons is highly desirable in many applications. In the interacting process of a relativistic oblique laser pulse with a solid target, fast electrons originating from either $\boldsymbol{j} \times \mathbf{B}$ heating [11] or vacuum heating induce the quasistatic magnetic and electric fields which in turn accelerate the hot electrons and confine them along the target surface. This self-sustained surface acceleration process results in the enhancement of the total number of surface fast electrons (SFEs) [12]. In addition, the laser parameters (intensities, angle of incidence, polarization, focusing properties) and the target properties (cone shape, preplasma scalelength, surface structure, etc) have been investigated to obtain the optimum interaction conditions for better performances of absorption.

A straightforward way for improving the energy conversion efficiency from the relativistic laser into hot electrons is by increasing the laser intensity [13, 14]. The limitation of this method is that it simultaneously raises the electrons temperature while reducing the effectiveness of the energy deposities into the core plasma in FI [15]. Flat and cone targets have been widely employed in many experiments to enhance the laser energy absorption and to confine the fast electrons to obtain better collimated electron beams [2, 16, 17].

The modulation of the target surface structure is an efficient method to maximize the conversion efficiency of laser energy coupling since vacuum heating is sensitive to the laser field structure at the target surface [18]. Experiments have shown that the laser absorption is more efficient in the fast electron production compared to the flat targets (FTs), by employing coated targets with wavelength-scale spheres [18] and low-density foams [16], as well as using sub-wavelength gratings [19, 20]. In particular, analytical and numerical simulations [25, 26] indicate that the electron acceleration can be improved by resonant SPWs excitation on periodically modulated target surfaces (gratings). A laser pulse with high prepulse-to-pulse contrast ($\leq 10^{-11}$) allows to preserve the surface structures and create a sharp-edged overdense plasma. In most of these experiments, the target surface structure is on a $10s$ nm scale and much smaller than the wavelengths of the incident laser. However, it is expected that the laser field can be built up remarkably through Mie resonances when the size of surface structures is comparable to the laser wavelength. Using dielectric spheres with a diameter slightly larger than the half of the laser wavelength on the target surface, Sumeruk *et al.*, [28] have observed a prominent increase of hot electron number and electron temperature owing to Mie resonances and multipass stochastic heating of the electrons [18].

Another mechanism of electron acceleration is the excitation of plasma surface waves (SPWs) or surface plasmons (SPs). It was demonstrated that SPWs can have direct impact on the acceleration process of electrons and protons [29, 30]. For example, by employing a double plasma mirror laser system with ultrahigh contrast (10^{-12}), a strong electron emission with energies exceeding 10 MeV [30] and protons with higher energies [29] compared with flat targets were produced via resonant excitation of a SPW in a grating target. Theoretical and experimental studies placed the main emphasis on the linear regime of SPWs. Recently, Liu et. al [31] developed a new model which includes relativistic and ponderomotive nonlinearities to explain the target normal sheath acceleration of protons at high intensity and in the presence of a preformed plasma on gratings.

The main goal of the present work was to investigate some fundamental aspects regarding the electron acceleration in the laser-plasma interactions. The experimental studies presented in this dissertation are focused on investigating the physical properties of surface fast electrons and the electron acceleration mechanisms. Different detectors, such as Fuji imaging plates, electron spectrometer and Ulbricht sphere were employed. The ARCTURUS laser system available at ILPP Düsseldorf employed in these experiments delivers high-contrast ($\sim 10^{-12}$ after the plasma mirror), 28 fs laser pulses with intensities higher than $2 \times 10^{20}\mathrm{W/cm}^2$ onto the targets. The laser parameters offer a novel interaction regime where SPWs can be generated in a non-linear way. The new regime of SPW excitation is favored by the relativistic intensity and the very steep preplasma profile of 10s nm scalelength.

The first set of experimental investigations addresses the surface fast electron acceleration, their angular distribution and energy spectra. Targets of different geometries, i.e. flat targets, grating targets and thin foil targets were also taken into account. An evident enhancement of surface fast electrons was observed in case of the grating targets compared with the flat mirror targets. The total number of surface fast electrons produced by wavelength-scaled grating targets (grating's periodicity λ_g is comparable with the laser wavelength λ_L, $\lambda_g = 833$ nm $\approx \lambda_L$) at the angle of incidence $\alpha = 45°$ reached maximum while the electron energies remain similar compared with the other gratings and the flat targets. A significant high-energetic electron flux was also observed for the sub-wavelength grating target ($\lambda_g = 278$ nm$< \lambda_L$) close to the laser specular direction at $\alpha = 45°$. The experimental results were compared with Particle-in-Cell simulations performed in a 2-D geometry. A good agreement with the experimental data was found for a steep plasma profile with the scalelength less than 3% of the laser wavelength.

A non-linear analytical model was developed to interpret the increase of the resonant angle in the SPWs excitation mechanism. The analytical results indicate that the ultra relativistic laser intensity and more realistic preplasma density profile enhance the nonlinear effect and therefore shift the SPWs resonant angle, which supports our experimental observations. For thin foil targets, the efficiency of surface fast electron acceleration is dependent on the surface properties and the thicknesses of the thin foils, and more interesting, on the macroscopic dimensions of the targets.

In the second part of this work, the laser energy absorption by solid targets was investigated. The laser absorption by different targets (flat, grating and thin foil targets) of different laser polarization ($P-$ and $S-$ polarization), at different angles of incidence were investigated and compared. The grating targets absorb the maximum energy at an angle of incidence of 45°, different from flat targets of which the absorption fraction increases with the angle of incidence. The absorption fraction of thin foil targets was also observed to have a similar dependence of the surface fast electron acceleration. Moreover, the thin foil targets with flat surfaces have a higher absorption efficiency than the bulk flat mirror targets.

The structure of this dissertation is as follows:

- An introduction of relevant physical processes which occur during the interaction of the superintense laser pulse with the solid matter is given in the chapter 2. The motion of electrons in an electromagnetic field and relativistic waves in plasmas are reviewed in the first two sections. To describe the experiments and the simulations in the subsequent chapters, the collisional and collisionless absorption processes as well as the propagation of laser light in overdense plasmas are presented. In the following two sections of this chapter, electron heating mechanism and surface fast electron acceleration are also discussed.

- Chapter 3 is dedicated to introduce the laser system employed in the experiments. The important characteristics of the high power ARCTURUS laser system are presented. The contrast enhancement using a plasma mirror system is introduced as well. The experimental arrangements used for investigating the charged particles and measuring the absorbed laser energy fraction are illustrated together with the characteristics of targets used in the experiments.

- In the chapter 4 the experimental results on electron acceleration using solid targets are presented. The enhancement of the electron flux on grating targets was investigated. The characteristics, like electron angular distribution, the charge of electron beam, dependence on the angle of incidence and energy spectra are discussed and compared with the flat target case. The properties of fast electrons generated by thin foil targets with different materials and thicknesses are observed at various experimental conditions like: angles of laser incidence, the laser contrast, dimensions and ground conditions of targets and presented in the second section. In case of thin foils, the efficiency of fast electron acceleration depends mainly on the thickness of the thin foil target.

- Chapter 5 presents the experimental results of the energy absorption measurements. The energy transfer process from laser radiation to matter is determined from considerable physical parameters of the laser as well as targets. In the experiments, the absorbed energy fraction was measured as a function of the laser polarization, incidence angle, bulk targets with different surface properties and thin foil targets with different materials and thicknesses. Finally, the experimental data were interpreted on the basis of the absorption mechanisms relevant for the interaction regime of the experiments.

- Chapter 6 deals with comparison of simulations of laser-grating interactions with experimental results. The influence of preplasma conditions is discussed in detail to reveal that the surface of the target after being heated by the prepulse is of key importance for the main pulse interaction. At last, a numerical simulation and a non-linear analytical model are given to interpret the mechanism of resonant surface plasma waves excitation.

- The last chapter summarises the experimental and simulation results and gives an outlook for future investigations and experiments.

Role of the author:

The author was the leader of the experiments at ARCTURUS laser facility in Düsseldorf and the experimental work presented in this thesis.

The author has performed the data analysis and interpretation. Furthermore, the author calibrated Imaging Plate records and analysed quantitatively the magnetic electron spectrometer in electron acceleration measurements. Moreover, the author has performed the 2D PIC simulations presented in Chapter 6 using a fully relativistic PIC code EPOCH on the high performance cluster of the Centre for Information and Media Technology (ZIM) at the University of Düsseldorf. In addition, the author interpreted the data in Section 6.5 based on the analytical model developed by Prof. A. Andreev from Max-Born Institute, Berlin.

Chapter 2

Superintense Laser-Plasma Interaction

When a laser pulse with the intensity $I_L > 10^{16}\mathrm{W/cm^2}$ interacts with matter, fast ionization processes generate a plasma in which the electrons can move freely. At relativistic intensities ($I_L > 10^{18}\mathrm{W/cm^2}$), the laser field amplitude is so high that the electrons will be accelerated to a velocity close to the speed of light c, such that the dynamics of the interacting electrons must be described relativistically.

The key point of describing relativistic laser-plasma interaction is to assume that the dynamics is dominated by collective behaviours rather than local interactions among neighbouring particles. This means that the force on each particle due to the mean electromagnetic (EM) field created by all the charges in the system is much larger than the forces exerted by the nearest neighbouring particles. In other words, the collisions between the neighbouring particles are assumed to be less relevant than the coherent motion in the mean field. In this case, all relevant frequencies must be larger than those of collisions. In classical plasmas, the frequency of collisions is proportional to the cross section of Coulomb scattering and inversely proportional to the particle energy. Hence, the high energy density due to the relativistic EM field smears the rate of collisions and the plasma can be treated as collisionless, i.e. the particles do not interact with each other. The matter is assumed as fully ionised in presence of superintense electric field, at least for the outer electrons.

This chapter discusses the basic principles of interaction between the relativistic EM fields of the laser and matter. Textbooks are mainly from Macchi [21], Gibbon [22], Kruer [23] and Mulser [24] for further details.

2.1 Electrons in Electromagnetic Field

In this section, the motion of single electron in a plane wave is described first, including the relativistic dynamics and nonlinear equations. Afterwards, the ponderomotive force and radiation friction are introduced. In the second part of the section, a briefly review of the basic kinetic and hydrodynamic equations is present. The derivation in this section follows Macchi [21].

2.1.1 Single Electron in Electromagnetic Field

Non-relativistic Motion in a Plane Wave

The electric and magnetic fields of a plane wave propagating in the x direction can be written in the complex representation as:

$$\mathbf{E} = \mathbf{E}(x,t) = E_0 \hat{\boldsymbol{\varepsilon}} \mathrm{e}^{ikx - i\omega t}, \qquad \mathbf{B} = \mathbf{B}(x,t) = \hat{\mathbf{x}} \times \mathbf{E} \tag{2.1}$$

where the fields are the real parts of the expressions. Here $k = \omega/c$ and $\hat{\varepsilon}$ is the polarization vector. $\hat{\varepsilon} = \hat{\mathbf{y}}$ (or $\hat{\mathbf{z}}$) denotes the linear polarization along y (or z) direction while for circular polariation, $\hat{\varepsilon} = (\hat{\mathbf{y}} \pm \mathrm{i}\hat{\mathbf{z}})/\sqrt{2}$. The equations of an electron motion in non-relativistic EM fields are:

$$m_e \frac{\mathrm{d}\mathbf{v}}{\mathrm{d}t} = -e\left[\mathbf{E}(\mathbf{r},t) + \frac{\mathbf{v}}{c} \times \mathbf{B}(\mathbf{r},t)\right], \qquad \frac{\mathrm{d}\mathbf{r}}{\mathrm{d}t} = \mathbf{v} \tag{2.2}$$

In general the term $\mathbf{v} \times \mathbf{B}$ is neglected in the linear approximation for weak fields and the linear solutions are thus obtained only with the same frequency of the oscillating motion as:

$$\mathbf{v} = -\frac{ie}{m_e\omega}\mathbf{E}, \qquad \mathbf{r} = \frac{e}{m_e\omega^2}\mathbf{E} \tag{2.3}$$

It is obvious that the trajectory is a straight line for linear polarization and a circle for circular polarization.

The dimensionless parameter of EM fields called the normalized vector potential is defined as the ratio between the electron momentum and $m_e c$,

$$a_0 \equiv \frac{eE_0}{m_e \omega c} \tag{2.4}$$

If $a_0 \ll 1$, $|\mathbf{v}| \ll c$ is fulfilled, the linear solution approximation is justified. If a_0 now is close to unity, the effects of the magnetic force should be taken into account. We use the "perturbative" method and write the velocity as $\mathbf{v} = \mathbf{v}^{(1)} + \mathbf{v}^{(2)}$ where $\mathbf{v}^{(1)}$ and $\mathbf{v}^{(2)}$ are of order $\sim a_0$ and $\sim a_0^2$ respectively. Now the equation of motion becomes:

$$m_e \frac{\mathrm{d}(\mathbf{v}^{(1)} + \mathbf{v}^{(2)})}{\mathrm{d}t} = -e\left[\mathbf{E}(\mathbf{r}, t) + \frac{\mathbf{v}^{(1)} + \mathbf{v}^{(2)}}{c} \times \mathbf{B}(\mathbf{r}, t)\right] \tag{2.5}$$

And it is straightforward to obtain

$$m_e \frac{\mathrm{d}\mathbf{v}^{(1)}}{\mathrm{d}t} = -e\mathbf{E}, \qquad m_e \frac{\mathrm{d}\mathbf{v}^{(2)}}{\mathrm{d}t} = -e\frac{\mathbf{v}^{(1)}}{c} \times \mathbf{B} \tag{2.6}$$

Assuming the linear polarization along $\mathrm{y}-$direction ($\hat{\varepsilon} = \hat{\mathbf{y}}$), it may be written as:

$$\mathbf{v}^{(1)} = \frac{eE_0}{m_e \omega} \hat{\mathbf{y}} \sin \omega t = a_0 c \hat{\mathbf{y}} \sin \omega t, \qquad \mathrm{y}^{(1)} = -a_0 \frac{c}{\omega} \cos \omega t \tag{2.7}$$

where we assign the initial position of the electron at $x = 0$. Considering $\mathbf{B}(x = 0, t) = E_0 \hat{\mathbf{z}} \cos \omega t$ into the equation for $\mathbf{v}^{(2)}$, we get:

$$\frac{\mathrm{d}\mathbf{v}^{(2)}}{\mathrm{d}t} = -\hat{\mathbf{x}} \frac{e}{m_e c} (a_0 c \sin \omega t)(E_0 \cos \omega t) = -\hat{\mathbf{x}} \frac{a_0^2}{2} c\omega \sin 2\omega t \tag{2.8}$$

Thus, the electron oscillates along the x direction with a frequency of 2ω:

$$v_x^{(2)}(t) = \frac{a_0^2 c}{4} \cos 2\omega t, \qquad x^{(2)}(t) = -\frac{a_0^2 c}{8\omega} \sin 2\omega t \tag{2.9}$$

Defining the dimensionless coordinates $X = (\omega x/c)/a_0^2$ and $Y = (\omega y/c)/a_0$, we obtain the famous $figure$-of-$eight$ trajectory of the electron shown in Figure 2.1:

$$16X^2 = Y^2(1 - Y^2) \tag{2.10}$$

For circular polarization, the trajectory is unaffected by $\mathbf{v}^{(1)} \times \mathbf{B}$ term in the first order of approximation and the electron still undergoes a circular orbit with radius $a_0 c/(\sqrt{2}\omega)$.

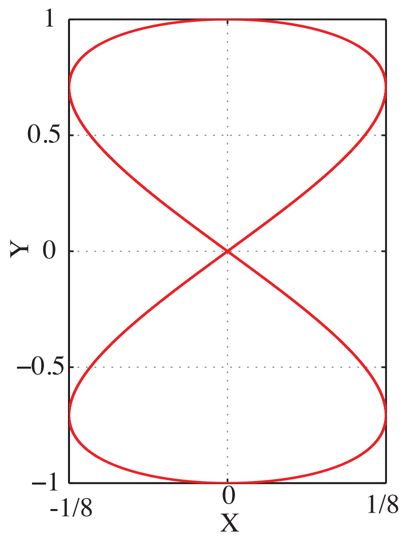

Figure 2.1: Characteristic figure-of-eight orbit of a free electron in a plane EM wave in the average rest frame.

Relativistic Regime

The dimensionless quantity a_0 defined by (2.4) is the maximum momentum of an electron oscillating in an $\mathbf{E}$ field with frequency ω and amplitude E_0 in units of $m_e c$. In fact, a_0 is a convenient measurement of relativistic effects. When $a_0 \gtrsim 1$, the laser-plasma interaction may be defined as in the "relativistic regime". The laser intensity I can be expressed in the form of a_0:

$$I = \left\langle \frac{c}{4\pi} |\mathbf{E} \times \mathbf{B}| \right\rangle = \frac{c}{8\pi} \left(\frac{m_e \omega c a_0}{e} \right)^2, \tag{2.11}$$

$$a_0 = 0.85 \left(\frac{I\lambda^2}{10^{18}\mathrm{W/cm^2}} \right)^{1/2}. \tag{2.12}$$

At present, multi 100 TW laser systems generate pulses which can reach focused intensities above $2 \times 10^{22}\mathrm{W/cm^2}$ [33] for λ=0.8μm, corresponding to $a_0 \sim 68$.

Now the relativistic equation for the momentum is:

$$\frac{\mathrm{d}\mathbf{p}}{\mathrm{d}t} = -e\left(\mathbf{E} + \frac{\mathbf{v}}{c} \times \mathbf{B} \right), \qquad \mathbf{p} = m_e \gamma \mathbf{v}, \tag{2.13}$$

where $\gamma = (1 - v^2/c^2)^{-1/2}$. The EM plane wave is assumed to propagate along $\hat{\mathbf{x}}$ and represented by the vector potential $\mathbf{A} = \mathbf{A}(x,t)$ with $\mathbf{A} \cdot \hat{\mathbf{x}} = 0$. After some vector algebra, from (2.13) one obtains

$$\frac{\mathrm{d}}{\mathrm{d}t} \left(\mathbf{p}_\perp - \frac{e}{c}\mathbf{A} \right) = 0, \tag{2.14}$$

where the subscript"$\perp$" refers to the vector component in the transverse yz plane. We take the vector potential

$$\mathbf{A} = A_0\big[\hat{\mathbf{y}}\delta\cos\phi + \hat{\mathbf{z}}(1-\delta^2)^{1/2}\sin\phi\big], \qquad \phi = kx - \omega t, \tag{2.15}$$

where δ=1 or 0 means the wave is linearly polarized along $\hat{\mathbf{y}}$ or $\hat{\mathbf{z}}$, respectively and $\delta = \pm 1/\sqrt{2}$ means circularly polarized. Other values of δ correspond to elliptical polarization. Here we evaluate the derivative of ϕ with respect to time as $\frac{\mathrm{d}\phi}{\mathrm{d}t} = -\frac{\omega}{\gamma}$ and get immediately:

$$\mathbf{p}_\perp = (p_y, p_z) = \frac{eA_0}{c}(\delta\cos\phi, (1-\delta^2)^{1/2}\sin\phi), \tag{2.16}$$

$$\begin{aligned} p_x &= \frac{1}{2m_ec}\left(\frac{eA_0}{c}\right)^2\big[\delta^2\cos^2\phi + (1-\delta^2)\sin^2\phi\big] \\ &= \frac{1}{4m_ec}\left(\frac{eA_0}{c}\right)^2\big[1 + (2\delta^2-1)\cos 2\phi\big]. \end{aligned} \tag{2.17}$$

Averaging over an oscillation cycle $\langle\cos 2\phi\rangle = 0$ and

$$\langle p_x\rangle = \frac{1}{4m_ec}\left(\frac{eA_0}{c}\right)^2 = m_ec\frac{a_0^2}{4} \equiv p_d. \tag{2.18}$$

So the longitudinal drift of the electron is constant. Together with $\mathbf{p}_\perp^2 = (eA_0/c)^2/2$, we get $\mathbf{p}^2 = \mathbf{p}_\perp^2 + p_x^2$ and the relativistic factor γ is constant as well.

After integrating (2.16, 2.17), normalizing the coordinates to $1/k = c/\omega$ and defining $\hat{\mathbf{r}} = k\mathbf{r}$, the trajectory of the electron is given by:

$$\begin{aligned} \frac{\hat{x}}{a_0^2} &= \frac{1}{4}\Big[-\phi - \big(\delta^2 - \frac{1}{2}\big)\sin 2\phi\Big] \\ \frac{\hat{y}}{a_0} &= -\delta\sin\phi, \qquad \frac{\hat{z}}{a_0} = (1-\delta^2)^{1/2}\cos\phi. \end{aligned} \tag{2.19}$$

Figure 2.2 shows the typical trajectories of plane waves with linear ($\delta = 1$) and circular ($\delta = \pm 1/\sqrt{2}$) polarization for $a_0 = 2$.

Ponderomotive Force

The ponderomotive force (PF) is a nonlinear force exerted on the electrons of the plasma by an inhomogeneous oscillating electromagnetic field. The motion equation of electrons in the plasma under the effect of the laser electric and

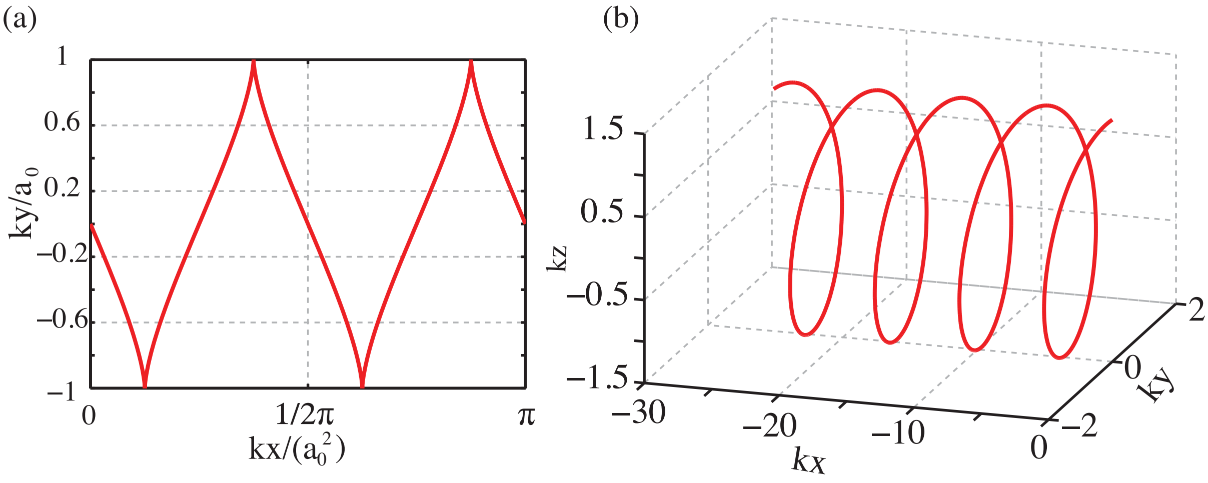

Figure 2.2: The trajectory of an electron in an monochromatic plane wave for $a_0 = 2$. (a) Linear polarization along $\hat{\mathbf{y}}$ ($\delta = 1$). (b) Circular polarization ($\delta = \pm 1/\sqrt{2}$).

magnetic field can be written as

$$\frac{\mathrm{d}\mathbf{v}}{\mathrm{d}t} = -\frac{e}{m}(\mathbf{E}(r) + \mathbf{v} \times \mathbf{B}(r)). \tag{2.20}$$

If the amplitude of the laser electromagnetic field varies in space, the force the oscillating fields exerting on the electrons can be non-zero. It can be understood more easily considering a non-relativistic wave. The varieties of amplitude of the electric field will cause that the electrons cannot be back to its original position. The electrons will drift toward the regions where the electric field is smaller due to such an average effect. At relativistic intensities, the Lorentz force leads the electrons to populate in regions where the intensity is lower.

Considering $\mathbf{E} = \mathbf{E_0}(\mathbf{r})\cos\omega t$, where $\mathbf{E_0}$ is the field at the initial position $\mathbf{r_0}$, we evaluate with a perturbative method and neglect the $\mathbf{v} \times \mathbf{B}$ term in the first order. The solution of the Eq. 2.20 is

$$\frac{\mathrm{d}\mathbf{v_1}}{\mathrm{d}t} = -\frac{e}{m}\mathbf{E_0}(\mathbf{r_0})\cos\omega t \tag{2.21}$$

$$\mathbf{v_1} = -\frac{e}{m\omega}\mathbf{E_0}(\mathbf{r_0})\sin\omega t \tag{2.22}$$

$$\mathbf{r_1} = -\frac{e}{m\omega^2}\mathbf{E_0}(\mathbf{r_0})\cos\omega t \tag{2.23}$$

Now we consider the second order the term $\mathbf{v_1} \times \mathbf{B_1}$. $\mathbf{B_1}$ can be obtained by Maxwell's equation

$$\nabla \times \mathbf{E_0} = -\frac{\mathrm{d}\mathbf{B}}{\mathrm{d}t} \tag{2.24}$$

$$\mathbf{B_1} = -\frac{1}{\omega}\nabla \times \mathbf{E_0}|_{r=r_0} \sin \omega t \tag{2.25}$$

Expanding $\mathbf{E}(\mathbf{r})$ about $\mathbf{r_0}$ we obtain

$$\mathbf{E}(\mathbf{r}) = \mathbf{E}(\mathbf{r_0}) + (\mathbf{r_1} \cdot \nabla)\mathbf{E}|_{r=r_0} + ... \tag{2.26}$$

Together with Eqs. (2.21 , 2.22) the equation of motion in the second order is

$$\begin{aligned} \frac{\mathrm{d}\mathbf{v_2}}{\mathrm{d}t} = &- \frac{e}{m}\Big\{ \Big[\mathbf{E_0} \cos \omega t + \Big(\frac{e}{m}\frac{\mathbf{E_0}}{\omega} \cos^2 \omega t \cdot \nabla \Big) \mathbf{E_0} \Big] \\ &+ \frac{e}{m\omega^2} \sin^2 \omega t \Big[\mathbf{E_0} \times (\nabla \times \mathbf{E_0}) \Big] \Big\} \end{aligned} \tag{2.27}$$

The average of the term $\cos \omega t$ over an oscillation period goes to zero while $< \sin^2 \omega t >=< \cos^2 \omega t >= 1/2$. Thus, the Eq. 2.27 becomes

$$\left\langle \frac{\mathrm{d}\mathbf{v_2}}{\mathrm{d}t} \right\rangle = -\frac{1}{2}\frac{e^2}{m^2\omega^2}\Big[(\mathbf{E_0} \cdot \nabla)\mathbf{E_0} + \mathbf{E_0} \times (\nabla \times \mathbf{E_0}) \Big] \tag{2.28}$$

and can be written as

$$\left\langle \frac{\mathrm{d}\mathbf{v_2}}{\mathrm{d}t} \right\rangle = -\frac{1}{2}\frac{e^2}{m^2\omega^2}\nabla \langle \mathbf{E}^2 \rangle \tag{2.29}$$

where $\mathbf{E_0}^2 = 2\langle \mathbf{E}^2 \rangle$.

The right hand side of the Eq. 2.29 is the effective nonlinear force on a single electron. By multiplying the Eq. 2.29 with the electron density n_0 and substituting

$$\omega_p^2 = \left(\frac{4\pi e^2 n_0}{m} \right) \tag{2.30}$$

where ω_p is the plasma frequency, the ponderomotive force can be obtained as

$$\mathbf{F}_p = -\frac{\omega_p^2}{\omega^2}\frac{\nabla \left\langle \mathbf{E}^2 \right\rangle}{8\pi} \tag{2.31}$$

The ponderomotive force (Eq. (2.31)) drives the electrons to the regions of lower field pressure and eventually effects the ions through charge-separation fields.

We now consider "realistic" laser pulses with finite spatial width and duration. In general, a laser pulse is described by an envelope function as:

$$\begin{aligned}\mathbf{E}(\mathbf{r},t) &= \mathrm{Re}\Big(\tilde{\mathbf{E}}(\mathbf{r},t)\mathrm{e}^{-\mathrm{i}\omega t}\Big) = \frac{1}{2}\tilde{\mathbf{E}}(\mathbf{r},t)\mathrm{e}^{-\mathrm{i}\omega t} + \mathrm{c.c.},\\ \mathbf{B}(\mathbf{r},t) &= \mathrm{Re}\Big(\tilde{\mathbf{B}}(\mathbf{r},t)\mathrm{e}^{-\mathrm{i}\omega t}\Big) = \frac{1}{2}\tilde{\mathbf{B}}(\mathbf{r},t)\mathrm{e}^{-\mathrm{i}\omega t} + \mathrm{c.c.}.\end{aligned} \tag{2.32}$$

We assume that the E field almost averages to zero over a period, i.e. $\langle\mathbf{E}(\mathbf{r},t)\rangle \simeq 0$ while for the envelope function $\langle\tilde{\mathbf{E}}(\mathbf{r},t)\rangle \neq 0$. This assumption suggests us to describe the electron motion as the superposition of the slow term and the fast oscillating term. Under certain conditions, the ponderomotive force is slowly-varying force to drive the "slow motion" in the dynamic equation.

Averaging the Newton's equation we have:

$$\begin{aligned}m_e\frac{\mathrm{d}\mathbf{v}_s}{\mathrm{d}t} &= -e\langle\mathbf{E}(\mathbf{r}(t),t)\rangle - e\langle\mathbf{v}\times\mathbf{B}(\mathbf{r}(t),t)\rangle\\ &\simeq -\frac{e^2}{4m_e\omega^2}\nabla|\mathbf{E}^*(\mathbf{r}_s(t),t)|^2\\ &= -\frac{e^2}{2m_e\omega^2}\nabla|\big\langle\mathbf{E}^2(\mathbf{r}_s(t),t)\big\rangle \equiv \mathbf{F}_p.\end{aligned} \tag{2.33}$$

The PF $\mathbf{F}_p$ defined in (2.33) is derived within the non-relativistic regime and describes the cycle-averaged position and velocity of the oscillation center:

$$m_e\frac{\mathrm{d}^2\langle\mathbf{r}\rangle}{\mathrm{d}t} = m_e\frac{\mathrm{d}\langle\mathbf{v}\rangle}{\mathrm{d}t} = \mathbf{F}_p = -\nabla\Phi_p, \tag{2.34}$$

where "ponderomotive potential" Φ_p is the energy of the cycle-averaged oscillation which is assumed to be a function of the oscillation center position:

$$\Phi_p = \Phi_p(\langle\mathbf{r}\rangle) = \frac{m_e}{2}\big\langle\mathbf{v}_o^2\big\rangle = \frac{e^2}{2m_e\omega^2}\big\langle\mathbf{E}^2\big\rangle. \tag{2.35}$$

From (2.34, 2.35), we can see that the electrons will be expelled from the regions where the electric field is higher.

The relativistic expression of the ponderomotive force can be derived from the force equation

$$\frac{\partial\mathbf{p}}{\partial t} + \mathbf{v}\cdot\nabla\mathbf{p} = -e\bigg(\mathbf{E} + \frac{\mathbf{v}}{c}\times\mathbf{B}\bigg) \tag{2.36}$$

where $\mathbf{p} = m\gamma\mathbf{v}$. By substituting $\mathbf{B}$ and $\mathbf{E}$ in function of the vector $\mathbf{A}$ and electrostatic potential Φ, the relativistic ponderomotive force can be derived

$$\mathbf{F}_p = -m_e c^2 \nabla(\gamma - 1). \tag{2.37}$$

The derivation of the PF in the relativistic regime can be found in [24] in detail. In the case of EM waves, the $\mathbf{F}_p$ is again minus the gradient of the circle-averaged oscillation energy.

Radiation Friction

An electron subjected to an external EM field is accelerated and emits EM radiation simultaneously. Both, the external and the induced radiation field, act on the electron. In other words, together with the extrinsic Lorentz force, the additional *radiation friction force* $\mathbf{f}_{rad}$ will exert on the electron with the form as

$$\begin{aligned} \mathbf{f}_{\mathrm{rad}} = \frac{2e^2}{3c^3}\ddot{\mathbf{v}} &\simeq -\frac{2e^3}{3m_e c^3}\frac{\mathrm{d}}{\mathrm{d}t}\big(\mathbf{E} + \frac{\mathbf{v}}{c} \times \mathbf{B}\big) \\ &\simeq -\frac{2e^3}{3m_e c^3}\big(\dot{\mathbf{E}} - \frac{e}{m_e c^3}\mathbf{E} \times \mathbf{B}\big), \end{aligned} \tag{2.38}$$

where v is the electron velocity and $\mathbf{B}_0$ is the applied magnetic field. The relativistic expression for RF in Sect. 76 of Ref.[34] is:

$$\begin{aligned} \mathbf{f}_{\mathrm{rad}} = &\frac{2r_c^2}{3}\Big\{-\gamma^2\big[\big(\mathbf{E} + \frac{\mathbf{v}}{c} \times \mathbf{B}\big)^2 - \big(\frac{\mathbf{v}}{c} \cdot \mathbf{E}\big)^2\big]\frac{\mathbf{v}}{c} \\ &\big[\big(\mathbf{E} + \frac{\mathbf{v}}{c} \times \mathbf{B}\big) \times \mathbf{B} + \big(\frac{\mathbf{v}}{c} \cdot \mathbf{E}\big)\mathbf{E}\big] - \gamma\frac{m_e c}{e}\big(\dot{\mathbf{E}} + \frac{\mathbf{v}}{c} \times \dot{\mathbf{B}}\big)\Big\}, \end{aligned} \tag{2.39}$$

and is called Landau-Lifshitz force. As this force acts on the electron together with the Lorentz force, the electron is accelerated in the average rest frame and the figure of trajectory of the electron will develop. The exact solution for the motion of an electron in a plane wave can be found in [35].

2.1.2 Collective Dynamics

Kinetic Equations

For a collisionless system in which the number of particles is conserved for each species a, the distribution function f_a obeys the kinetic equation

$$\partial_t f_a + \nabla_{\mathbf{r}} \cdot (\dot{\mathbf{r}}_a f_a) + \nabla_{\mathbf{p}} \cdot (\dot{\mathbf{p}}_a f_a) = 0, \tag{2.40}$$

which can also be understood as a continuity equation in the phase space.

The Vlasov theory of a plasma assumes that the force on the particle is the Lorentz force and the EM fields can be obtained self-consistently via Maxwell's equations. The standard Vlasov equation may be written as

$$\partial_a f_a + \mathbf{v} \cdot \nabla_{\mathbf{r}} f_a + q_a(\mathbf{E} + \mathbf{v} \times \mathbf{B}/c) \cdot \nabla_{\mathbf{p}} f_a = 0. \tag{2.41}$$

The nonlinear equations of Vlasov and Maxwell equations constitute the so-called Vlasov-Maxwell system of which the analytical solutions are very hard to find. However, there are efficient numerical methods to solve the Vlasov-Maxwell system, for exampe the Particle-In-Cell (PIC) approach [36, 37].

Fluid Equations

Integrating (2.41) over momentum leads to the continuity equation

$$\partial_t n_a + \nabla \cdot (n_a \mathbf{u}_a) = 0. \tag{2.42}$$

where n_a and $\mathbf{u}_a$ are the total density and the mean velocity of the particle a, respectively. Multiplying (2.41) by **v** and again integrating over the momentum, together with (2.42), the non-relativistic fluid equation for the mean velocity $\mathbf{u}_a$ with a scalar pressure term P_a can be obtained

$$m_a n_a(\partial_a \mathbf{u}_a + \mathbf{u}_a \cdot \nabla \mathbf{u}_a) = q_a n_a(\mathbf{E} + \mathbf{u}_a \times \mathbf{B}/c) - \nabla \mathsf{P}_a. \tag{2.43}$$

In very intense laser-plasma interactions, the electron motion is dominated by the coherent oscillation in the EM fields, which means the thermal velocity is negligible with respect to the average coherent velocity and it leads to $\mathsf{P}_a = 0$. So neglecting the P_a results in the relativistic equation, so-called "cold fluid" momentum equation

$$(\partial_t \mathbf{p}_a + \mathbf{u}_a \cdot \nabla \mathbf{p}_a) = q_a(\mathbf{E} + \mathbf{u}_a \times \mathbf{B}/c), \qquad \mathbf{p}_a = m_a \gamma_a \mathbf{u}_a. \tag{2.44}$$

2.2 Relativistic Waves in Plasmas

This section focuses on the waves in a relativistic plasma. For EM waves, the nonlinear refractive index and two most prominent phenomena: self-focusing and transparency are introduced. For electrostatic waves, the wave-breaking limit with a focus on relevant properties of the electron accelerators are discussed. The derivation in this section follows Macchi [21].

2.2.1 Linear Waves

We eliminate **B** from Maxwell's equations in a plasma [38] and obtain the wave equation for the electric field

$$\left(\nabla^2 - \frac{1}{c^2}\partial_t^2\right)\mathbf{E} - \nabla(\nabla \cdot \mathbf{E}) = \frac{4\pi}{c^2}\partial_t \mathbf{J}, \tag{2.45}$$

where the current density of a "cold" plasma $\mathbf{J} = -en_e\mathbf{u}_e$ in which only electrons response to the high-frequency fields.

Firstly, we consider *linear* waves in a homogeneous plasma with a uniform and constant electron density n_e. For monochromatic fields,

$$\tilde{\mathbf{J}} = -\mathrm{i}\frac{n_0 e^2}{m_e \omega}\tilde{\mathbf{E}} = -\frac{\mathrm{i}}{4\pi}\frac{\omega_p^2}{\omega}\tilde{\mathbf{E}}. \tag{2.46}$$

where

$$\omega_p = \left(\frac{4\pi e^2 n_e}{m_e}\right)^{1/2} \tag{2.47}$$

is the plasma frequency. Substituting (2.46) into (2.45) we obtain the inhomogeneous Helmholtz equation

$$\left(\nabla^2 + \varepsilon(\omega)\frac{\omega^2}{c^2}\right)\tilde{\mathbf{E}} - \nabla(\nabla \times \tilde{\mathbf{E}}) = \left(\nabla^2 + \mathsf{n}^2(\omega)\frac{\omega^2}{c^2}\right)\tilde{\mathbf{E}} - \nabla(\nabla \times \tilde{\mathbf{E}}) = 0, \tag{2.48}$$

where $\varepsilon(\omega)$ and $\mathsf{n}(\omega)$ are the dielectric function and the refraction index of a cold plasma, respectively.

$$\varepsilon(\omega) = \mathsf{n}^2(\omega) = 1 - \frac{\omega_p^2}{\omega^2} \tag{2.49}$$

Now we consider the transverse EM plane waves. The dispersion relation reads:

$$-k^2c^2 + \varepsilon(\omega)\omega^2 = -k^2c^2 + \omega^2 - \omega_p^2 = 0. \tag{2.50}$$

A wave can propagate in the plasma only when k is a real number, which requires

$\omega > \omega_p$. This means the plasma density must fulfill

$$n_e < n_c \equiv \frac{m_e \omega^2}{4\pi e^2} = 1.1 \times 10^{21} \mathrm{cm}^{-3} (\lambda/1\mu\mathrm{m})^{-2}, \tag{2.51}$$

where n_c is called the critical density. Eq. (2.51) is only valid in the non-relativistic case, otherwise $m_e = m_0 \gamma_e$. A plasma with an electron density $n_e < n_c$, allowing the propagation of transverse EM waves is called the *underdense* plasma. The opposite ($n_e > n_c$) is an *overdense* plasma in which the EM wave cannot propagate. In overdense region, the evanescent field will decay exponentially as $\sim \exp(-x/\ell_s)$ where the characteristic distance

$$\ell_s = c(\omega_p^2 - \omega^2)^{1/2}, \tag{2.52}$$

is the called $skin - depth$. For overdense plasmas $\omega_p \gg \omega$, $\ell_s \approx c/\omega_p = 5.31 \times 10^5 n_e^{-1/2}$cm. For a typical laser wavelength $\lambda \sim 1\mu$m, the gas targets (typical density $\sim 10^{20}\mathrm{cm}^{-3}$) will be underdense and solid targets (typical density $\sim 10^{23}\mathrm{cm}^{-3}$) will be overdense.

When an ultrashort, high contrast laser pulse at a low intensity interacts with a solid target, the plasma expansion before and during the interaction is negligible, i.e. the density scalelength $L_n = n_e/|\partial_x n_e| \ll \lambda$. In such case, the electron density can be treated as a step-like density profile and the amplitudes of reflected and transmitted waves can be evaluated from Fresnel formulas (Sect.7.3 of Ref. [38]).

The *longitudinal electrostatic* (ES) plane waves ($\mathbf{k} \parallel \mathbf{E}$) exist in the plasma only for $\varepsilon(\omega) = 0$, i.e. $\omega = \omega_p$. They are called plasma waves or plasmons of which the group velocity vanishes while the phase velocity may be arbitrary, and the dispersion relation is $\omega^2 = \omega_p^2 + \gamma_e k^2 \nu_{te}^2$ with ν_{te} being the plasma thermal velocity.

2.2.2 Relativistic Self-Focusing

We now consider the propagation of an EM wave in the relativistic regime. At such a high intensity, the motion of electrons becomes relativistic. We replace $m_e \to m_0 \gamma_e$ where $\gamma_e = \gamma_e(a_0) = (1 + a_0^2/2)^{1/2}$ in Eqs. (2.49) and (2.50) to obtain the nonlinear $\varepsilon(\omega)$, $\mathsf{n}(\omega)$ and the dispersion relation as

$$\varepsilon_{nl}(\omega) = \mathsf{n}_{nl}^2(\omega) = 1 - \frac{\omega_p^2}{\gamma_e \omega^2}, \qquad -k^2 c^2 + \omega^2 - \frac{\omega_p^2}{\gamma_e} = 0. \tag{2.53}$$

A typical laser beam with a Gaussian-like profile in the transverse direction has the peak value a_0 on the axis and decreases with the distance r away from the axis. From (2.53) we can see that the refractive index has the same dependence on r as a_0, which shows similar features as an optical fiber. So the laser beam will be bent and re-collimated by the plasma which takes an effect of a converging lens.

There is the finite width of the laser beam, so the radial component of the ponderomotive force will expel electrons out of the central region of the beam and create a density depression around the axis. The local refractive index will increase due to the density decrease and hence also produce a focusing effect for the laser pulse, called "self-channeling". In general, the self-focusing effect comes mainly from two effects. One is the relativistic effect of the effective inertia of electrons, and the other is the density profile modified self-consistently by the competition of the PF and the space-charge electric force generated by charge displacement.

2.2.3 Relativistic Transparency

According to Eq. (2.53), a light wave can propagate in the homogeneous plasma when $\omega > \omega_p/\gamma^{1/2}$, which means the effective critical density now increases to $n_c' = n_c\gamma > n_c$ with respect to the linear regime. The effect is known as relativistic *self-induced transparency* (SIT) or relativistic transparency. In reality, the real pulse has a finite profile such that only those parts of the pulse of which the local amplitude meets the condition that $n_c\gamma > n_e$ may penetrates inside the overdense plasma. In this way, the shape of the pulse is modified.

Figure 2.3 shows the nonlinear situation of a plane wave penetrating the overdense plasma. The ponderomotive force pushes electrons, producing a charge separation layer at the surface of the plasma. The electrons are piled up and that makes the density n_e higher than the initial density n_0 in some region.

2.2.4 Electrostatic Oscillations and Waves

As mentioned in 2.2.1, the dispersion relation of the electrostatic (ES) oscillations in a cold plasma is $\omega = \omega_p$ which does not contain the wavevector k. The wavelength and the phase velocity of the plasma oscillation can be determined when the plasma oscillation is excited. Many sorts of means can excite plasma

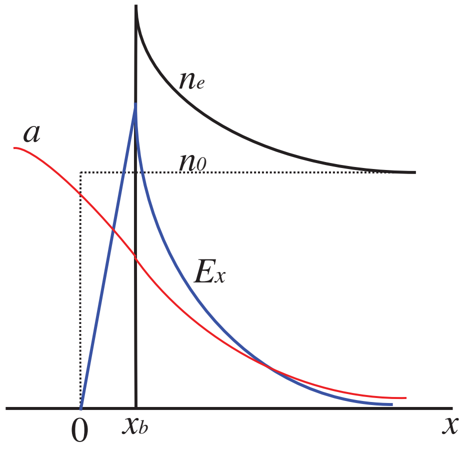

Figure 2.3: The sketch of the electric field and the electron density profile for the plane wave penetrating an overdense plasma. The laser is incident from the left. n_0 is the initial electron density of the plasma. a is the EM vector potential.

oscillations, like particle beams, instabilities and mode conversion *et al.*. However, mode conversion is one of the main techniques for coupling electromagnetic wave energy into a plasma.

In a longitudinal wave, the oscillation amplitude of the particles cannot exceed the wavelength, otherwise the regular periodic structure will be lost and the wave is said to $break$. The wavebreaking plays an important role in the electron acceleration process and can drive electrons up to higher energies. The maximum energy of which the electrons can reach is given by:

$$\max(E_x) = \frac{m_e \omega_p c}{e} \sqrt{2(\gamma_p - 1)} \equiv E_{wb} \tag{2.54}$$

which is called as "relativistic wavebreaking" limit [21]. When $\beta_p = v_p/c \ll 1$, we obtain again $\max(E_x) = m_e \omega_p v_p / e$. When the wave amplitude reaches the breaking threshold, the electric field acquires a sawtooth shape. It is also possible to estimate the distance between adjacent spikes, i.e. the wavelength λ_p of the nonlinear wave:

$$\lambda_p \simeq 4(c/\omega_p)\sqrt{2(\gamma_p - 1)} \tag{2.55}$$

2.3 Electron Heating

In this section, the generation of high-energy electrons in laser-plasma interactions will be discussed in two different regimes. Firstly, the electron acceleration in wake waves will be considered in an underdense plasma. Secondly, the case of an overdense plasma will be presented, where the electrons are accelerated at the vacuum-plasma interface where the collisionless absorption is dominant. The derivation in this section follows Macchi [21] and Gibbon [22].

2.3.1 Underdense Plasmas: Laser Wakefield Accelerators

There are two necessary conditions for an EM wave to accelerate a charged particle efficiently: the electric field has a component along the propagation direction, and there exists the phase velocity that can optimize the phase between the wave and the particle. The longitudinal electron plasma waves with a phase velocity v_p independent of the plasma frequency match the above conditions and can be used as the charged particle accelerators. To accelerate relativistic particles, the phase velocity of the plasma wave should be close to but not exceeding the speed of light, $v_p \lesssim c$, so that the relativistic particles may remain in phase with the wave. The acceleration process may be more efficient for higher relativistic energies since a large change in energy corresponds to a small change in velocity, thus the particle may get out of phase after a long time.

We propose a wakefield generated by an intense laser pulse propagates at a group velocity $v_g = c(1 - \omega_p^2/\omega^2)^{1/2} \lesssim c$ in an underdense plasma. The ponderomotive force (PF) on electrons in the longitudinal direction reads

$$F_p = F_p(x - v_g t) = -m_e c^2 \partial_x \gamma_a, \qquad \gamma_a = \Big(1 + \langle \mathbf{a}^2(x - v_g t)\rangle\Big)^{1/2}, \tag{2.56}$$

where $\mathbf{a}^2(x - v_g t)$ is the dimensionless amplitude of the laser pulse and $v_p = v_g \sim c$ as desired. For an ultra relativistic laser pulse of amplitude $a_0 \gg 1$, the wavelength λ_p of the wake wave depends on a_0 and the wake wave is highly nonlinear. This dependence results in the phase fronts of the wake wave being curved around the laser axis, and the transverse structure of the wakefield can make the wavebreaking threshold lower than in the plane geometry.

The accelerating distance L_{acc} of the electron trapped in the wave is estimated as:

$$L_{acc} = \frac{W}{eE_0} \simeq \frac{2\omega^2 c}{\omega_p^3} = \frac{\lambda}{\pi}\Big(\frac{\omega}{\omega_p}\Big)^3 \tag{2.57}$$

where W is the energy gain. In general, the L_{acc} is larger than the Rayleigh length so the generated plasma wake will diffract the driving laser pulse. Thus, one of the task to develop the laser-plasma electron accelerator is to guide the laser pulse over long distance by employing several approaches, either in a stable self-guiding regime near the self-focusing threshold or in a low-density channel in the plasma.

2.3.2 Overdense Plasmas: Collisionless Absorption

The high energy electrons generated by the high-intensity laser interaction with overdense plasmas are commonly named as *fast* or *hot* electrons. In experiments, when solid targets are irradiated with relativistic pulses of a_0, the typical order of magnitude of the fast electron energy is given by

$$\varepsilon_p = m_e c^2 \left(\sqrt{1 + a_0^2/2} - 1 \right), \tag{2.58}$$

which is also called the "ponderomotive" energy. The process of fast electron generation is however, far from as simple as the motion of a particle in a potential. A satisfactory theory should explain several observations, such as the pulsed nature of fast electron bunch, the conversion efficiency of the laser energy, the dependence on the plasma parameters and the energy spectra of electrons.

We consider an ultrashort, high-intensity laser pulse impinging on a solid target. The ionization and heating of the solid material occurs rapidly enough so that the target can be considered as a plasma with step-like ion density profile $n_i = n_0 \Theta(x)$ since the hydrodynamic expansion is negligible. The EM field will be evanescent inside the overdense plasma according to (2.49) penetrating only in the "skin" layer of thickness ℓ_s defined by (2.52) due to the high electron density ($n_0 \gg n_c$) in the solid material. If $\varepsilon(\omega)$ is real, the reflection is complete and no energy absorption will occur. To obtain the absorption level, we add a friction force $-m_e \nu_c \mathbf{u}_e$ to the equation of motion of electrons so that $\varepsilon(\omega)$ has an imaginary part.

$$\varepsilon(\omega) = 1 - \frac{\omega_p^2}{\omega(\omega + \mathrm{i}\nu_c)}. \tag{2.59}$$

For $(\omega_p/\omega)^2 = n_0/n_c \gg 1$, the absorption coefficient $A \simeq 2\nu_c\omega^2/\omega_p^3$ is obtained from Fresnel formulas (Sect.7.3 of Ref. [38]). The friction is determined by collisions with ions in a classical plasma, so it is called as collisional absorption, or *inverse Bremsstrahlung*, (see Sect.3.4 of Ref. [24]). For a non-relativistic electron with velocity v_e and energy $\varepsilon_e = m_e v_e^2/2$, the collision rate depends on the Coulomb cross section σ_c as $\nu_c = n_i \sigma_c v_e$ where $\sigma_c \propto v_e^{-4} \propto \varepsilon_e^{-2}$. When the average value of ε_e increases, collisional absorption becomes inefficient due to the scaling $\nu_c \propto \varepsilon_e^{-3/2}$ (*runaway effect*). During the interaction of a high intensity laser pulse, ε_e is enhanced and even higher than the thermal energy due to the coherent motion in the field. The collisional absorption decreases while the intensity increases. Therefore, the energy absorption at a high intensity occurs mainly via collisionless mechanisms.

Figure 2.4 briefly gives the sketch of the field and the electron density profile in the skin layer of the over-dense plasma in a class of kinetic mechanisms of collisionless absorption. Due to their thermal energy, the confined electrons attempt to escape at the vacuum side ($x < 0$). On the average, a thin charge separation layer of thickness ℓ_c will be created with $\ell_c \simeq \lambda_D = v_{te}/\omega_p$. Since the spatial scale $\ell_s \gg \lambda_D$ and time scale $\omega^{-1} \gg \omega_p^{-1}$, we may consider that the electrons are instantaneously "reflected" from the sheath field at $x = 0$. Such reflections leads to a non-vanishing absorption and named as *sheath inverse Bremsstrahlung* (SIB)[39]. However, the sheath reflection condition is limited to low intensities when the external field is too weak to drag the electrons into vacuum against the sheath potential.

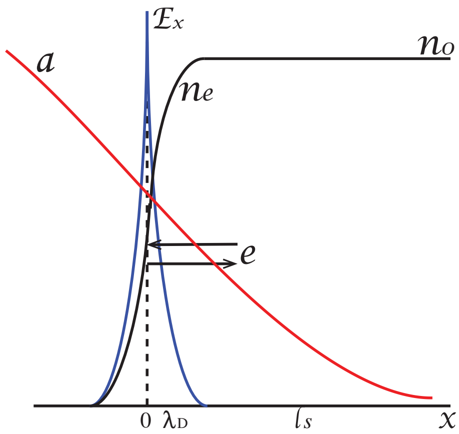

Figure 2.4: The sketch of the electric field and the electron density profiles in the skin layer of a solid-density plasma. The sheath field E_x "reflects" electrons from the bulk.

2.3.2.1 Resonance Absorption

The excitation of resonances in normal modes of a plasma is another general possible route to enhance the absorption and the field in an overdense plasma. The excited plasma oscillations at the critical density surface where $\omega = \omega_p$ is called the basic *resonance absorption* mechanism. The resonance absorption is very effective when the laser pulse is $P-$polarized and obliquely incident onto the plasma density gradient. When the electric field of the incident laser light is in the plane formed by $k-$vector and ∇n_e, i.e. the plane of incidence, the wave is said to be $P-$polarized. In this case, at the turning point E is parallel to ∇n_e. Part of the field can tunnel up to the critical surface. A charge density perturbation may be created and excites a plasma oscillation as shown in Figure 2.5. For a plane wave, the wavevector is $k^2 = k_x^2 + k_y^2$ where the component along the surface is $k_y = (\omega/c)\sin\theta$. By substituting the dispersion relation (2.50) we obtain $\omega^2 = \omega_p^2 + k_x^2 c^2 + \omega^2 \sin^2\theta$ and thus, when $n_e > n_c \cos^2\theta$, $k_x^2 < 0$. k_x being an imaginary number indicates that the EM field will be evanescent in this region.

We begin from Poisson's equation $\nabla \cdot (\varepsilon \mathbf{E}) = 0$ and it follows that

$$\nabla \cdot \mathbf{E} = -\frac{1}{\varepsilon}\mathbf{E} \cdot \nabla\varepsilon = -\frac{1}{\varepsilon}E_z \frac{\partial\varepsilon}{\partial z} \tag{2.60}$$

While in a plasma

$$\nabla \cdot \mathbf{E} = 4\pi e \delta n_e \tag{2.61}$$

where δn_e is the deviation of the electron density from the equilibrium value. If $E_z \neq 0$, the EM wave will induce a density fluctuation. At critical density, the fluctuation has the plasma frequency ω_{pe} and an electron plasma wave is excited. The oscillation can pass through the turning point and reach the critical surface to drive the electron plasma wave. The amplitude of the oscillations depends on the amplitude of the field, and the same issue as the amount of energy transferred by the laser to the plasma wave. For large angle of incidence θ, the reflection surface will be too far from the critical surface, and the region to tunnel will be too long. On the other hand, if θ is too small, the component of $\mathbf{E}$ along the gradient will be small and the electron oscillations will not be driven efficiently. In fact, there is an optimal angle of incidence for given density scalelength $L_n = n_e/|\nabla n_e|$, as a compromise between maximizing the electric field component perpendicular to the plane and its amplitude.

For the $S-$polarized light, $\vec{E}$ is normal to the plane of incidence, there is no component of E along ∇n_e, i.e. $\mathbf{E} \cdot \nabla n_e = 0$, and no plasma wave can be driven.

Using the WKB method, the value of E_z at critical can be expressed in a linear density profile as

$$E_{z(n=n_c)} = \frac{1}{s}\frac{\Phi(\tau)}{\sqrt{2\pi\rho}} \tag{2.62}$$

where s is the imaginary part of the dielectric function describing the EM energy dissipation, $\rho = 2\pi L_n/\lambda$ and $\Phi(\tau)$ the so-called Denisov function. The parameter $\tau = \rho^{1/3}\sin\theta$ describes the angular dependence of E_z. The Denisov function can be approximated as $\Phi(\tau) \approx 2.3\tau\exp(-2\tau^3/3)$ [23].

The absorption fraction can be obtained by integrating the energy lost of the light wave over the density profile as $f_a \approx 1/2[\Phi(\tau)]^2$ [23]. At the maximum of the Denisov function, there is an optimal angle at which the resonance absorption is most efficient [23]:

$$\sin\theta_{max} \approx 0.8\left(\frac{c}{\omega L_n}\right)^{\frac{1}{3}} \tag{2.63}$$

In fact, the angular dependence of the absorption depends on the density profile near critical. At high laser intensity, ponderomotive force steepens the density profile and shortens the distance from turning point to the critical surface. Therefore, resonance absorption is less sensitive to the angle of incidence.

Plasma oscillations obtain a group velocity and propagate as ES waves in the plasma if the temperature is finite. Such longitudinal waves may accelerate a fraction of thermal electrons along the propagation direction and out of the target surface. The electrons acceleration in the *forward direction* will enter the target bulk and will be discussed in the following sections.

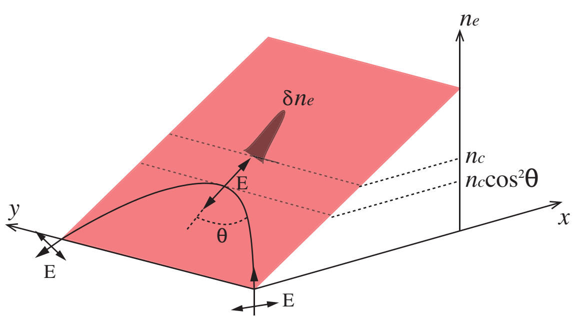

Figure 2.5: Resonance absorption in an overdense plasma. A $P-$polarized EM wave obliquely incident at an angle θ is reflected at the $n_e = n_c\cos^2\theta$ surface. The evanescent field may excite a resonant plasma oscillation at $n_e = n_c$.

The plasma resonance is smeared out if the density gradient is very steep and another normal mode: electron *surface waves* (SWs) or *surface plasmons* appears and propagates along the surface direction with the dispersion relation [21]:

$$k^2c^2 = \omega^2\frac{\varepsilon(\omega)}{1+\varepsilon(\omega)} = \frac{1-\omega_p^2/\omega^2}{2-\omega_p^2/\omega^2}. \tag{2.64}$$

The components of the electric field propagating at the $x = 0$ surface and along the y axis can be written as

$$
\begin{aligned}
E_x &= ikE_0\left[\Theta(-x)\frac{\mathrm{e}^{+q_< x}}{q_<}\Theta(+x)\frac{\mathrm{e}^{(-q_> x)}}{q_>}\right]\mathrm{e}^{-i\omega t},\\
E_y &= E_0[\Theta(-x)\mathrm{e}^{+q_< x}+\Theta(+x)\mathrm{e}^{-q_> x}]\mathrm{e}^{-i\omega t},
\end{aligned}
\tag{2.65}
$$

where $q_> = (\omega/c)(\omega_p^2/\omega^2 - 1)^{1/2}$ and $q_< = (\omega/c)(\omega_p^2/\omega^2 - 1)^{-1/2}$ are the modes of oscillations [21].

The field enhancement and electron acceleration can be achieved by resonant excitation of SWs and the electrons are emitted along the surface direction. However, the phase matching with an incident EM wave is not possible from (2.64) due to the phase velocity $v_p < c$. A direct way out of this difficulty is to use a target with a periodically modulated surface with the wavevector k_g like a grating. Phase matching with an external field of a wavevector component $k_y = (\omega/c)\sin\theta$ requires a condition $k = k_y + nk_g$, with n an integer number and there is a proper angle for a given k_g. This model will be discussed in detail in Section 2.4.2.

The classical collisional and resonance absorption processes described in the previous sections are less efficient when the laser pulse interacts with a very steep plasma profile (or an overdense plasma). This may happen in ultrashort, high-contrast laser pulse interactions with solid targets, when the plasma, created by the pulse's rising edge, does not have time to expand during the pulse. Under these conditions other collisional or collisionless absorption mechanisms are predicted to be important.

2.3.2.2 Normal and Anomalous Skin Effect

In a step-like overdense plasma profile, the laser field can penetrates the plasma to the skin depth

$$
\ell_s = \frac{c}{\omega_{pe}}\left(\frac{\nu_{ei}}{\omega_L\cos\theta}\right)^{\frac{1}{2}}
\tag{2.66}
$$

At low laser intensity ($I < 10^{16}\mathrm{W/cm^2}$), the electrons within the skin layer oscillate in the laser field provided that the electron mean free path $\lambda_e = v_{te}/\nu_{ei}$ is smaller than the skin depth. The electron oscillation energy is thus locally thermalized and the energy dissipation can be achieved through the collisions with ions.

At high laser intensity, the electron temperature increases, resulting in both the electron mean free path and the mean thermal excursion length v_{te}/ω_0 exceeds the skin depth. Under these conditions, collisionless absorption can take place.

The effective collision frequency ν_{eff} is given in this case by the electron excursion time in the anomalous skin layer ℓ_{as}, i.e. $\nu_{\text{eff}} = v_{te}/\ell_{as}$, where $\ell_{as} = (c^2 v_{te}/\omega_0\omega_{pe})^{1/3}$ [23]. For normal incidence in the overdense limit, the absorption fraction is given by $f_A \approx \omega_0\ell_{as}/c$. The angular distribution of the the collisionless absorption fraction can be calculated making use of the Fresnel equations. The absorption is expected to a maximum of 0.7 at grazing incidence and can be improved further by an anisotropic electron distribution function.

2.3.2.3 "Brunel Effect" or "Vacuum Heating"

The resonant absorption is valid only when the density is nearly uniform over the oscillation amplitude. In fact, in very steep density gradients, the resonance absorption mechanism does not exist any longer in its standard form. The amplitude of the resonant plasma waves excited during resonance absorption processes oscillating along the density gradient is [23]

$$X_p \approx \frac{eE}{m_e\omega_0^2} = \frac{v_{os}}{\omega_0} \tag{2.67}$$

In a sharp-edged density profile, X_p is larger than the plasma scalelength L_n, the plasma wave will be destroyed and rebuilt in each cycle and no proper wave oscillation can exist. Brunel has proposed a model for collisionless absorption, referring to "Brunel effect" or "vacuum heating", assuming an infinite gradients of the step-like plasma profile and an external capacitor field extends on the vacuum side. In this model, the electrons are directly heated by the $P-$polarized laser field. The electrons are dragged in vacuum for a half laser cycle, turned around and then re-enter the highly overdense plasma region there delivering their energy.

The Brunel model considers the once-per-laser-cycle pulsed generation of fast electrons with the energy roughly close to the "vacuum" value. The driving field amplitude is equal to the electric field at the surface, $E_d \simeq 2E_L \sin\theta$ in the limit $\omega_p \gg \omega$. The number of electrons per unit surface crossing the interface is $\simeq n_0 u_d/\omega_p^2 \simeq E_d/(4\pi e)$. By assuming that each electron dragged out to the vacuum side re-enters the plasma with a velocity $\simeq u_d$ and a period $2\pi/\omega$, the absorbed intensity is estimated as [23]

$$I_{abs} \simeq \frac{(m_e u_d^2/2)(n u_d/\omega)}{2\pi/\omega} = \frac{eE_d^3}{16\pi^2 m_e\omega} = \frac{eE_L^3 \sin^3\theta}{2\pi^2 m_e\omega}. \tag{2.68}$$

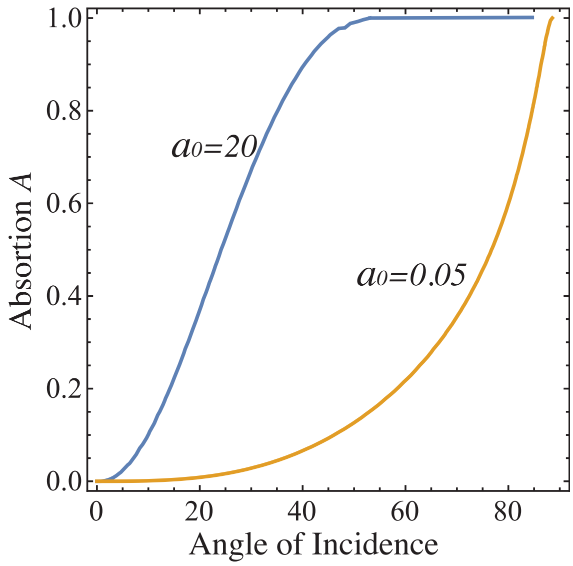

Figure 2.6: Angular dependence of the absorption fraction by vacuum heating mechanism described by (2.69)

By dividing (2.68) with the incident energy flux $I_{inc} = (c/8\pi)E_L^2 \cos\theta$, we obtain an absorption coefficient $A \simeq a_0 \sin^3\theta/\cos\theta$. To obtain a meaningful absorption coefficient $A \leq 1$, the electric field of the incident wave may be written as $E_d \simeq f(A)E_L \sin\theta$ with $f(A) = 1 + \sqrt{1-A}$. Accounting for relativistic intensities, $m_e u_d^2/2$ is replaced by $m_e c^2\left(\sqrt{1+u_d^2}-1\right)$, and the implicit relation becomes [22]:

$$A \simeq \frac{f(A)}{a_0}[(1 + f^2(A)a_0^2 \sin^2\theta)^{1/2} - 1]\frac{\sin\theta}{\cos\theta}. \tag{2.69}$$

Figure 2.6 shows the expression of the angular dependence of A. For $a_0 \ll 1$,

$$A \approx a_0 \frac{f^3}{2\pi}\frac{\sin^3\theta}{\cos\theta} \tag{2.70}$$

the peak appears at grazing angles. For $a_0 \gg 1$,

$$A \approx \frac{f^2}{\pi}\frac{\sin^2\theta}{\cos\theta} \tag{2.71}$$

the angular dependence of A has a broad maximum at smaller angles, in a limit where A is independent on a_0.

The kinetic energy of hot electrons accelerated by the vacuum heating can be estimated as

$$\kappa_B T_{vh} \approx \frac{m_e v_d^2}{2} \approx 3.17\frac{I_L \lambda_L^2}{10^{16} \cdot \mathrm{W/cm^2} \cdot \mu\mathrm{m}^2} \cdot \mathrm{keV}. \tag{2.72}$$

2.3.2.4 Magnetic Force and "$j \times \mathrm{B}$" Heating

The necessary conditions for Brunel vacuum heating are the same as resonant absorption, i.e. oblique incidence and $P-$polarization. Due to the driving force provided by the electric field component perpendicular to the surface, both mechanisms are ineffective for both $S-$polarization and at normal incidence. However, at high laser intensities, the contribution of nonlinear oscillations driven by the magnetic component of the Lorentz force becomes important, and v_{os} will have a component along the k-vector of the laser. Therefore, an absorption mechanism similar to the one predicted by Brunel can take place even at normal incidence, with the difference that the electrons are driven across the vacuum plasma interface by the longitudinal $\mathbf{v} \times \mathbf{B}$ Lorentz force rather than by the $P-$component of the electric field in the electrostatic model. The mechanism is related to the oscillating component of the ponderomotive force

$$F_p = -\frac{m}{4}\frac{\partial}{\partial x} v_{os}^2(z)(1 - \cos 2\omega t) \tag{2.73}$$

The main differences of this mechanism are that the dominant frequency of the driving force is 2ω instead of ω and scales as a_0^2 rather than a_0. For oblique incidence and sufficiently high laser intensities, vacuum heating is predicted to be more significant than $\boldsymbol{j} \times \mathbf{B}$ heating when the driving field is greater than the magnitude of the $\boldsymbol{j} \times \mathbf{B}$ driving field, i.e. for $\sin\theta > (v_{os}/c)(\omega_0/\omega_{pe})$.

With a simple non-relativistic perturbative approach, we assume still a step-like density profile and the normal incidence of an elliptically polarized plane wave of amplitude a_0. The vector potential inside the plasma in the linear approximation can be written as

$$\mathbf{a}(x,t) = \frac{a(0)}{\sqrt{1+\epsilon^2}} \mathrm{e}^{-x/\ell_s}(\hat{\mathbf{y}}\cos\omega t + \epsilon\hat{\mathbf{z}}\sin\omega t), \tag{2.74}$$

where $0 < \epsilon < 1$ is the ellipticity and $a(0) = 2a_0/(1+\mathsf{n})$. The $-e\mathbf{v} \times \mathbf{B}$ force can be written as [21]

$$F_x = -m_e c^2 \partial_x \frac{\mathbf{a}^2}{2} = F_0 \mathrm{e}^{-2x/\ell_s}\left(1 + \frac{1-\epsilon^2}{1+\epsilon^2}\cos 2\omega t\right), \tag{2.75}$$

where $F_0 = 2m_e c^2 |a^2(0)|/\ell_s = (2m_e c^2/\ell_s)(\omega/\omega_p)^2 a_0^2$ from (2.49) and $|1+\mathsf{n}|^2 = (\omega_p/\omega)^2$. The ponderomotive force which can be obtained by averaging one cycle of (2.75), is independent of the laser polarization. The oscillation term in double-frequency 2ω vanishes for circular polarization ($\epsilon = 1$). So there is a quite different laser-plasma coupling between linear and circular polarization at normal incidence.

Proceeding with the perturbative approach, the total electron density is given by

$$\delta n_e = n_0 \frac{2F_0}{m_e \ell_s \omega_p^2} \mathrm{e}^{-2x/\ell_s} \left(1 + \frac{1-\epsilon^2}{1+\epsilon^2} \frac{\cos 2\omega t}{1 - 4\omega^2/\omega_p^2}\right). \tag{2.76}$$

In the case of linear polarization, $\epsilon = 0$, there will be $\delta n_e < 0$ for some time interval. This means that some fast electrons can escape to the vacuum side in that time interval and these fast electron generation is at 2ω rate. For circular polarization ($\epsilon = 1$), the oscillation term in the $-e\mathbf{v} \times \mathbf{B}$ force disappears and there is no fast electrons generated because there is no force driving electrons across the boundary.

2.3.2.5 Magnetic Field Generation

During the high intensity laser-matter interaction, an extremely high, quasi stationary magnetic field is generated in the vicinity of the focal spot. In general, a magnetic field will be created spontaneously where the electrons return to the plasma along a different path and eventually a current loop is created. In short-pulse interactions, B-fields can be generated in at least three mechanisms:

1) *Radial thermal transport*, in which the thermoelectric source term comes from that the electron temperature and density gradients are not parallel, i.e.

$$\frac{\partial \mathbf{B}}{\partial t} = \frac{\nabla T_e \times \nabla n_e}{e n_e} \tag{2.77}$$

2) *DC currents in steep density gradients*, which is driven by temporal variations in the ponderomotive force,

$$\nabla^2 \mathbf{B} \sim \nabla \times \mathbf{J} \sim \nabla n_e \times \nabla I_0. \tag{2.78}$$

where $\mathbf{J} = e n_e \mathbf{v}_p \sim n_e \nabla I_0$ is a net DC ponderomotive current.

3) *Fast electron currents* flowing either along the target surface or into the target with the hot electron flux $n_h v_h$.

Many theoretical publications have been committed to the study of the magnetic field generation and its saturation mechanism in high-density plasmas e.g.

[42, 43]. Here we consider a simplified, "classical" treatment to illustrates the main features of the radial thermal transport mechanism.

The basic equations are the Lorentz-Maxwell equations:

$$\frac{\partial \mathbf{p}}{\partial t} + (\mathbf{v} \cdot \nabla)\mathbf{p} = -e(\mathbf{E} + \frac{1}{c}\mathbf{v} \times \mathbf{B}), \tag{2.79}$$

$$\nabla \cdot \mathbf{E} = 4\pi e(n_0 - n_e), \tag{2.80}$$

$$\nabla \times \mathbf{E} = -\frac{1}{c}\frac{\partial \mathbf{B}}{\partial t}, \tag{2.81}$$

$$\nabla \times \mathbf{B} = -\frac{4\pi}{c} e n_e \mathbf{v} + \frac{1}{c}\frac{\partial \mathbf{E}}{\partial t}, \tag{2.82}$$

$$\nabla \cdot \mathbf{B} = 0, \tag{2.83}$$

where $\mathbf{p} = \gamma m \mathbf{v}$ and $\gamma = (1 + p^2/m^2c^2)^{1/2}$. We begin with the equation of motion for an electron fluid as Eq. (2.79),

$$n_e m_e \frac{\mathrm{d}\mathbf{v}_e}{\mathrm{d}t} = -n_e e\left(\mathbf{E} + \frac{1}{c}\mathbf{v}_e \times \mathbf{B}\right) - \nabla \cdot \mathbf{P}_e + \mathbf{f}^c \tag{2.84}$$

where $\mathbf{P}_e = n_e \kappa_B T_e$ is the electron pressure. The collisional force is in general $\mathbf{f}^c = n_e e(\mathbf{J}/\sigma + \beta \nabla T_e/e)$, where σ is the plasma conductivity and β the thermoelectric power [44]. Due to the small electron inertia, the average forces acting on the electron fluid tent to be unvarying over the characteristics time of the order of the laser pulse duration τ. Under these conditions, we obtain:

$$\mathbf{E} = \frac{\mathbf{J}}{\sigma} - \frac{1}{c}\mathbf{v}_e \times \mathbf{B} - \frac{\nabla P_e}{n_e e} + \frac{\beta}{e}\nabla T_e \tag{2.85}$$

We take the curl of $\mathbf{E}$ using Faraday's law $\dfrac{\partial \mathbf{B}}{\partial t} = -c\nabla \times \mathbf{E}$, we eliminate $\mathbf{E}$ and obtain

$$\frac{\partial \mathbf{B}}{\partial t} = c\nabla \times \frac{\mathbf{J}}{\sigma} + \nabla \times (\mathbf{v} \times \mathbf{B}) + \frac{c}{n_e e}\nabla \times \nabla P_e \tag{2.86}$$

By applying $\nabla \times \mathbf{B} = \dfrac{4\pi}{c}\mathbf{J}$, the first term on the right-hand side becomes

$$-\frac{c}{\sigma}\nabla \times \mathbf{J} = \frac{c^2}{4\pi\sigma}\nabla^2 \mathbf{B} \tag{2.87}$$

Substituting $P_e = n_e \kappa_B T_e$ and using simple vectorial identities, the Eq. 2.86 becomes

$$\frac{\partial \mathbf{B}}{\partial t} = \frac{c^2}{4\pi\sigma}\nabla^2\mathbf{B} + \nabla \times (\mathbf{v} \times \mathbf{B}) + \frac{c\kappa_B}{n_e e}\nabla T_e \times \nabla n_e \tag{2.88}$$

The term

$$\mathbf{S} = \frac{c\kappa_B}{e n_e}\nabla T_e \times \nabla n_e \tag{2.89}$$

in the Eq. 2.88 represents the *thermoelectric* source term, describing the self-generated magnetic fields in a plasma. Its direction is determined by the geometry of the laser-produced plasma and the origin comes from the non-parallel electron density and temperature gradients. The combination of the temperature gradient ∇T_e in the negative radial direction and the density gradient ∇n_e along the direction normal to the target generates a magnetic field which is toroidal around the laser axis, as shown schematically in Figure 2.7.

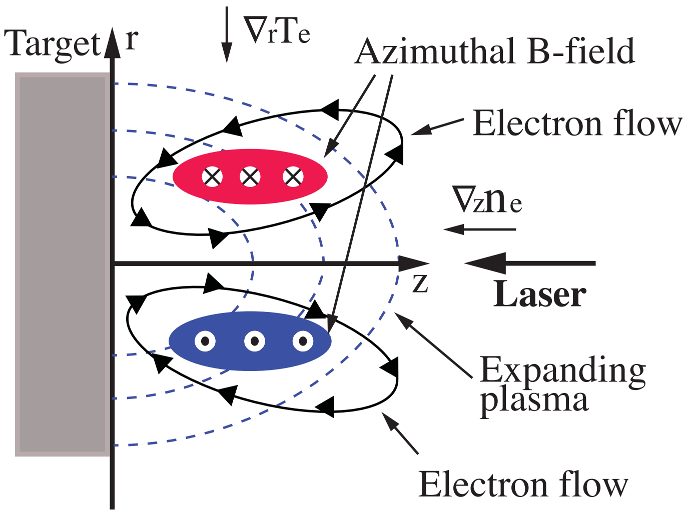

Figure 2.7: Geometry of magnetic field generation through the $\nabla T_e \times \nabla n_e$ mechanism in a laser-produced plasma.

2.4 Surface Fast Electron Acceleration

In this section, two main basic mechanisms for surface fast electron acceleration in laser-plasma interactions, namely *self-induced surface electromagnetic fields* and *surface plasma waves* are introduced. The latter mechanism is discussed in two different regimes: linear and non-linear.

2.4.1 Self-induced Surface Electromagnetic Fields

When the solid target is irradiated by the high intensity ($\sim 10^{18}\mathrm{W/cm^2}$), short (<1 ps) laser pulses, it is expected that the laser energy is transferred to large numbers of high-energy ($\sim$ 100 keV) electrons. These fast electrons have mean free paths of hundreds of micrometers and the scale time of collisional energy loss is of typically a few picoseconds, larger than the laser pulse length. Consequently, fast electrons can transport the absorbed energy to the target region away from the laser spot. The fast electron transport is strongly dependent on the plasma conditions at the surface where the laser energy is absorbed and the temperature to which the target is heated. The fast electron penetration into the target only occurs in the case the solid target can supply an equivalent charge-neutralizing return current. Glinsky [45] and others [46, 47] have shown that electric fields can reduce the penetration depth to a value much less than the mean free path for energy loss. Bell [48] developed a simple model which shows that in many cases such a return current cannot be maintained in the solid and an electric field is generated electrostatically which confines the fast electrons to the surface of the target.

The mechanism of the surface electromagnetic fields generation can be understood as follows. When a solid surface is irradiated obliquely by an intense laser pulse with a steep density gradient, a large number of fast electrons at moderate energies are produced due to the "vacuum heating" or $\boldsymbol{j} \times \mathbf{B}$ heating. The accelerated electrons propagate along the laser incidence direction and induce magnetic fields along the target surface. When the magnetic fields are sufficiently intense, a large fraction of fast electrons will be reflected back to the vacuum. The consequent negative space charge in the vacuum drive the fast electrons back to the target. These electrons are therefore confined on the surface, generate the surface current and enhance the surface magnetic field. Such quasistatic magnetic fields at the front surface are unipolar and become stronger with time even after the main pulse is fully reflected, of which the peak moves forward along the target surface. Meanwhile, the quasistatic electric fields have two peaks which locate in and outside of the target, respectively. The presence of these quasistatic electromagnetic fields take significant effects on the high energetic electron generation [43].

An analytical model was proposed in [42] to describe the surface electromagnetic fields and will be discussed in the following. The schematic of the analytical model is shown in Figure 2.8. The $P-$polarized laser pulse irradiates the solid target obliquely with the incidence angle α where $z \leq 0$ is vacuum. As shown in the right figure, the surface electron current, which is induced by a nonuniform magnetic field, is assumed in $-x$ direction and the surface magnetic field is in $+y$ direction. The magnetic field is defined by the vector potential as $B_y(z) = \dfrac{\partial A(z)}{\partial z}$ and the initial momentum of the fast electrons is $(p_x, p_z)_{z=0} = (p_{\text{in}} \sin\alpha, p_{\text{in}} \cos\alpha)$. The fast electrons are injected by the laser field toward the target and then bent by the magnetic field. According to the canonical momentum and energy conservation in the x direction, the momenta become:

$$
\begin{aligned}
p_x(z) &= p_{\text{in}} \sin\alpha + e[A(z) - A(0)], \\
p_z(z) &= \pm\sqrt{p_{\text{in}}^2 - \Big[p_{\text{in}} \sin\alpha + e[A(z) - A(0)]\Big]^2}.
\end{aligned}
\tag{2.90}
$$

The injected electrons will be reflected by the surface magnetic field at $z = z_{ref}(p_{\text{in}})$ when $p_{\text{in}} \leq [A(z_{ref}) - A(0)]/(1 - \sin\alpha)$. The densities of electron charge and the surface current can be obtained as

$$
\begin{aligned}
n(z) &= -e \int f(\boldsymbol{p}, z) \mathrm{d}\boldsymbol{p} \\
&= -e \int_\Omega f_0(\boldsymbol{p}_{\text{in}}, z = 0) \frac{\partial(p_x, p_z)}{\partial(p_{\text{in}x}, p_{\text{in}z})} \mathrm{d}\boldsymbol{p}_{\text{in}}, \\
J_s(z) &= -e \int_\Omega \frac{p_x(z)}{m\gamma} f_0(\boldsymbol{p}_{\text{in}}, z = 0) \frac{\partial(p_x, p_z)}{\partial(p_{\text{in}x}, p_{\text{in}z})} \mathrm{d}\boldsymbol{p}_{\text{in}},
\end{aligned}
\tag{2.91}
$$

where e, m and γ are the elementary charge, electron mass and the Lorentz factor, respectively, and Ω is the domain of the initial momentum for the reflected electrons. $A(0) = 0$ is chosen for simplicity. The surface current density can be obtained according to the water-bag model [49] which assumes that the momentum distribution of incoming electrons is uniform in $0 \leq p_{\text{in}} \leq p_{max}$ as

$$
\begin{aligned}
J_s(z) &= -\frac{e n_s p_{\text{max}}}{m} \int_0^1 \frac{(p_{\text{in}} \sin\alpha + A) p_{\text{in}} \cos\alpha \mathrm{d}p_{\text{in}}}{\sqrt{1 + p_{\text{in}}^2} \sqrt{p_{\text{in}}^2 - (p_{\text{in}} \sin\alpha + A)^2}}, \\
&\equiv -\frac{e n_s p_{\text{max}}}{m\gamma_0} J'_s(z),
\end{aligned}
\tag{2.92}
$$

where n_s is the number density of the electrons forming the surface current. We define L the depth of the surface current and the solid density of the target is located at $z \geq L$. Using the conservation of the canonical momentum, the return current is written as

$$J_{\text{ret}}(z) = \frac{n_r e^2}{m}[A_m - A(z) + A_0], \tag{2.93}$$

where n_r is the number density of the background plasma and $A_m = A(z = \infty)$.

The spatial profile of the surface magnetic field is obtained to be the surface and return currents:

$$\frac{\partial^2 A(z)}{\partial z^2} = \begin{cases} J_s'(z), & 0 \le z < L, \\ J_s'(z) - \frac{n_r}{n_s}(A_m - A + A_0), & L \le z. \end{cases} \tag{2.94}$$

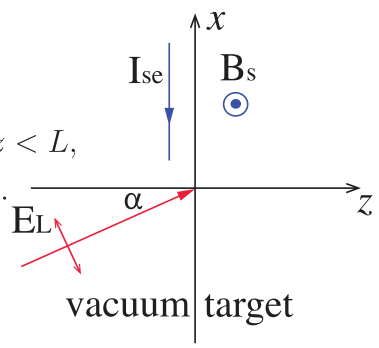

Figure 2.8: Schematic of the analytical model in [42].

Here z is normalized by z/ℓ_s and $\ell_s = c/(e\sqrt{n_s/m\gamma_0\varepsilon_0})$. Eq. (2.94) can be solved with the boundary conditions of $A(0) = A'(0) = 0$ and $A(\infty) = A_m$, $A'(\infty) = 0$.

Figure 2.9 shows the spatial profile of the vector potential (solid line), magnetic field (dashed line) and electrostatic potential (broken line) with $\gamma = 6.1$, corresponding to $a_L = 6$. The maximum of surface magnetic field is located at the target surface while for the electrostatic field, the maximum is outside the current surface region. It is also notable that compared with the surface magnetic field, the electrostatic field is much smaller and can be negligible in treating the electron motion inside the surface region. The return current is localized within the skin depth of the plasmas and the thickness of the magnetic field layer is equal to L.

2.4.2 Surface Plasma Waves: Linear Regime

Another acceleration mechanism of electrons propagating close to the direction along the target surface can be associated with the acceleration by surface plasma waves (SPWs) [25, 30]. Recently, analytical theories and numerical simulations [25–27] indicate that the electron acceleration can be improved by the resonant SPWs excitation with the periodically modulated surface targets (gratings). In the experiments, a laser pulse with high prepulse-to-pulse contrast ($\le 10^{-11}$) allows to preserve the surface structures and create a sharp-edged overdense plasma. By employing a double plasma mirror laser system with ultrahigh contrast (10^{-12}), protons with higher energies [29] and a strong electron emission with energies exceeding 10 MeV [30] were produced via resonant excitations of a SPW in a grating target. However, the prior theoretical and experimental studies placed the main emphasis on the linear regime of SPWs. The derivation in this section follows Sgattoni [27].

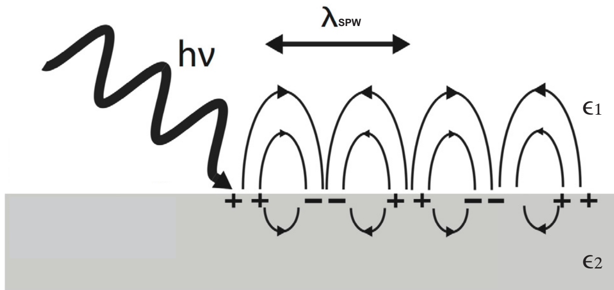

Figure 2.10: Schematic of the surface oscillation mode of the electrons at the steep vacuum-metal interface.

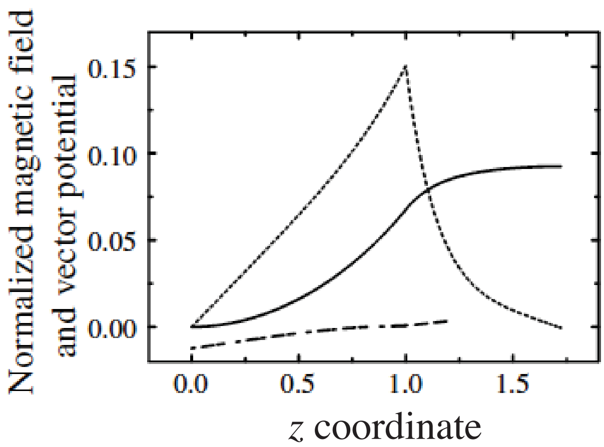

Figure 2.9: The spatial profile of the vector potential, magnetic field and electrostatic potential solved from Eq. (2.94) [42].

SPWs are electron oscillation modes excited at a steep vacuum-plasma interface. They are confined in a small region across the boundary and propagate along the surface (Figure 2.10). The dispersion relation of SPWs reads

$$k_{SPW}(\omega) = \frac{\omega}{c}\sqrt{\frac{\epsilon_1\epsilon_2}{\epsilon_1+\epsilon_2}}, \tag{2.95}$$

where ϵ_1 and ϵ_2 are the dielectric constants of the vacuum and the plasma, respectively, c the speed of the light, ω and k_{SPW} are the frequency and the wavenumber of the SPW. The dielectric constant of the vacuum $\epsilon_1 = 1$. Within the linear theory, the electrons in the plasma are non-relativistic and the dielectric constant of the plasma becomes

$$\epsilon_2(\omega) = 1 - \frac{\omega_p^2}{\omega^2} \tag{2.96}$$

where $\omega_p = \sqrt{e\pi n_e e^2/m_e}$ is the plasma frequency with n_e, e and m_e the electron plasma density, the elementary charge and the mass of an electron, respectively.

The dispersion relation of the SPW now depends solely on the plasma frequency ω_p and becomes

$$k_{SPW} = \frac{\omega}{c}\sqrt{\frac{\omega_p^2 - \omega^2}{\omega_p^2 - 2\omega^2}} \tag{2.97}$$

With the phase-matching conditions, a laser pulse with the frequency ω_L can be utilized to excite a SPW resonantly. When metal grating surfaces with a periodic modulation λ_g are employed, the phase-matching condition reads

$$k_{L,\parallel} = k_{SPW}(\omega) \pm n\frac{2\pi}{\lambda_g}. \tag{2.98}$$

$k_{L,\parallel} = \frac{\omega}{c}\sin\alpha$ with α the angle of incidence. We restrict to the solution with $n = -1$ and the condition for resonant excitation of a SPW on a grating by an incident EM wave with the same frequency (neglecting thermal, collision and relativistic effects) is

$$\lambda_L/\lambda_g = \sqrt{\frac{1-\eta}{2-\eta}} - \sin\alpha, \tag{2.99}$$

where λ_g being the grating period and $\eta = (\omega_p/\omega)^2 = n_e/n_c$, with ω_p being the plasma frequency and n_c the critical density. Within this linear model, a grating target of periodicity $\lambda_g = 2\lambda_L$ at $\alpha = 30°$ matches the SPW resonant condition for $\eta \gg 1$.

2.4.3 Surface Plasma Waves: Nonlinear Regime

Recently, Liu *et. al* [31] have developed a new model which includes relativistic and ponderomotive nonlinearities to explain the target normal sheath acceleration of protons at high intensity in the presence of a preformed plasma on gratings. The mode structure shows that the amplitude of surface plasma waves (SPWs) excited by a $P-$polarized laser pulse on a rippled target is larger than the transmitted laser amplitude. The relativistic increase in electron mass and ponderomotive force leads the electron density modification, which eventually modifies significantly the field structure of the SPWs. The derivation [31] will be discussed in the following in detail.

The schematic in Figure 2.11 shows the SPW propagating along the overdense plasma-vacuum interface of which the amplitude is

$$E_x = F(z)\mathrm{e}^{-\mathrm{i}(\omega t - k_x x)}. \tag{2.100}$$

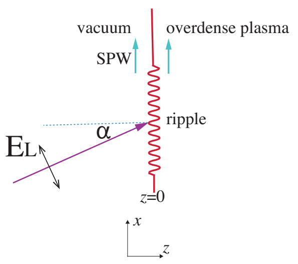

Figure 2.11: Schematic of the analytical model in [31]

Considering $\nabla \cdot \vec{E} = 0$, the wave equation in vacuum ($z < 0$) gives:

$$\begin{aligned} F(z) &= A\mathrm{e}^{\alpha_I z}, \\ E_z &= -\frac{\mathrm{i}k_x}{\alpha_I} A\mathrm{e}^{-\mathrm{i}(\omega t - k_x x)}, \\ \alpha_I &= (k_x^2 - \omega^2/c^2)^{1/2}. \end{aligned} \tag{2.101}$$

While for $z > 0$, the wave equation is

$$\begin{aligned} \nabla^2 \vec{E} - \nabla(\nabla \cdot \vec{E}) + \frac{\omega^2}{c^2}\varepsilon \vec{E} = 0, \\ \varepsilon = 1 - \frac{\omega_p^2 n_e}{\omega^2 \gamma n_0} \end{aligned} \tag{2.102}$$

For $\omega^2 \ll \omega_p^2$, the wave equations in $x-$component can simplify to

$$\frac{\mathrm{d}^2 F}{\mathrm{d}z^2} + (\frac{\omega^2}{c^2} - k_x^2)F - \frac{\omega_p^2 n_e}{c^2 \gamma n_0} F = 0. \tag{2.103}$$

The magnetic field can be written as

$$\vec{B} = \hat{y}\frac{1}{\mathrm{i}\omega}\frac{\partial F}{\partial z}\exp[-\mathrm{i}(\omega t - k_x x)]. \tag{2.104}$$

After some algorithm processing, the author gave the nonlinear dispersion relation

$$\begin{aligned} \alpha_I &= \frac{a_0(\omega^2/c^2 - k_x^2/\varepsilon)\Big[1 + (a_0^2/2)/(1 + a_0^2/2)\Big]^{1/2}}{\Big[4(\omega_p^2/c^2)\Big((1 + a_0^2/2)^{1/2} - 1\Big) - (\omega^2/c^2 - k_x^2)a_0^2\Big]^{1/2}} \\ &\cong \frac{\omega^2 a_0}{2\omega_p c}\frac{(1 + a_0^2)^{1/2}}{(1 + a_0^2/2)^{1/2}\Big[(1 + a_0^2/2)^{1/2} - 1\Big]^{1/2}}, \end{aligned} \tag{2.105}$$

where the propagation constant k_x is

$$k_x = (\omega^2/c^2 + \alpha_I^2)^{1/2} \cong \omega/c + \alpha_I c/\omega. \tag{2.106}$$

It is noteworthy that the field decay constant in vacuum α_I is remarkably modified at large SPW amplitude.

The ratio of SPW to laser amplitude is calculated as [31]

$$\left|\frac{A_1}{A_L}\right| = \frac{\omega^2 h r_0}{c^2}\frac{(\Omega_p^2-1)^{3/2}}{(\Omega_p^2-2)^2}\frac{1+\sin\alpha(\frac{\Omega_p^2-2}{\Omega_p^2-1})^{1/2}}{\left[1+\frac{(\Omega_p^2-1)^2}{\Omega_p^2\sec^2\alpha-1}\right]^{1/2}}, \tag{2.107}$$

where $\Omega_p = \omega_p/\omega$, h is the surface ripple depth, r_0 the focal spot size of the laser and $A_L = A_0 \sec\alpha$. In this expression, it is clear that the amplitude of SPWs scales linearly with the depth of the surface ripple and laser focal spot size, and nonlinearly with Ω_p.

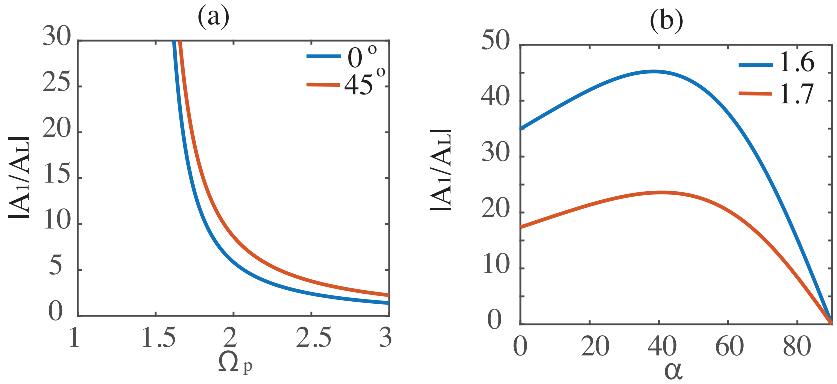

Figure 2.12: The amplitude ratio of the SPW field to the laser field obtained from Eq. (2.107) as a function of (a) Ω_p for the angle of incidence $\alpha = 0$ and 45° and (b) α for $\Omega_p = 1.6$, 1.7. Here $\omega r_0/c = 30$, $\omega h/c = 0.3$.

Figure 2.12 shows the variation of amplitude ratio of the SPW field to the laser field as different value Ω_p (a) and incidence angles (b) deduced from Eq. (2.107). In Figure 2.12(a), it is shown that the amplitude ratio decreases with Ω_p at both laser incidence, normal and oblique. When $\Omega_p = \sqrt{2}$ at the surface plasmon resonance, the amplitude ratio is high, only limited by the damping of the SPW. While in Figure 2.12(b), when $\Omega_p = 1.6$ and 1.7, the amplitude increases firstly with the angle of incidence, attains a maximum at $\alpha = 45°$ and decreases to zero at grazing incidence ($\alpha = 90°$). At $\omega_p^2 \gg \omega^2$, the nonlinear mode structure indicates that the behaviour of SPW is only barely affected by nonlinearity.

2.4.4 Electron Acceleration in Thin Foil Target

Now we consider the interaction of an intense laser pulse ($I > 10^{18}\mathrm{W/cm^2}$) with a solid thin foil target. The interaction process can be described as follows. The intense laser pulse irradiates a thin foil target with a thickness of few microns. A preplasma is created on the target front side due to the laser prepulse. The main pulse interacts with the plasma and accelerates electrons in the forward direction to the energy of few MeV due to the direct action of the ponderomotive force. Unlike the case of bulk target, this cloud of hot electrons propagates through the bulk and escape into the vacuum behind the target, producing an negative charged sheath as shown in Figure 2.13. The electrostatic field with the order of the laser electric field ($\sim$ TV/m) due to the charge separation in the sheath is almost normal to the surface. The ions can then be accelerated in this sheath field in the target normal direction. The derivation in this section follows Macchi [21] and Roth [32].

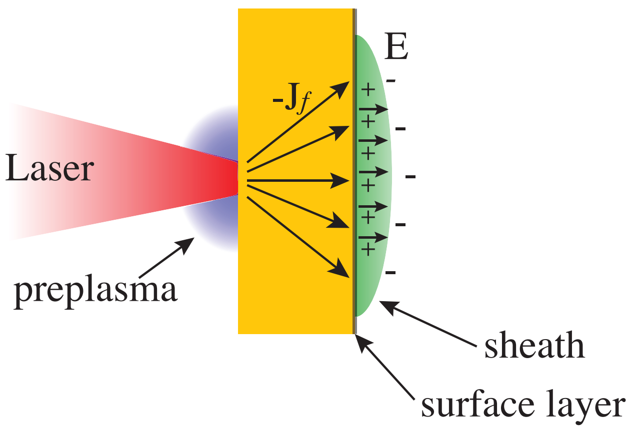

Figure 2.13: The intense laser pulse interacts with thin foil target and the charge separation forms.

The number of electrons generated by the laser pulse is larger than 10^{10} (depending on the target thickness). The electrons are accelerated and transported through the target bulk to its rear side, which results in the broadening in transverse extension. The size of the electron sheath can be estimated by

$$r_{sheath} = r_0 + d\tan(\theta/2) \tag{2.108}$$

where r_0 is the radius of the laser spot, d the target thickness, and θ the electron sheath's angle to the laser focal spot, i.e. the broadening angle of the electron distribution. The electrons are assumed to have an exponential energy distribution

$$n_{hot}(E) = n_0 \exp(-\frac{E}{k_B T_{hot}}) \tag{2.109}$$

with the temperature $k_B T$ and overall density n_0. The electron density at the target rear side then can be given as

$$N_{e,0} = \frac{\eta E_L}{c\tau_L \pi (r_0 + d\tan\theta/2)^2 k_B T_{hot}}, \tag{2.110}$$

where η is a scaling with intensity as $\eta = 1.2 \times 10^{-15} I_L^{0.74}$($I_L$ in the unit of W/cm^2), E_L the laser electric field $E_L = \sqrt{2I_L/\varepsilon_0 c}$, c the light velocity, τ_L the laser pulse duration. The electron temperature can be obtained with a practical notation based on the ponderomotive scaling as:

$$k_B T_{hot} = m_0 c^2 \Big(\sqrt{1 + \frac{I_L[\mathrm{W/cm^2}]\lambda_L^2[\mu\mathrm{m}^2]}{1.37 \times 10^{18}}} - 1 \Big). \tag{2.111}$$

The electron angular broadening θ (FWHM) and the electron density at the target rear side $n_{e,0}$ for electrons with mean energy $k_B T$ can be estimated from above Eqs. (2.108−2.111).

The electrons reach the rear side of the target and escape into the vacuum, leading to an electric potential Φ in the vacuum region due to the charge separation. Assuming a step-like ion density profile at the rear side $n_i = (n_0/Z)\Theta(-x)$ and Boltzmann equilibrium condition for electrons, the Poisson's equation describing the static sheath becomes

$$\varepsilon_0 \frac{\partial^2 \Phi}{\partial x^2} = e(n_e - Z n_i) = e\pi e n_{e,0} \Big[\exp(\frac{e\Phi}{k_B T_e}) - \Theta(-x) \Big]. \tag{2.112}$$

Here the electron kinetic energy is replaced by the potential energy $-e\Phi$. The initial electron density $n_{e,0}$ is taken from Eq. (2.110). If the plasma is globally neutral, integration of the above equation from $-\infty$ to $+\infty$ is zero. For the electrostatic potential, $\Phi(-\infty) = 0$ and $\Phi(+\infty) = -\infty$. A possible way out of this difficulty is to assume that there is a upper cut-off electron energy $\bar{\varepsilon}$ rather than infinite, which is physically reasonable in general. In such a case $\Phi(+\infty) = -\bar{\varepsilon}$

limits the maximum energy gain of ions.

To find the solution of Eq. 2.112 in the vacuum ($x \geq 0$), we switch to dimensionless quantities $\xi = x/\lambda_D$, $\phi = e\Phi/T_e$, and $E = eE_x\lambda_D/T_e$ for convenience, where $\lambda_D = (\varepsilon_0 k_B T_{hot}/e^2 n_{e0})^{1/2}$ is the electron Debye length and we obtain

$$\phi = -2\ln(\xi/\sqrt{2} + e), \qquad E = 2/(\xi + \sqrt{2}e). \tag{2.113}$$

If we also assume that there is a cut-off energy uT_e with $u > 0$ in the electron energy distribution, the analytical solution reads

$$\begin{aligned} \phi &= -u + \ln(1 + \tan^2((\xi - \xi_r)\mathrm{e}^{-u/2}/\sqrt{2})), \\ E &= \sqrt{2}\mathrm{e}^{-u/2}\tan((\xi - \xi_r)\mathrm{e}^{-u/2}/\sqrt{2}). \end{aligned} \tag{2.114}$$

where ϕ does not diverge but becomes constant at some distance $x_r = \xi_r\lambda_D$ from the surface. The above static sheath model can reproduce the observed scalings for the cut-off energy of protons in good accuracy.

Chapter 3

Experimental Setup and Diagnostics

This chapter presents the experimental arrangements and the diagnostic methods which were used for the experiments in this dissertation. The Arcturus laser system and its components are described firstly, followed by the plasma mirror system which is necessary to improve the temporal profile of the laser pulse. The temporal laser contrast ratio and the focal spots with and without plasma mirror are measured and compared.

The following sections of this chapter primarily introduce the targets used in the experiments, the setup of absorption measurements and electron detection methods. The detailed calibration methods of the Fuji BAS-TR image plates (IP) will be given. At the end of this chapter, the Particle-in-cell (PIC) codes EPOCH used to simulate the experiments in Chapter. 6.1 will be introduced in detail.

3.1 Arcturus Laser System

The Arcturus laser, located at the Heinrich-Heine University in Düsseldorf, is a commercially available table-top, Ti:sapphire-based, high power laser system which is based on the chirped pulse amplification (CPA) scheme. A few key components of the laser system are described in the following similar as in[56] and can be found in the schematic of figure 3.1. The Kerr-lens mode-locked Synergy oscillator pumped by a 5W continuous wave (cw) provides pulses with the repetition rate of 76 MHz, energy of 5 nJ and pulse duration of 23 fs. The central wavelength is around 790 nm with a corresponding bandwidth of $\sim$ 96 nm. The

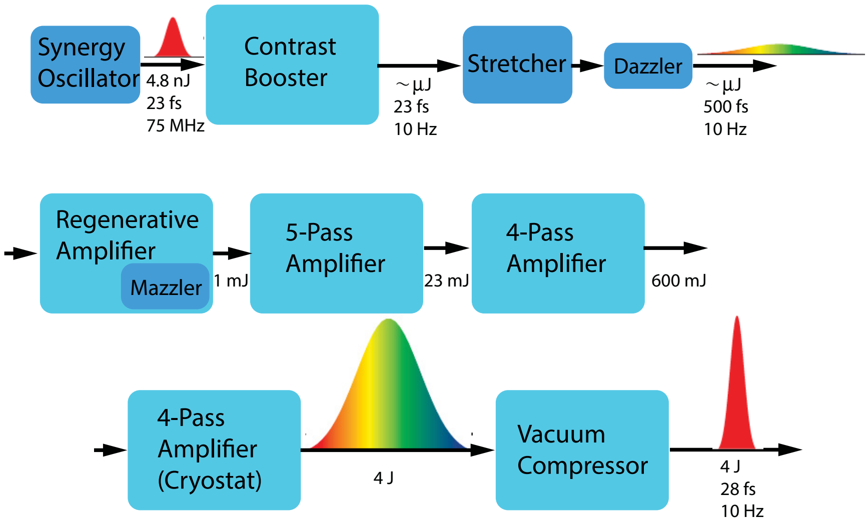

Figure 3.1: Overview of the Arcturus laser system at the Heinrich-Heine University Düsseldorf. The laser pulse is generated in the Oscillator and then stretched, amplified and compressed to a final pulse with 4 J, 28 fs and 10 Hz.

ultrashort laser pulse is then amplified to microjoule level with the enhanced temporal contrast and picked to 10 Hz in a booster amplifier. A saturable absorber cleans the pulse from amplified spontaneous emission (ASE) at the same time. Afterwards, the pulse is stretched out in time to $\sim$ 500 ps in the stretcher module. Inside the stretcher, an acousto-optical modulator called Dazzler is settled to compensate the group velocity dispersion in order to have a flat and minimum phase pulse, the contrast of which can be improved via compression in the later stages. The phase of the pulse can be controlled and adjusted by a computer programme.

The pulse passes through a regenerative amplifier with the energy up to 1mJ, first 5-multipass amplifier to 23 mJ, second 4-multipass 2A amplifier to 600 mJ, which are all pumped by double-frequency Nd:YAG lasers. The final amplification is done in a titanium-doped sapphire crystal ($5 \times 5 \times 3$ cm^3) which is pumped by four double-frequency *Propulse* Nd:YAG lasers with 8 J (2 J each). The beam diameter is 3.3 cm. After this amplification, the pulse energy is 4 J and the beam is expanded by a telescope to a final diameter of 8 cm. The transmission efficiency of the compressor is $\sim 60\%$ hence $\sim$ 2.5 J laser energy are delivered to the target.

The vacuum compressor consists of two gold coated gratings which are parallel. By changing the vertical level of the beam path, the pulse passes through each of the grating twice and can be compressed down to 28 fs.

The temporal distribution of the laser intensity can be experimentally measured by a *SEQUOIA* apparatus (Amplitude Technologies, France) which is a high dynamic range third-order cross-autocorrelator allowing to measure the laser pulse contrast on 100s of picosecond time scale. Figure 3.2 shows the typical Arcturus laser pulse temporal profile after the vacuum compressor measured by the *SEQUOIA*. The diagnosis reveals that after compression, the contrast ratio of the laser pulse is $\sim 10^{-10}$ for the ASE pedestal, at 100 ps before the main pulse and about 10^{-6} for the prepulses at 10 ps before the main pulse.

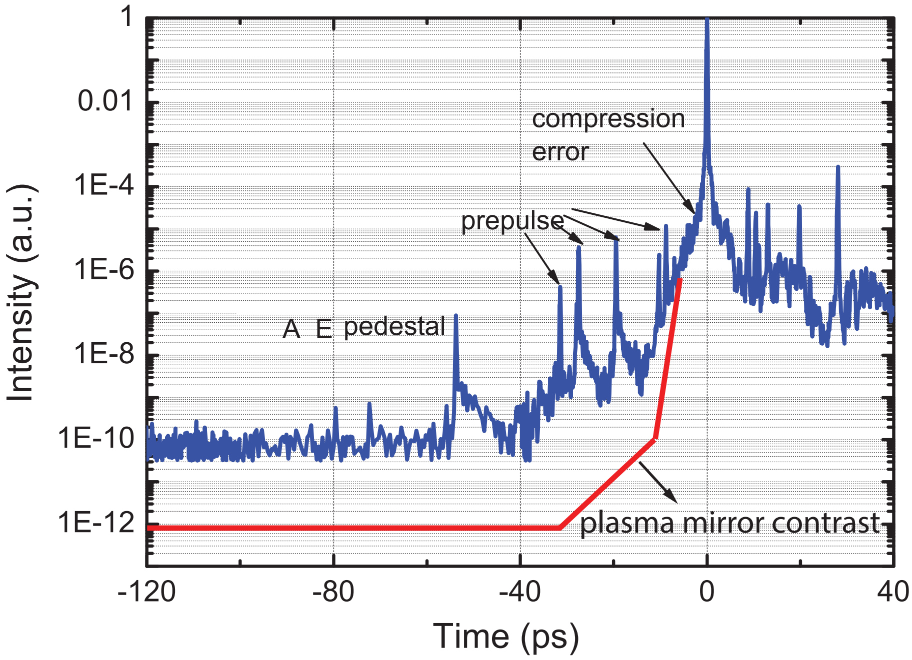

Figure 3.2: A typical temporal profile of the Arcturus laser pulse after the vacuum compressor measured by a *SEQUOIA* (blue line). The red line is the estimated laser contrast after the plasma mirror.

3.2 Plasma Mirror of Arcturus Laser System

When a laser pulse is focused to an intensity above $10^{20}\mathrm{W/cm^2}$, prepulses of six orders less intense can already ionise the target and generate an overdense preplasma which will reflect the laser pulse at the critical density. However, when the targets are thin foils (thickness 10s nm) or modulated structure ($\sim$ 10s nm), the preplasma will destroy such targets completely before the main pulse arrives.

In order to perform the laser-solid interaction in a small scale length of the pre-plasma, a laser contrast improvement is required. A plasma mirror system (PM) was designed to improve the temporal contrast of the Arcturus laser pulse, considering the laser pulse duration and intensity, the space limitation of the laser room and the feasibility of the PM target replacement.

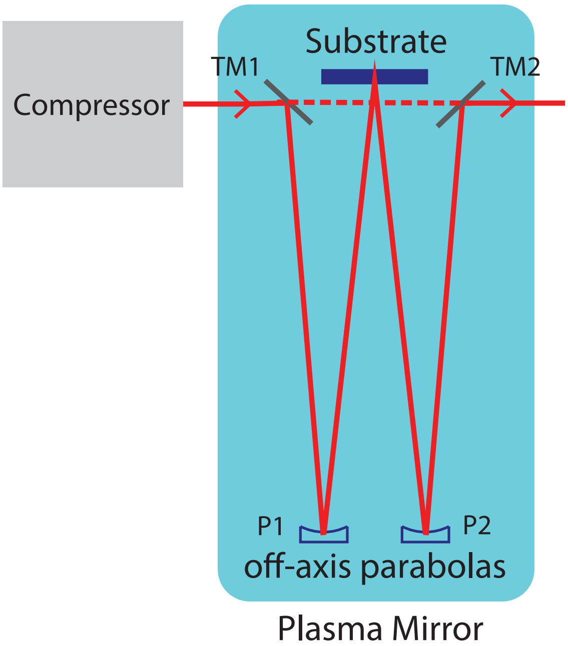

Figure 3.3: Sketch of the plasma mirror setup in the Arcturus laser system. The laser beam, coming from the compressor is redirected by the turning mirror TM1 to the parabolic mirror P1 and focused onto the PM substrate. Afterwards, it is re-collimated by a second parabolic mirror P2 and re-enters the beam path via the turning mirror TM2.

Figure 3.3 sketches the plasma mirror setup. The pulse is first directed to a long focal length (f=1524mm) off-axis parabolic mirror P1 by a six-inch turning mirror TM1, which can be moved in and out of the beam path controlled by a motor. The four-inch parabola focuses the pulse beam onto a dielectric substrate coated with anti-reflective material. The ASE and prepulses with lower intensities pass through the substrate before the main pulse arrives at the anti-reflective coating. Before the main pulse reaches the substrate, an overdense plasma on the surface of the substrate is generated, which acts as a mirror and will reflect most of the main laser pulse. The radius of the focal spot on the substrate is 350 μm and the main pulse intensity is around $2\times10^{16}\mathrm{W/cm}^2$. The angle of the incidence on the PM substrate is close to normal (2.4°) to reduce the laser energy loss due to the resonance and Brunel absorption.

After the reflection, the second off-axis parabolic mirror P2 re-collimates the beam and the second turning mirror TM2 redirects the beam into the beam line again. The coating at the focus position on the substrate is damaged after each shot. This damaged spot can also prevent the back-reflected laser beam for re-turning to the compressor and main amplifiers. This is in particular important for experiments when the laser is normal incident onto the target and the back reflected laser light can be significant.

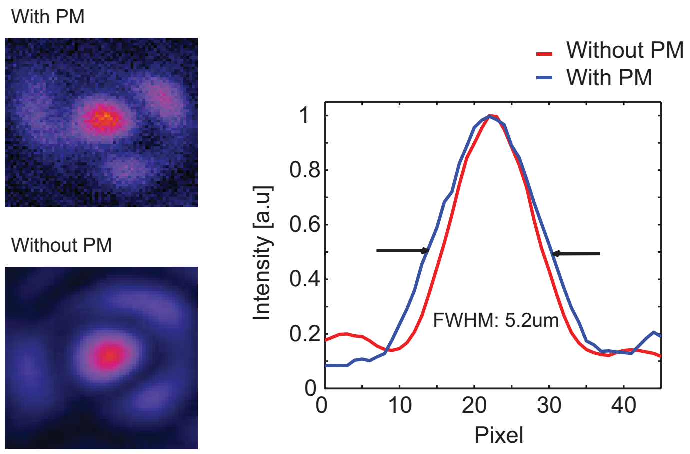

Figure 3.4: 2D images of the focal spot recorded by a CCD camera and beam profiles with and without the plasma mirror. The FWHMs of the focus diameter are $\sim 5.2\mu$m in both cases.

The spatial profiles of focal spot with and without PM are investigated by a microscope lens with $10\times$ magnification and imaged onto a CCD camera shown in Figure 3.4. Spatial profiles of the focal spots are quite similar for the operation with and without the plasma mirror. About 50% of the total laser energy is coupling onto a focal spot with a diameter of 5.2μm (FWHM) when the PM is included.

The laser contrast is expected to be improved by two orders of magnitude on a ns and ps time scale after the plasma mirror as shown in Figure 3.2 (red line). One can estimate in this case that the contrast is around 10^{-12} at 100 ps and 10^{-8} at 10 ps before the laser pulse maximum.

3.3 Absorption Measurements' Setup

The absorbed laser energy fraction by the solid targets was measured by the experimental arrangement shown in Figure 3.5. The laser beam is guided onto the target in the experimental chamber by a number of high-reflectivity (HR) dielectric mirrors after leaving the compressor (and plasma mirror). The laser beam was focused by a gold coated 90° off-axis parabola (*OAP*) with an f-number = 2 and an effective focal length of 152.4mm. The laser beam is linearly polarized and focused onto the target with a spot diameter of $\sim$5 μm (FWHM).

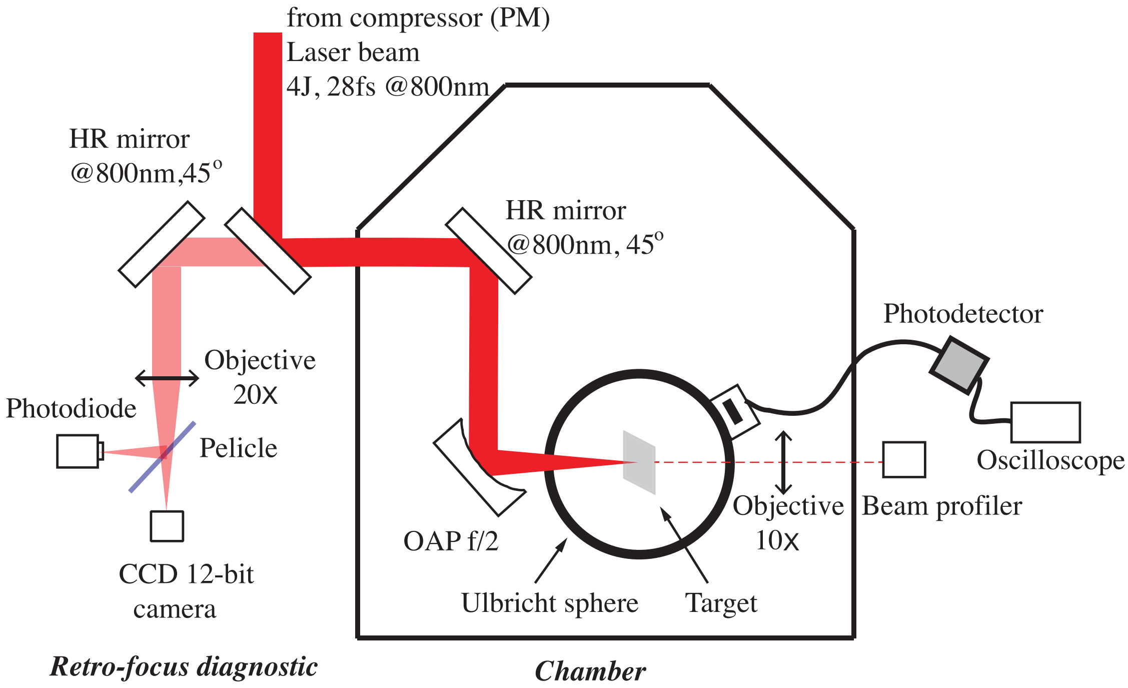

Figure 3.5: Schematic of the set-up for the absorption experimental investigations.

The main component of the setup is an Ulbricht (integrating) sphere with 20 cm in diameter. The inner wall of the sphere was coated by a diffusive and high-reflectivity Barium Sulphate($BaSO_4$) paint. The Barium Sulphate paint has a high reflectivity, better than 95% over a large wavelength range (400-1200nm) with a Lambertian angular scattering distribution and long-term stability.

There are three open ports with a diameter of 5 cm on the sphere surface. One is the entrance port of the laser pulse into the sphere. A micro objective with $10\times$ magnification is mounted through the port on the opposite side to monitor the focal spot. The third port at the normal direction to the laser propagation axis provides access to the target holder arm which controls the target and can move the target in three directions with an accuracy of 1μm and rotate continuously 360° with an accuracy of 0.1° by a motor. The second port for the micro objective will be closed during the measurement. An optical fiber bundle connects the sphere to a high-speed photodiode which records the signal of the reflected light energy read out by an oscilloscope.

Two separated focus diagnostics are integrated in the main experimental arrangement. In Figure 3.5, the first setup consists of a remotely controlled motorised microscope objective with $10\times$ magnification connected with an 8 bit *CCD* camera or 12 bit beam profiler to image the laser focus. A typical 2D image of the focal spot recorded with the beam profiler is presented in Figure 3.4.

In left part of the Figure 3.5 an additional setup is shown, named retro-focus diagnostic. This system is implemented in order to monitor the focus quality when aligning the target. The solid target reflects the laser beam and a small fraction of the back reflected laser beam will pass through the last dielectric turning mirror which is mounted in the beam line before entering the target chamber, the achromat lens (f_a=25cm) and the microscope objective (20$\times$), then is aligned onto a 12-bit *CCD* camera. The retro-focus diagnostic allows the visual control of the target position in the focal plane before each shot in the case of absorption measurements, as long as the target is placed in the Ulbricht sphere and there is no other method to take a direct sight of the interaction zone during the experiment. A fraction of back-reflected radiation is guided to a photodiode by a pelicle which is placed before the 12-bit *CCD* camera in order to measure the light leaked through the laser entrance port.

By attaching the photodetector at the Ulbricht sphere, the reflected (specular and scattered) fraction of laser energy *R* is measured, allowing to determine the amount of the absorbed energy fraction *A* via the formula: A=1$-$$R$. The fraction of the total area of the two ports to the total sphere area F_p is roughly 0.03. Considering the multiple reflections and losses through the opening ports, the average reflectivity is determined by

$$\bar{\rho} = \rho_0(1 - F_p) + \rho_p F_p \tag{3.1}$$

where ρ_0 is the sphere paint reflectivity, ρ_p is the reflectivity of the opening ports. Taking into account the particular geometry of the Ulbricht sphere in the experiments, the average reflectivity is $\bar{\rho} \gtrsim 90\%$. The output radiation field can be derived from the convolution of the input radiation field with the time response of the sphere of the form e^{t/τ_s} with the time constant τ_s determined by

$$\tau_s = -\frac{2}{3} \cdot \frac{\mathrm{d}_s}{c} \cdot \frac{1}{\ln \bar{\rho}} \tag{3.2}$$

where c is the speed of light and d_s is the diameter of the sphere. The estimated scale of the time constant is of the order of 4 ns. After several reflections on the inner surface walls of the Ulbricht sphere, the reflected radiation reaches the active surface optical bundle fiber which is coupled to the sphere. After the fiber, the radiation signal passes through a lens with f = 7.5cm and is focused onto the photodiode. In order to prevent the high energy plasma radiation from damaging the photodetector, and to keep the incident radiation level within the linear response of the photodetector, several suitable neutral density (ND) and infrared (OG550) filters are placed in front of the lens.

The linearity of the sphere reflectivity was checked as a function of the incidence laser fluence and found to be better than 7% for fluences up to $\approx 64\text{mJ/cm}^2$. Additional information regarding the Ulbricht sphere can be found in the PhD dissertation by M. Cerchez [57].

A photo of the setup of the absorption measurements is shown in Figure 3.6(a) where the Ulbricht sphere is situated in the target chamber. Figure 3.6(b) is the photo of the photodetector to measure the energy reflected by the target.

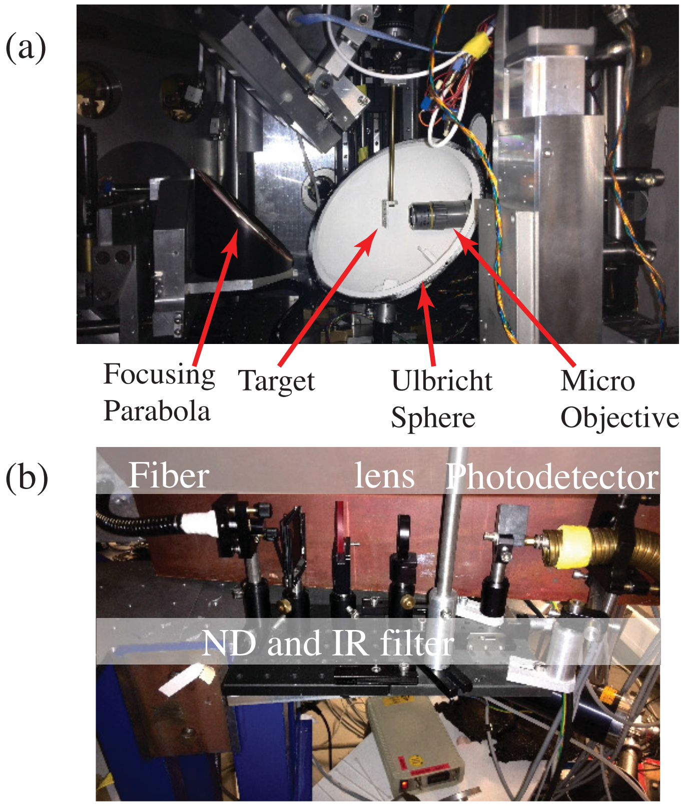

Figure 3.6: (a) Photo of the Ulbricht sphere mounted in the target chamber to measure the laser energy absorption fraction. The main components in the target chamber are indicated. (b) Photo of the set-up of the photodetector to measure the energy reflected by the target.

3.4 Experimental Setup for Electron Acceleration

We investigate the distribution and spectrum of the accelerated electrons. Depending on the target configuration and thickness, different experimental arrangements were used. Figure 3.7(a) shows the typical schematic of the electron measurement for bulk targets and (b) for the foil targets. We define ϕ to be the angle between the surface fast electron (SFE) emission direction and the target surface direction in the incidence plane. For bulk targets, such as gratings and flat mirrors, the electron spectrometer is oriented along the target surface direction at $\phi = 3°$ to measure the energy spectra of the SFEs with the aid of Fuji BAS-TR imaging plates. The gratings' grooves were orientated normal to the laser polarization direction. A sandwich stack detector consisting of four layers of imaging plates of 80mm$\times$80mm in size separated by Al filters. For thin foil targets (Figure 3.7 b), the electron spectrometer is set up at the target normal direction at the rear side.

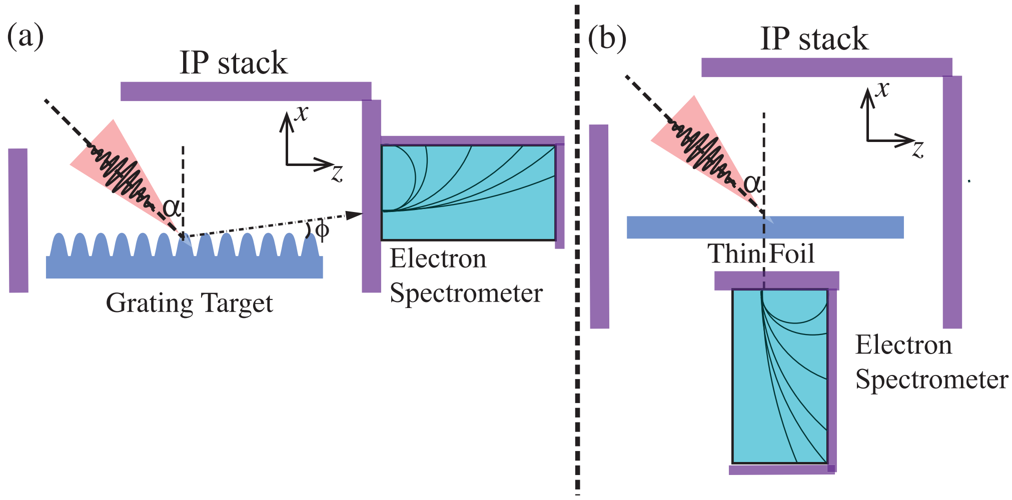

Figure 3.7: Schematic view of the experimental setup.

3.4.1 Fuji BAS-TR Imaging Plates

The "Imaging Plate" (IP) is a new film-like radiation image sensor comprised of specifically designed phosphors that can trap and store the radiation energy.

The stored energy is stable until scanned with a laser beam, which releases the energy as luminescence. By this phosphor technology, imaging plates become an indispensable detection tool for the quantitative measurements of the electrons generated by laser plasma interaction. Besides, they can also be used for detecting other particles, such as protons, ions and photons in UV, XUV and X-rays range [58, 59]. Imaging plates were actually originally developed as a reusable medical X-ray diagnostic and thereafter widely used in medicine, biology and industry applications. The properties of the imaging plates and the calibration method will be discussed in the following section in detail.

The Imaging Plate is a flexible image sensor in which bunches of very small crystals (grain size: about 5 μm) of photo-stimulable phosphor of barium fluoro-bromide containing a trace amount of bivalent europium as a luminescence center, formulated as BaFBr: Eu2+, are uniformly coated on a polyester support film. The process is known as Photostimulable Luminescence (PSL) effect. The basic principle is that the incident particles or photons excite the metastable states in the sensitive layer of the plates, which are very stable and therefore can save the signals over a long time. These plates can be irradiated, read out and processed by a commercial scanner system. Since the metastable states are reversible, the plates can be reused after reexitation. In combination with a dedicated scanner, a dynamic range of 5 orders of magnitude can be reached. The sensitive layer of type BAS TR plate used in the experiments is 50 μm thick [60]. Figure 3.8 illustrates the basic structure of a Fuji BAS−TR imaging plate and the process of exposure and scanning. Left: the IP is firstly exposed to the particles i.e. electrons, ions or photons. Right: the HeNe-scanning beam relax the excited metastable states in the sensitive layer and the PSL signals is detected by the photo-multiplier (PM).

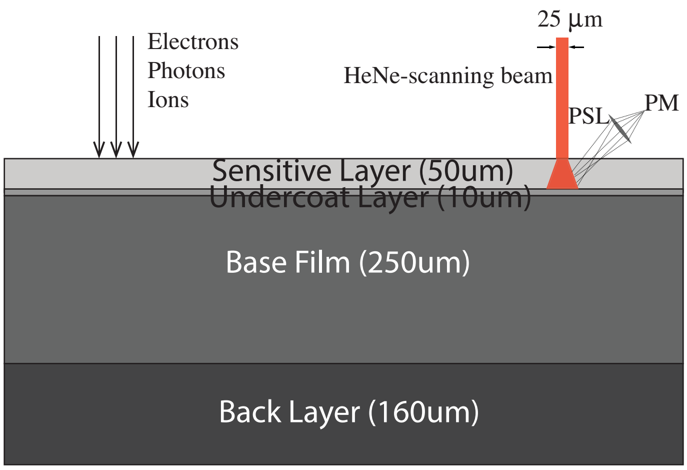

Figure 3.8: The composition of Fuji BAS−TR imaging plate and the process of exposure (left) and scanning (right).

Table 3.1: The thickness, density and material composition of the layers consist of imaging plate Fuji BAS−TR.

Layer	Thickness(μm)	Density(g/cm^3)	Material
Sensitive	50	2.85	Phosphor[1] :Urethane[2]=25:1
Back	10	1.39	Plastic
Base	250	1.39	PET[3] $(C_{10}H_8O_4)_n$
Ferrite	160	2.77	Mn_2O_3, ZnO, Fe_2O_3+Plastic

[a]Phosphor: Ba:F:Br:I=1:1:0.85:0.15
[b]Urethane: $C_3H_7NO_2$
[c]PET: Polyethyleneterephthalate
From http://www.buero-analytik-winden.de

There are several types of imaging plates, with different properties in resolution, size and thickness of the sensitive, protective and carrier material layers. The protective layer with a few microns of thickness covered by Mylar at the top of most IPs serves as mechanical protection and also protects the IPs from humidity. Some of IPs avoid such a protective layer in favour of keeping the sensitivity. Below the protective layer is a $50 - 120\mu$m thick sensitive layer where the signals can be stored, followed by a thin back layer, a base layer and a ferrite layer which is slightly magnetic to fix the IP during the scanning procedure. The characteristic properties of the layers composing of FUji BAS−TR imaging plates are listed in the Table 3.1.

As mentioned before, the dynamic range of the imaging plates is of the order of 10^5 which is greater than the intensity range in which the imaging plate scanner (in our case, CR35BIO) can read in one single scan. At higher signal intensity, it is therefore necessary to repeat the scanning process because the readout of the imaging plate might exhibit "overexposed" regions in case of strong irradiation after the first scan. It means that the signals stored in this region is too intensive to be read out by the scanner in one scan but is still in the dynamic range of the IP. Nevertheless, it is possible to repeat the readout process and reconstruct the original intensity stored in the IP. The decrease rate in the signal intensity in the IP is independent of the initial intensity, but is solely a function of the number of successive scans. Figure 3.9 shows the results of several test series for consecutive readouts using our scanner CR35BIO. The experimental data can be fitted by an exponential decay function as

$$L_n = 0.999 + 1.8279 \cdot \exp(-n/1.4027) \tag{3.3}$$

where n is the scan number, L_n is the erasing rate defined as the ratio of the signal intensity scanned after n times to the intensity scanned after the first time. The

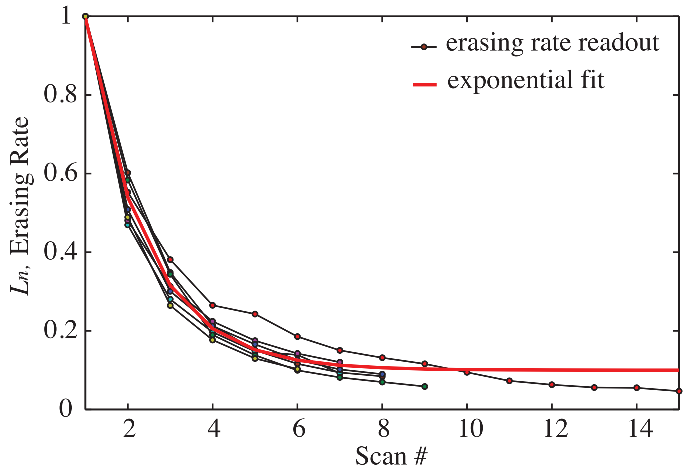

Figure 3.9: The signal intensity stored in the IP decreases with the number of repeated scans. With each scan, the signal is attenuated by a corresponding erasing rate, independent of the initial intensity value.

difference between our fitting decay function and the function from [60] mainly comes from the different imaging plate scanners. The signal recorded in an IP does also fade with time but does not change significantly after 80 minutes[61]. So we have already included time fading in the decay function and most of the IPs were scanned after this time. Each scan took around 8 min at a pixel size of 25 μm.

In the experiment, three sandwich stacks composed of several layers of aluminium filters and imaging plates were mounted around the interaction point to detect the emitted electrons within an angular range ϕ between 0° and 180° excluding the laser incoming divergence angle. Figure 3.10 shows the arrangement of the stacks in detail. The top 1.5 mm Al layer filtered out 98% of the X-rays with photon energies below 15 keV as well as the electrons energies $\varepsilon \lesssim$800 keV. The last IPs record the electrons with energies higher than 1.7 MeV. Considering the divergence of electrons in the target surface plane and the distances between each stack and the target, the IPs surfaces are chosen as 8cm$\times$8cm, sufficient for recovering the electron divergence in the target surface plane of an angle range of $\pm 40^o$.

The IPs were erased before being placed into the interaction chamber and exposed to a new shot. Due to the high signal intensity, the first front imaging plate is always “overexposed” that a single scan is not able to readout the signal on the IP. After several successive scans, the initial signal intensity (PSL) can be deduced through the above described fading characteristic equation 3.3.

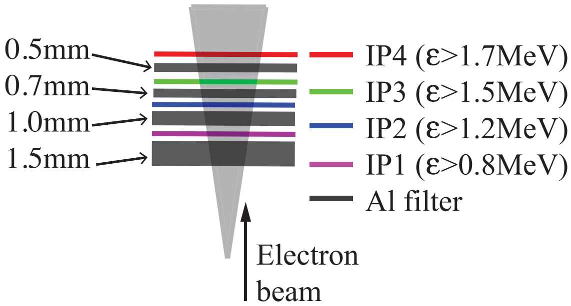

Figure 3.10: IP stack design. The IPs are separated by Aluminium filters with various thicknesses.

In 2005, with the LINAC accelerator source, Tanaka *et al.* [61] calibrated the BAS-SR IP response for electrons with three different energies (see Figure 3.11). They also gave the fading effect as a function of time after exposure. In addition, they studied the effect of an electron at oblique incidence at the IP. Afterwards, Hidding *et al.* [60] calculated the deposited energy per electron in the sensitive layer of an IP for various types of IPs using the Monte Carlo-type framework GEANT4. Figure 3.11 (from B. Hidding's PhD dissertation [62]) shows the deposited energy per electron for the four IP types: FDL-UR-V, BAS-SR, BAS-MS and BAS-TR (solid lines, left y axis) from GEANT4 calculations and the experimental calibration curve (dotted line, right y axis) from Ref. [61]. Concerning the calculated results, there is no significant difference between the BAS-MS and the BAS-SR type while considerable differences are found for the other two types of IPs. In particular, the energy deposition of the TR type is lower by about a factor of 3 than those of the other types of IPs due to the smaller thickness and lower density of the sensitive layer in BAS-TR IP.

The calibration curve presented in [61] represented by the dotted line using the right y axis in Figure 3.11 gives the PSL response of the IP to the incidence electrons with various energies. The high-energy part of the curve is the PSL response of a BAS-SR IP upon the well-defined electron bunches with the energies of 11.5, 30, and 100 MeV produced by a LINAC. The lower-energy part is based on a relative sensitivity curve obtained in Ref. [63] using a different type of imaging plate (FDL UR-V).

One can see from the Figure 3.11 that both, the PSL value per electron from the experimental data and the deposited energy per electron from simulated calculation, are approximately constant when the electron energies are more than 1 MeV. This allows to translate the deposited energy calculated from GEANT4 linearly with a constant conversion factor into an experimental PSL value or accordingly to the electron number. As shown in Figure 3.11, an electron with an

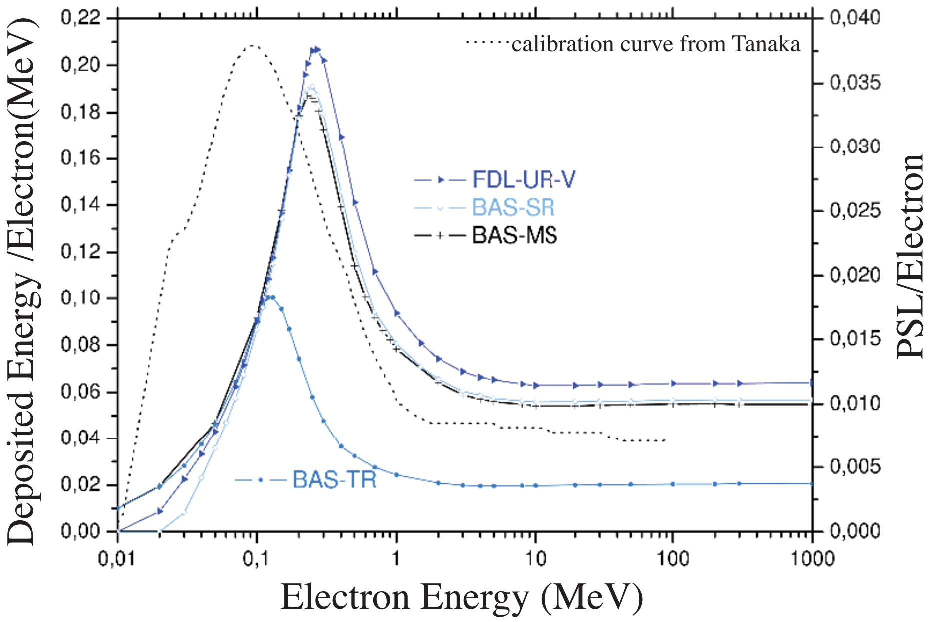

Figure 3.11: Monte Carlo calculation of the electron energy deposition in the sensitive layer of different IPs (solid lines, left y axis) and PSL calibration curve (dotted line, right y axis). The figure comes from [62].

energy higher than 1 MeV produces a measured PSL response at about 0.008, with a corresponding deposed energy of about 55 keV in a BAS-SR IP. Because the BAS-TR IP is about three times less sensitive compared to the BAS-SR IP, one can estimate that one electron with the energy higher than 1 MeV will deposit the energy of about 18 keV in the BAS-TR IP and produce the PSL response of about 0.003. It's worth noting that in Ref. [60, 61], the minimum pixel size of the scanner BAS-1800 is 50 μm and the dotted line in Figure 3.11 is obtained from setting the scanner pixel size of 200 μm. As in our data calibration, the minimum pixel size of the scanner CR35BIO is 25 μm and a factor of 64 (8×8) needs to be taken into account. Last but not least, the electron beam always has a certain divergence, so the effect of electrons obliquely incident on the IP has to be considered. It has been studied to show that there is a $1/\cos\theta$ relation between the PSL value generated by normal incident and oblique incident electrons with an angle θ [61].

The IP stack detectors were build for recording the spacial distribution of electrons emitted from the solid target irradiated by the ultrashort, ultrahigh laser pulses. The photo of the IPs stack and a detailed view inside the target chamber is presented in Figure 3.12.

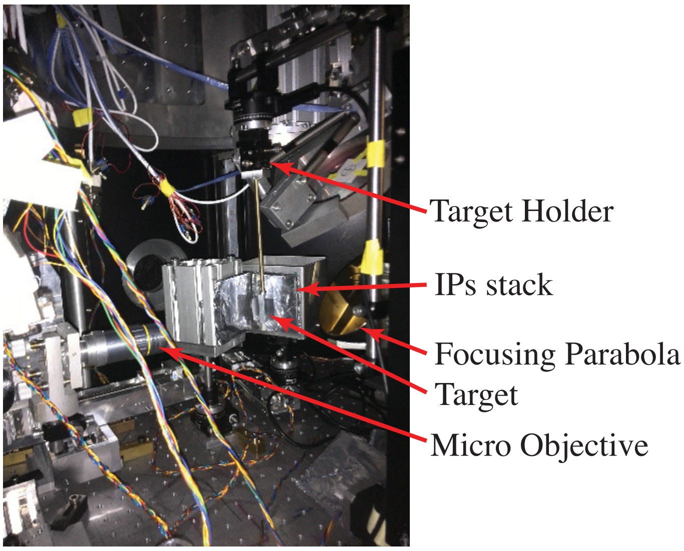

Figure 3.12: Photo of IPs stacks mounted in the target chamber. The main components are indicated in the photo including the focusing parabola, target holder and micro-objective.

3.4.2 Magnetic Electron Spectrometer

The multi-MeV electrons are detected by a magnetic spectrometer with the help of Fuji BAS-TR imaging plates. The magnetic spectrometer consists of a pair of 5 cm long permanent magnets of 0.28 T and can be used for detecting electrons with energies higher than 330 keV. The spectral resolution, determined by the slit width and the dispersion of the spectrometer, is 0.004 MeV at 1.5 MeV and 0.02 MeV at 5 MeV. The slit width used in the experiments is 0.5 mm and the distance between the interaction point and the entrance slit of the spectrometer is about 4 cm.

The typical images on the IPs recorded in the top and back sides (with respect to the electron entrance slit) of the magnetic electron spectrometer are shown in Figure 3.13. The energy of the relativistic electrons from the top side E_t and from the back side E_b can be obtained by

$$
\begin{aligned}
E_{t,b} &= E_0\Big(\sqrt{\frac{1}{1-1/(1+(m_e c/eBr_{t,b})^2)}}-1\Big),\\
r_t &= \frac{b^2+\ell^2}{2b},\\
r_b &= \frac{L^2+\ell^2}{2\ell},
\end{aligned}
\tag{3.4}
$$

where m_e is the electron rest mass, c the light speed, B the strength of the magnetic field, r_t and r_b the Larmor radius of the electron reaching the top and the back side

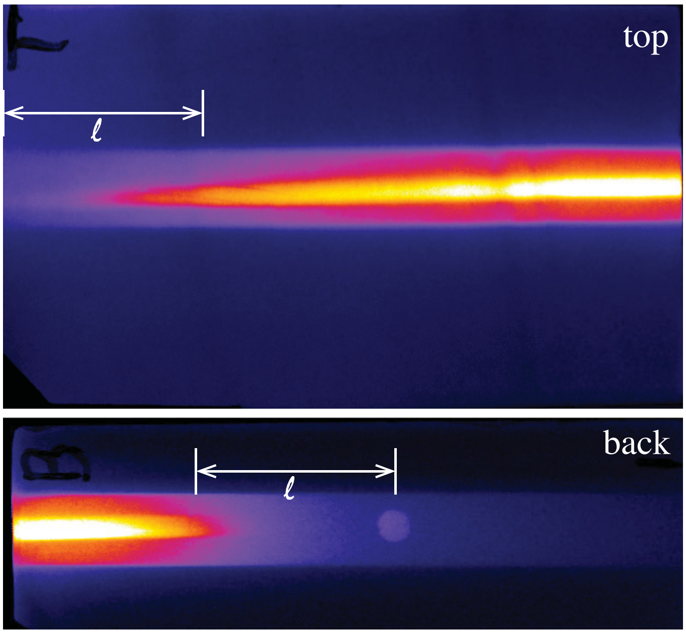

Figure 3.13: Typical images on the IPs recorded in the top and back side of the magnetic electron spectrometer.

of the spectrometer, respectively, $E_0 = m_e c^2$ the electron rest mass energy, L the length of the magnetic field, b the vertical distance between the electron entrance slit to the top of the magnetic field. The distance ℓ is marked in Figure 3.13.

The PSL recorded on the IPs corresponds to the number of electrons. After calibrating the PSL on the IPs, the electron energy spectrum can be obtained.

3.5 Targets

In experiments, three different targets, i.e. gratings, metal thin foils and carbon nanotubes (CNTs) were used. All three types of targets were employed in the experimental investigation of the energy absorption and acceleration of hot electrons.

3.5.1 Gratings

The grating targets used in the experiments are holographic reflection gratings with a sinusoidal profile coated by 1μm Au layer. Three types of gratings with different groove spacings (λ_g) sub-, near- and double-wavelengths (relative to the laser wavelength) were examined. An atomic force microscope (AFM) image of

Table 3.2: The parameters of grating targets and flat Au mirrors used in the experiments of electron acceleration and absorption.

Target	λ_g (nm)	h (nm)
G278	278	50
G833	833	60
G1667	1667	80
Flat Au mirror	–	< 10
Rough Al plate	–	1.6μm

one of the gratings is depicted in Figure 3.14. The longitudinal periodicity of the grating is given by the parameter λ_g and the peak-to-valley depth of the grooves denoted by h_g. For comparison, a gold coated flat mirror with the same thickness and the surface roughness less than 10 nm and an Aluminium plate rough target with the roughness $h = 1.6\mu$m were used. A list of the parameters of targets which were utilised in the experiments can be found in Table 3.2. The grating's grooves were orientated normal to the laser polarization direction.

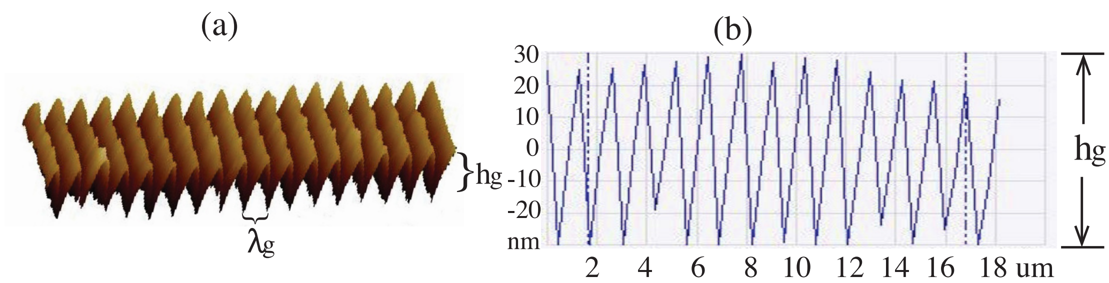

Figure 3.14: (a) 3D atomic force microscope images of a holographic grating; (b) Sectional view of target G833 (λ_g=833nm, h=60nm)

3.5.2 Thin Metallic Foils and CNTs

Different kind of metal foils and CNTs with different thicknesses were selected in the experiments depending on the experiment purposes and diagnostic methods. Table 3.3 gives the detailed materials, thicknesses and the experimental observations of the targets utilised.

Table 3.3: The thickness of thin metallic foils and CNTs employed in the experiments and the observations

Target Material	**Thickness**	**Observations**
Titanium	3 μm	IA
	5 μm	EA, IA, AM
Copper	750 nm	EA, IA, AM
Aluminium	400 nm	EA, IA, AM
	6 μm	IA
	12 μm	IA
	20 μm	IA
CNT	20 μm	IA
	100 μm	EA, IA, AM

EA: electron acceleration
IA: ion acceleration
AM: absorption measurement

Chapter 4

Experimental Studies of Electron Acceleration on Solid Targets

In this chapter, the experimental results of electron acceleration on different solid targets, i.e. gratings and thin metallic foils are reported. The fast electrons accelerated during the interaction of ultrashort laser pulses with grating targets, of sub-, near and double-wavelength (relative to the laser wavelength) groove spacings, are investigated experimentally. The electron acceleration along the target surface direction, in and out of the surface plasma waves (SPWs) resonance condition are investigated with the double-wavelength grating and compared with other gratings and flat targets. The flux of surface fast electrons is enhanced dramatically in the case of the grating targets and the optimum is near the wavelength grating at an angle of incidence of 45°. A significant enhancement of the high-energetic electron flux is also observed for the sub-wavelength grating target close to the laser specular direction at $\alpha = 53°$.

4.1 Electron Acceleration on Grating Targets

In this section, we report on the first experimental studies of the enhanced fast surface electron beams produced by grating targets (GTs) irradiated by femtosecond laser pulses with the relativistic parameter $a_0 \simeq 10$. The incidence angular dependence, electron acceleration efficiency and electron energy spectrum using GTs are studied in comparison with the flat targets (FTs). A pronounced enhancement of the number of fast electrons and higher collimation of electron beams from GTs emitted along the target surface compared with FTs are observed, while the electron energies do not alter too much. We found that the total number of surface fast electrons (SFEs) from GTs strongly depends on the angles of incidence and the preplasma conditions, whereas the spectra merely rely on the preplasma conditions. Also, the optimum angle of incidence for the laser is 45°.

Figure 4.1 shows the geometric diagram of the raw data recorded on IPs in the experimental setup. ϕ is defined as before mentioned to be the angle between the electron emission direction and the target surface direction in the incidence plane. θ denotes the angle between the electron emission direction and the target surface direction in the target surface plane. The electron number per radian in the figure of electron angular distribution in the following sections is obtained in the incidence plane by summing all the electrons emitting in the θ direction at the certain angle of ϕ.

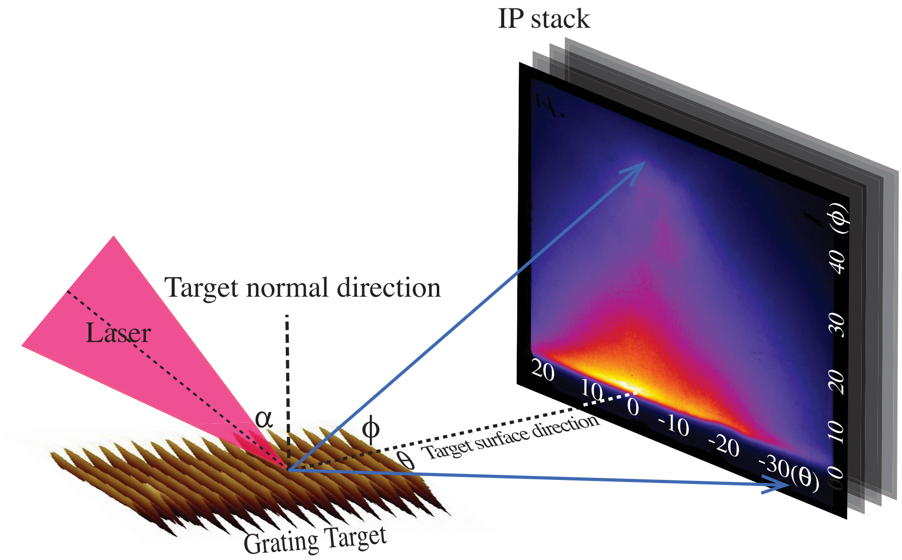

Figure 4.1: The schematics of the raw data recorded on IPs.

4.1.1 Angular Distribution

In Figure 4.2, the angular distributions of fast electrons produced in the incidence plane from the GTs with different groove spacings and the flat target irradiated by the laser pulse at the angle of incidence $\alpha = 30°$ and 45° with the electron energies $\varepsilon \gtrsim$ 1.5 MeV are presented. The number of electrons per radian is obtained by summing the electron counts over all the different polar directions in the incidence plane. Evidently, a large fraction of the emitted electrons propagates along the target surface direction ($3° \sim 5°$) for grating target G833 and G1667, while no electrons with energies higher than 1.5 MeV are found for the flat target and G278 in the direction of $\alpha = 30°$. Also, the target G278 shows a similar behaviour as for the flat target at $\alpha = 30°$ under our experimental conditions. In Figure 4.2(b), at $\alpha = 45°$, all three of grating targets produce higher electron fluxes along the target surface direction compared with the flat target. Furthermore, the SFEs angular distribution of the fast electrons measured on the grating G1667 ($\lambda_L \approx 2\lambda_g$) shows quantitatively similar behaviours in comparison to the near$-\lambda_L$ G833 case. Apparently, both the double- and near- λ_L grating targets are superior to sub$-\lambda_L$ G278 in respect of electron flux and the number of fast electrons generation. In particular, the target G833 displays the best performance with higher maximum electron flux compared with target G1667 along the surface direction at both the angles of incidence $30°$ and $45°$. An enhanced flux is generated by G833 with a factor of three compared with the flat target along the target surface direction at $\alpha = 45°$.

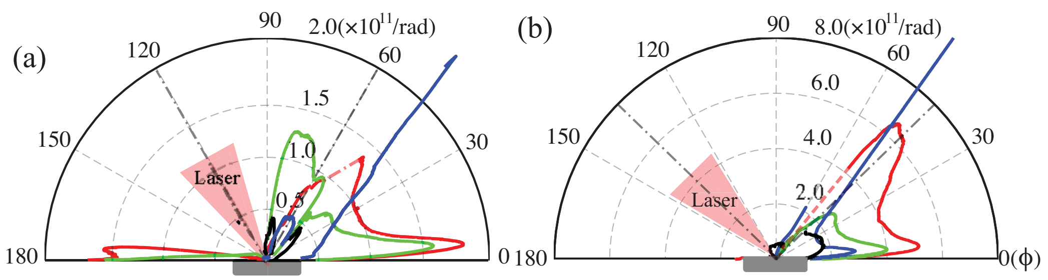

Figure 4.2: The angular distribution of electrons at $\alpha = 30°$ (a) and $45°$ (b) with electron energies $\geq$ 1.5 MeV. Here, blue: G278, red: G833, green: G1667 and black: flat target.

More electrons with higher energies are found around the laser specular direction for the grating targets when α is increased to 45°. In particular, the sub$-\lambda_L$ grating G278 exhibits a strong and high collimated electron beam emission at this direction. At the angle of incidence of 30°, the electron flux peaks at $\sim 48°$ with a small offset from the target normal direction. When the angle of incidence increases to 45°, this maximum flux occurs at $\sim 53^\circ$ which shifts to the target normal direction. The position of the flux peaks for all the three gratings are very close to each other for both angles of incidence and only shift a little when the angles of incidence increase from 30° to 45°. For the flat target, few electrons with $\varepsilon \geq 2.5$ MeV can be found close to the laser specular direction.

The target G278 displays a similar performance with the flat target at $\alpha = 30^\circ$ while shows the similar features with the grating G833 at $\alpha = 45^\circ$. This can be explained on the one hand, that the target surface modulations of 278 nm are too small and too close with each other to display the collective interaction; on the other hand, such a small amplitude is much easier smeared by the preplasma, leading to behaviors like on a flat target. Similar results were also reported in Ref.[18, 68]. However, the target G278 shows similar characteristics with the grating G833 at $\alpha = 45^\circ$. Thus one can estimate that due to our high contrast, the scalelength of the preplasma is about a few percent of the laser wavelength. Under such steep density gradient conditions and intense laser fields, vacuum heating and $\boldsymbol{j} \times \mathbf{B}$ heating are the major absorption mechanisms in the electron acceleration. At small angles or even at normal incidence, electrons can be dragged out from a structured surface into the vacuum by $\boldsymbol{j} \times \mathbf{B}$ heating and then reenter into the neighbour cells of the grating to deliver the energy. So grating targets can absorb the laser energy more efficiently than the flat target at small angles of incidence. For large angles of incidence, the vacuum heating are dominant by driving the electron motion with the component of $\mathbf{E}$ perpendicular to the target surface. Thus, the grating targets behave similar to the flat target. At this point of view, the optimum angle of incidence of grating targets does not occur at very large angles.

4.1.2 Electron Beam Charge

Figure 4.3 shows the charge of electrons ($\phi = [0^\circ, 180^\circ]$) and the SFEs ($\phi = [0^\circ, 10^\circ]$) generated by different grating and flat targets at different angles of incidence. We found that the efficiency of electron acceleration is higher at $\alpha = 45^\circ$ than at 30° for both grating targets and the flat target. The total number of electrons with energies higher than 1.5 MeV generated by G833 at the angle of incidence of 45° is about 73 nC and 17% of the electrons are emitted along the target surface direction within the angle of $\phi = [0^\circ, 10^\circ]$ which is about 2.6 times larger

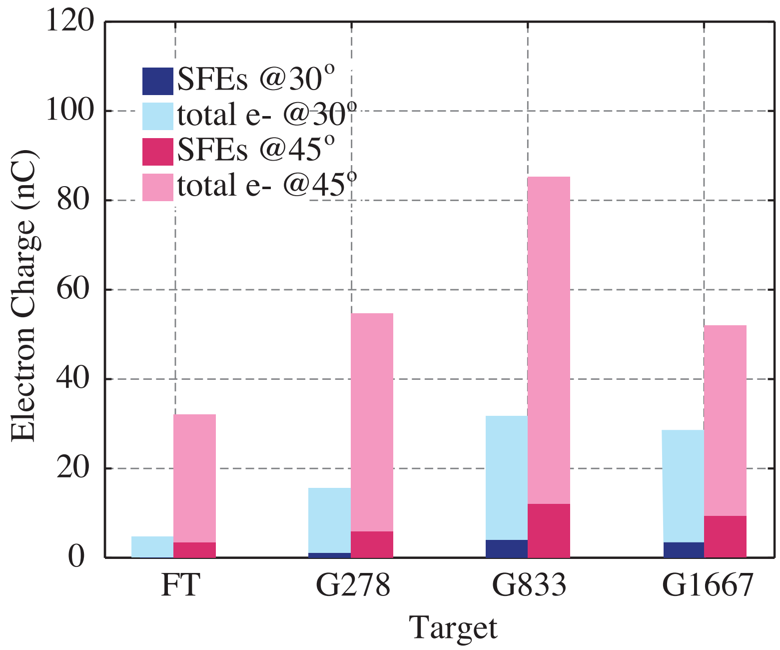

Figure 4.3: The total charge of electrons ($\phi = [0°, 180°]$) and the SFEs ($\phi = [0°, 10°]$) with energies higher than 1.5 MeV generated by different targets at $\alpha = 30°$ and 45°

than for the same target at $\alpha = 30°$. The total charge of fast electrons generated by G833 at $\alpha = 45°$ is 2.5 times and the charge of SFEs 3.5 times larger than that from the FT.

4.1.3 Surface Fast Electrons

We proceed to study more closely the generation and acceleration of the SFEs. One of the acceleration mechanisms of electrons propagating close to the direction along the target surface is associated with the acceleration from surface waves (SPWs) [25, 30]. The condition for resonant excitation of a SPW on a grating by an incident EM wave with the same frequency (neglecting thermal, collision and relativistic effects) is $\lambda_L/\lambda_g = [(1-\eta)/(2-\eta)]^{1/2} - \sin\theta_i$ (Eq 2.99), where λ_g being the grating period and $\eta = (\omega_p/\omega)^2 = n_e/n_c$, with ω_p the plasma frequency and n_c the critical density. Within this linear model, only the target G1667 ($\lambda_L/\lambda_g \approx 1/2$) at $\alpha = 30°$ fulfills the SPW resonant condition for $\eta \gg 1$, while the resonant condition is not satisfied for the target G1667 at $\alpha = 45°$ and G833 at $\alpha = 30°$ and 45°.

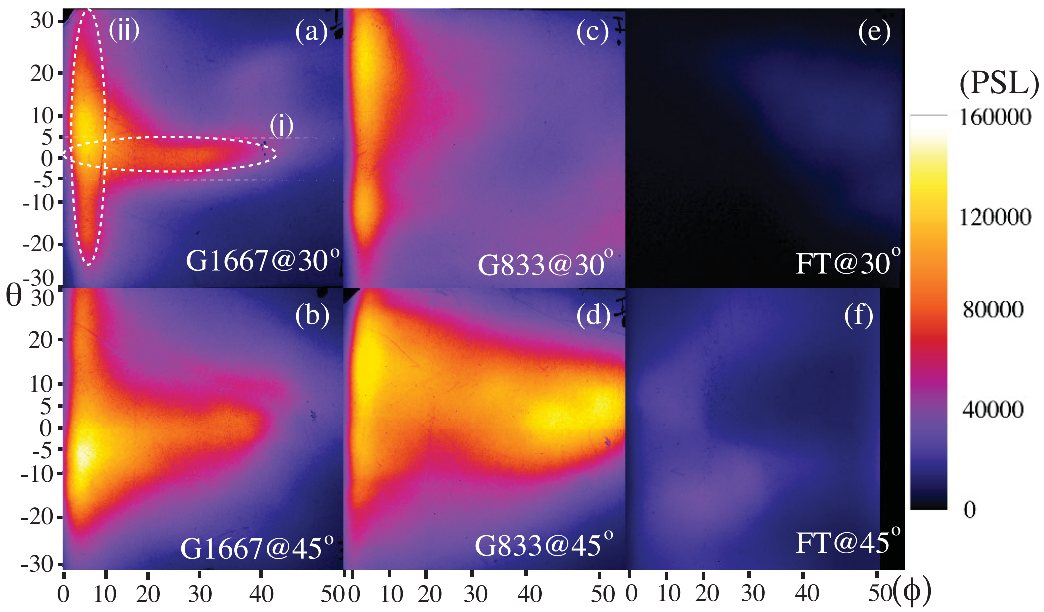

Figure 4.4: Electron spatial distributions of G1667, G833 and the FT at $\alpha = 30°$ and $45°$. θ and ϕ are the polar and azimuthal angle, respectively. The electron energies$\geq$ 1.5 MeV.

Figure 4.4 shows the spatial distribution of the electrons collected on the 3rd IP of the stack detector corresponding to $\varepsilon \geq 1.5$ MeV for G1667, G833 and the flat target at $\alpha = 30°$ and 45°. Prominently, in Figure 4.4(a), two preferential distribution directions can be recognized, (i) in the incidence plane with a spread up to $\phi = 40°$ and (ii) in the surface plane with a spread up to $\theta \doteq \pm 30°$. The spacial distribution of the surface electrons obtained in the incidence plane: (i) is similar to the previous results [30] and their origins were attributed to the SPWs acceleration in linear regime. The distribution in the surface plane (ii) has not been found in prior work [30] while it shows up in all cases as shown in Figure 4.4 (b-d). The experimental parameters in the case of Figure 4.4 (b-d) do not meet the SPW resonant condition. Interesting features are obtained in the Figure 4.4 (b). The linear model predicts a resonant condition at $\alpha = 30°$ for the grating G1667. We measured an enhanced flux of SFE by a factor 3 at $\alpha = 45°$ compared with $30°$. This deviation from the previous experiment [30] and theoretical works [25] indicates that in our interaction conditions additional effects influence the excitation of SPWs at such a high laser intensity. However, we can say that there are still electrons coming from SPWs excitation acceleration mechanism for G1667 at $\alpha = 45°$ due to our short focal parabola (f#=2).

4.1.4 Angular Dependence

In the region (ii), the SFEs will distribute to the larger angle ϕ when the angle of incidence is increased to $45°$ as shown in Figure 4.4(b, d) for the grating targets.

Figure 4.4(e, f) displays the spacial distribution of SFEs generated by the flat target. It is clear that there are much fewer electrons of energies ≥ 1.5 MeV generated by the flat target compared with the grating targets.

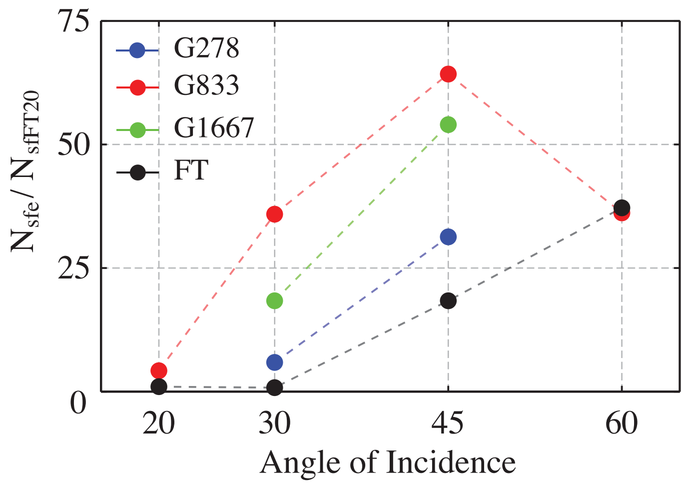

Figure 4.5: The number of surface fast electrons ($\phi \in [0°, 10°]$) at different angles of incidence. The data are normalized by the number of SFEs from the flat target at $\alpha = 20°$ and the electron energies ≥1.5 MeV.

We further study the dependence of electron acceleration on the gratings at different angles. The flat target indicated by the black dotted line in Figure 4.5 shows a typical monotonous increase of the number of SFEs with the angle of incidence due to the vacuum heating effect. However, the optimum angle of incidence for SFE acceleration by grating targets appears at 45° instead of 60° inconsistent with the simple vacuum heating scenario, which is also confirmed by our laser absorption measurements. Clearly, the linear SPWs resonant acceleration is not solely responsible for the SFEs acceleration in the laser-grating interaction. In Figure 4.5, the number of SFEs at $\alpha = 45°$ is larger than at 30° for G1667, and the electron production of G833 shows a better performance than G1667. This can be understood as follows: the peak-to-valley depths of our grating targets are very sensitive to the scalelength of preplasma due to the prior heating since tens of nanometers of preplasma will smoothen the grating surface structures. It means that the preplasma fills valleys of gratings leading to a decrease of the maximal plasma density (also η, see in Eq. 2.99) and therefore to an increase of the optimal angle of laser pulse incidence [69].

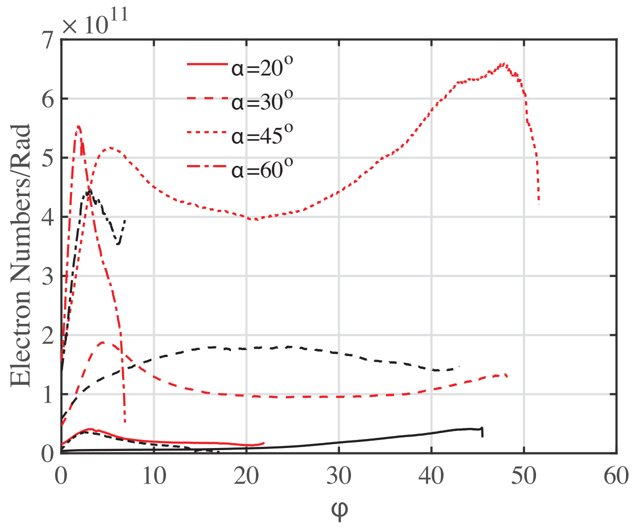

Figure 4.6: The angular distributions of surface fast electrons ($\varepsilon \geq 1.5$ MeV) generated by the flat target (black) and grating G833 (red) at different angles of incidence. ϕ is the angle from the target surface direction.

The angular distributions of the surface fast electrons generated by the flat target and grating G833 are compared at different angles of incidence as $20°, 30°, 45°$ and $60°$, and shown in Figure 4.6. The efficiency of surface fast electron acceleration from G833 is higher than the flat target at the same angle of incidence. From the Figure 4.6, the highest efficiency of SFE acceleration from G833 in the angular range $\phi \in [0°, 10°]$ occurs at the angle of incidence $\alpha = 45°$. However, the highest flux is found when α is $60°$ for grating G833 at $\phi = 2°$, closer to the target surface direction compared with $\phi = 6°$ at $\alpha = 45°$. To seek an electron beam with high collimation, high flux, few MeV generated by laser$-$solid interaction as an application, the grating targets at larger angle of incidence can be a good option.

4.1.5 Electron Distribution with Low Laser Contrast

It is well known that a preplasma plays an important role in the laser-solid target interaction [70–72]. In our experiments, we found that both fast electrons number and energies depend strongly on the preplasma conditions. Figure 4.7 shows the angular distributions of fast electrons generated by the GTs and the FT at $\alpha = 45°$ without the plasma mirror. In this case, the angular distributions of fast electrons are quite similar for the GTs and the FT. The fast electrons distribute almost homogeneously within the angle range of $\phi \in [0°, 120°]$. The angular distributions of fast electrons at $\alpha = 30°$ are quite similar to those at $\alpha = 45°$. This observation indicates that with low laser contrast, the scalelength (L_n) of the preplasma is larger than the peak-to-valley depth (h_g) of the grating, which hints the surface structure of the grating has been smeared out by the prepulse before interacting with the main pulse. With the PM, $L_n < h_g$ and the target surface structures are preserved by virtue of the ultrahigh laser contrast.

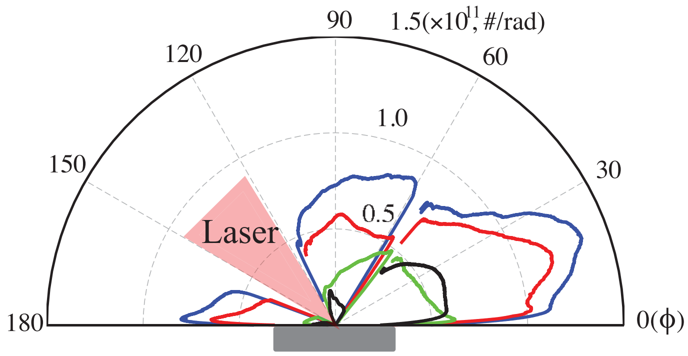

Figure 4.7: Angular distributions of fast electrons in case of low laser contrast. Electron energies≥800 keV. The colour denotations are the same as in Figure 4.2.

4.1.6 Energy Spectra of Electrons

The electron energy spectrum is the number of electrons or intensity of the electron beam as a function of electron energy. Both, the number and the energy of electrons emitted along the target surface direction, can be obtained by the magnetic spectrometer placed at $\phi = 3°$ and using IPs as the detector. In this section, the electron energy spectra and their incidence angular dependence of different targets (FT and GTs) will be compared and analysed in detail.

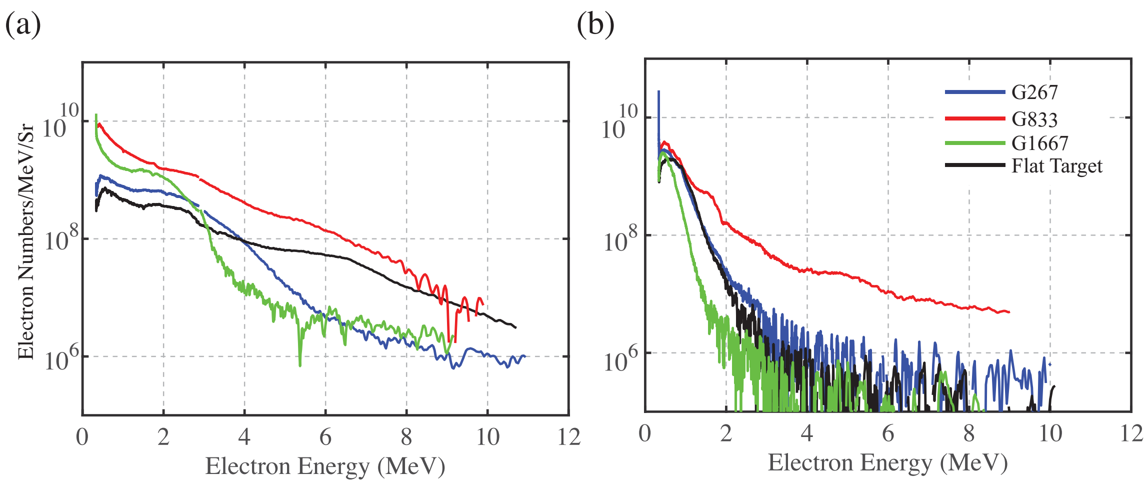

Figure 4.8: The energy spectra of fast electrons at $\phi = 3°$ from the target tangent direction at $\alpha = 45°$ (a) with PM and (b) without PM.

Due to the different target configuration, the solid acceptance angle of the magnetic spectrometer in each target case is different. For comparison, the electron energy spectra given in this dissertation are the number of electrons per solid angle as a function of electron energy. Figure 4.8 (a) shows the fast electron energy spectra of the flat and grating targets measured at $\alpha = 45°$ when the laser has the best contrast. Under such experimental conditions, there is no obvious difference between the spectra of the flat target and the gratings. After fitting the spectra with a decaying exponential function, the effective temperature of electrons are obtained in the range between 1.7 and 2.4 MeV. Taking into account the number of generated electrons discussed in Section 4.1.2, we can see that the grating targets emit much more fast electrons along the surface direction compared with the flat target while leave the electron energies almost unchanged under the conditions that the laser contrast is high and intensities $I_L > 10^{20}\mathrm{W/cm^2}$. With these data, we can calculate that the total energy transferred to the surface fast electrons with energies $\varepsilon \geq 1.5$MeV generated by G833 at $\alpha = 45°$ is approximately 0.025 J which is about 1.7% of the laser energy incident on the target.

By integrating the electron energy distribution in Figure 4.8(a), the numbers of electrons with energies $\varepsilon \gtrsim 1.5$MeV generated by all the three grating targets are larger than on the flat target, which is coincide with the results obtained from the electron angular distribution in Section 4.1.1. Figure 4.8(b) shows the fast electron energy spectra of the flat and grating targets measured at $\alpha = 45°$ without the plasma mirror. The effective temperature of electrons after fitting are within the range of 330 $-$ 480 keV which are much lower than those measured with the interaction condition with the plasma mirror. The numbers of electrons with energies $\varepsilon \gtrsim 800$ keV are similar for all targets, which is also in agreement with the results obtained in Section 4.1.5. Therefore, the number of fast electrons derived from the electron energy spectrum can be a reference of the efficiency of the electron acceleration.

Figure 4.9 gives the comparison of the electron energy spectra of FT (a, c) and G833 (b, d) at different angles of incidence with/without PM. The electron energy spectra of G833 exhibit the same dependence on the angles of incidence with the flat target when the plasma mirror was used. It is noteworthy that there is an obvious enhancement of electrons generation with energies $1 - 3$MeV from the grating target G833 at the angle of incidence $\alpha = 60°$.

A candidate for high-energy-gain of inertial confinement fusion (ICF) is fast

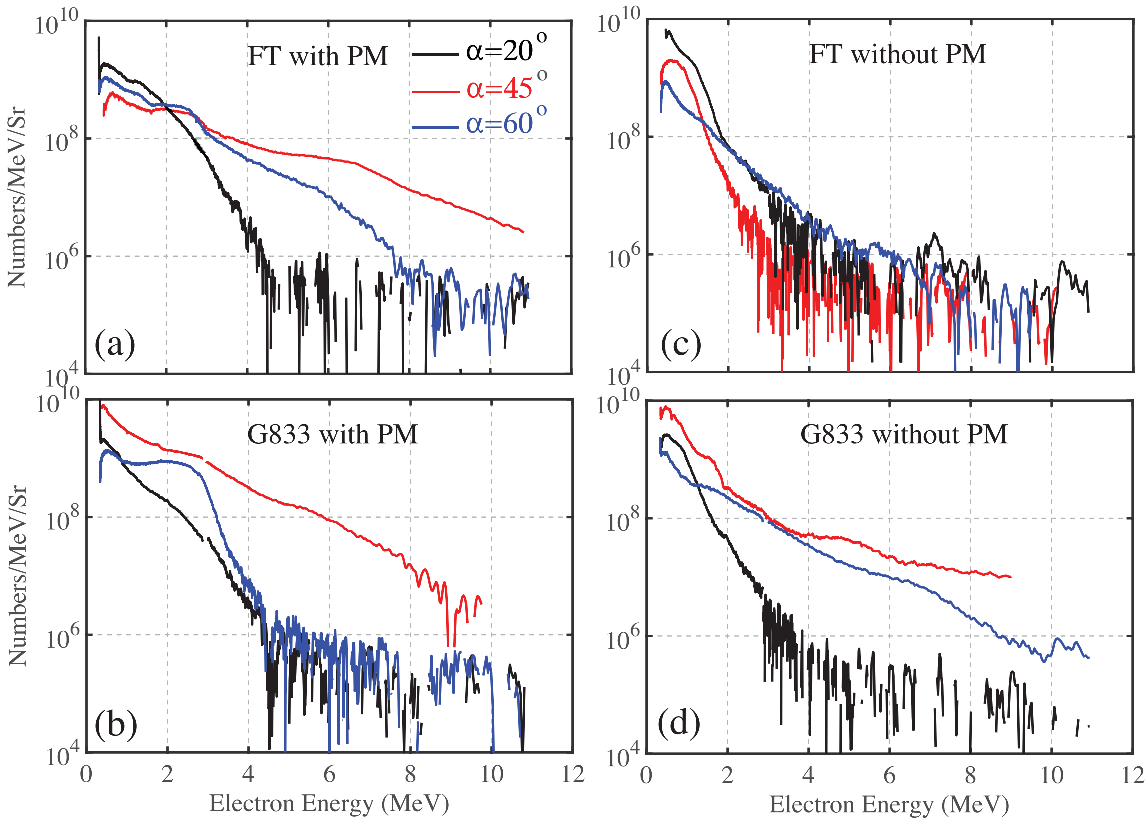

Figure 4.9: The energy spectra of fast electrons collected with the detector at $\phi = 3°$ from the target tangent direction at $\alpha = 45°$ for FT and G833, respectively. (a, b) with PM and (c, d) without PM

ignition (FI). By this scheme, the fuel can be compressed isochorically instead of a central hotspot, thereby reducing the requirements of fuel density, and leading to higher gain. The short-pulse ultraintense laser (petawatt) interacts with the solid target, creates an intense, MeV electron beam which deposits its energy into the compressed core to achieve the electron FI. In Ref. [73], an idealized electron FI scenario was simulated in 2D showing that 25kJ of electron beam energy consisting of ~ 2MeV Maxwellian-distributed electrons can heat a core of radius $\sim 40\mu$m and peak density of ~ 500g/cm^3 to ignition. The number of generated electrons of $1-3$ MeV is therefore critical to fast ignition. The grating targets can generate a larger flux ($\sim 5.5 \times 10^{11}$/Rad) and more collimated ($\sim 5°$ for FWHM) fast electrons with energies $\varepsilon = 1 \sim 3$ MeV (see Figure 4.8(a) and Figure 4.9 in the case of G833 with high laser contrast), which deserve further study.

In summary, we have provided experimental evidence of surface accelerated fast electrons enhanced by using grating targets at laser intensities higher than $10^{20}\mathrm{W/cm^2}$, which can be applied as an intense ultrashort multi-MeV electron source. A large fraction of fast electrons are generated along the grating surface while electrons with higher energies concentrate close to the laser specular direction. Our results also suggest that we are able to increase the number of fast electrons instead of their energies by using grating targets compared to the flat targets. The grating groove spacing near to the laser wavelength shows higher efficiency in surface fast electron acceleration in contrast to the double-wavelength gratings which meets the SPWs excitation conditions under resonant angle due to the nonlinear effects in the presence of the preformed plasma (see Section 2.4.3). To obtain higher collimated and larger flux and a few MeV electron beam, the optimal experimental conditions are a high contrast ($\sim 10^{-12}$) ultraintense laser pulse ($I_L > 10^{20}\mathrm{W/cm^2}$) interacting with the wavelength-scale grating target at large angle of incidence ($\alpha = 60°$).

4.2 Electron Acceleration of Thin Metallic Foils

Understanding the transport of laser-driven fast electrons through thin foils is particularly interesting in the context of many applications as acceleration of ions from laser-irradiated foils [50, 51, 74] and the fast ignition scheme of the inertial confinement fusion [75]. For example, in the target normal sheath acceleration (TNSA) process, proton acceleration is driven by the fast electron population, while the shock acceleration originates from the laser ponderomotive potential imposed on the front target surface.

In this section the experimental results of electron acceleration by three different thin metallic foils of different thicknesses, i.e. Titanium (5 μm), Copper (750 nm) and Aluminium (400 nm) are presented. The electron angular distribution in the front and rear side, the energy spectra of electrons emitted in the target normal direction in the rear side were measured at the angles of incidence of $0°$ and $45°$ with high and low laser contrasts.

4.2.1 Flat Target Ti (5 μm)

Normal Incidence

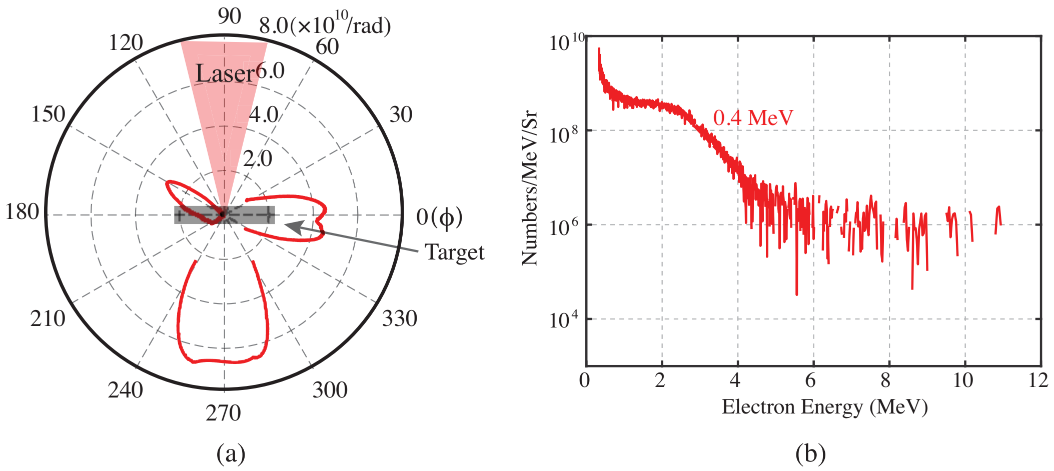

Figure 4.10: (a) Angular distributions of fast electrons generated by the Ti target at the laser normal incidence ($\alpha = 0°$). Electron energies $\varepsilon \geq$1.5 MeV. (b) Energy spectra of electrons accelerated at the rear target normal direction ($\phi = 270°$).

The spacial distribution of electrons generated by the Titanium foil target (with a thickness of 5 μm) is recorded by IP stacks with the same method as on the grating targets described in Section 4.1. The experimental set-up is shown in Figure 3.7(b). Figure 4.10(a) shows the angular distributions of fast electrons ($\varepsilon \gtrsim$ 1.5 MeV) accelerated at the incidence plane from the Ti target irradiated by the laser pulse with a high laser contrast at the angle of incidence of $\alpha = 0°$. The number of electrons per radian is obtained with the same method as for the grating targets. The laser is incident at $\phi = 90°$. A large fraction of the electrons are in the laser axis direction in the target rear side ($\phi = 270°$), i.e. target normal direction. After the absolute calibration of the imaging plates, the number of electrons emitted in the interval of $\phi \in$[240°, 330°] is $\sim 6.3 \times 10^{10}$ and amounts to a charge of 10 nC. The total number of electrons (including the surface fast electrons, $\phi \in$[0°, 360°]) is 1.2×10^{11}.

A considerable fraction (∼47.5%) of electrons accelerated on the Ti target are emitted along the target surface direction. The divergence angle of electrons with energies $\geq$ 1.5 MeV is 42° at full width at half maximum (FWHM). An obvious target shadow can be found from the angular distribution in Figure. 4.10(a). The distributions of the surface fast electrons are almost symmetric about the target surface plane at ϕ=0°.

The FWHM divergence angle of the electrons with energies higher than 1.5 MeV at the target normal direction is 51°. We follow the derivation in [32] and consider the situation of the foil target with the thickness of a few μm in which the complicated interaction can be neglected. A reasonable assumption is that the electrons are generated in the laser focal spot region and are purely collisionally transported to the rear side of the target. The electron beam divergence is mainly due to the multiple Coulomb small-angle scattering. The broadening of the distribution $f(\theta)$ was given analytically by Molière's theory in Bethe's theory [112], in the lowest order, following a Gaussian distribution:

$$f(\theta) = \frac{2\mathrm{e}^{-\vartheta^2}}{\chi_c^2 B}\sqrt{\theta/\sin\theta} \tag{4.1}$$

where the angle ϑ can be related to θ by $\vartheta = \theta B^{1/2}/\chi_c$. B is determined by the transcendental equation $B - \ln B = \ln(\chi_c^2/\chi_a^2)$. χ_a is the screening angle and given by

$$\chi_a^2 = 1.167(1.13 + 3.76\alpha^2)\lambda^2/a^2 \tag{4.2}$$

where $\lambda = \hbar/p$ is the de Broglie wavelength of the electron and $a = 0.085 a_B Z^{1/3}$, with the Bohr radius a_B.

$$\alpha = \frac{Ze^2}{4\pi\epsilon_0\hbar\beta c} \tag{4.3}$$

where Z is the nuclear charge, e the electron charge and $\beta = v/c$. ϵ_0, $\hbar$ and c denote the usual constants. The variable χ_c is given by

$$\chi_c^2 = \frac{e^4}{4\pi\epsilon_0 c^2}\frac{Z(Z+1)N_A\rho d}{A\beta^2 p^2} \tag{4.4}$$

where p is the electron momentum, N_A the Avogadro's number, ρ the material density, and A is the mass number of the target material. χ_c is related to the target thickness d and the material property $Z(Z+1)\rho/A$. Since the width of $f(\theta)$ is determined by χ_c, the angular broadening of the electron distribution propagating through the target is related to the target thickness and its material. The analytical formula (4.1) allows us to estimate the divergence of the laser-accelerated electron beam during the transport through the cold solid target. For a laser intensity $I_L = 2 \times 10^{20}\mathrm{W/cm}^2$ and the electron temperature obtained from the electron energy spectrum (Figure 4.10 b), the full-cone angle of the electron distribution calculated from formula (4.1) is around $52°$ for FWHM for the Titanium target with a thickness of 5 μm. Our experimental value is in quite good agreement with the analytical results.

When the laser pulse is incident normally to the target, electrons are dominantly heated by the $\boldsymbol{j} \times \mathrm{B}$ mechanism and pushed inwards by the laser ponderomotive force. A charge separation is induced at the target front surface resulting in the electrostatic field which accelerates the target surface forward, known as "hole-boring". The electron bunches produced by the laser pulse in the target front surface transport through the target bulk and exit the target rear surface, creating a strong electrostatic field which drives the surface proton acceleration. For foil targets with mediate thickness (a few μm at a laser intensity $\sim 10^{20}\mathrm{W/cm^2}$), the characteristic transverse size of the shock wave at the front surface is similar to the laser spot size, while the transverse size in the target rear surface is much larger than that. 2D PIC simulations [77] have shown that the electrons accelerated into the target with a nonzero transverse velocity drift rapidly out of the focal volume. These electrons are trapped in the electrostatic sheath when they reach the rear side of the target and are deflected back into the target, which has been experimentally confirmed [14, 78, 79]. As soon as the electrons penetrate the cold solid region, they will be scattered inevitably in small angles (binary collisions) by the background material. Such collisions will swell eventually the divergence of the electron beam, as well as slow down the electrons.

Figure 4.10 (b) shows the energy spectra of electrons from metallic thin foils. After fitted by a Boltzmann distribution with an exponential decay function, the electron temperature for the Ti targets is 0.4 MeV.

Oblique Incidence

At oblique incidence, it is possible to investigate the effect of the preplasma conditions on electron acceleration by removing the plasma mirror. In Section 4.1.1 and 4.1.5, the angular distributions and energy spectra of grating targets and the flat target are different due to the different laser contrasts. In this paragraph, the characteristics of the generated electrons from the Ti foil target at $\alpha = 45°$ are investigated and compared with the different laser contrasts.

The experimental results of the angular distributions of electrons accelerated by the ultrashort relativistic laser pulse at oblique incidence ($\alpha = 45°$) with a high and a low laser contrast for the Ti foil target is shown in Figure 4.11(a). The number of electrons per radian is obtained in the same way as for the grating targets. Evidently, a large fraction of the emitted electrons are along the target surface direction in this case while much fewer electrons with energies higher than 1.5 MeV are found in the target normal direction. After the calibration, the total number of electrons generated by the Ti target irradiated by the laser pulse with a high contrast (Figure 4.11 in red) is 3.0×10^{11}. Less than 5% of the electrons are coming from the rear target normal direction. Moreover, the total number of accelerated electrons is larger at $\alpha = 45°$ than that at the laser normal incidence. This may be owing to the fact that the tangent component of laser fields has more efficiency in accelerating electrons, similar to the case of bulk targets (see Section 4.1).

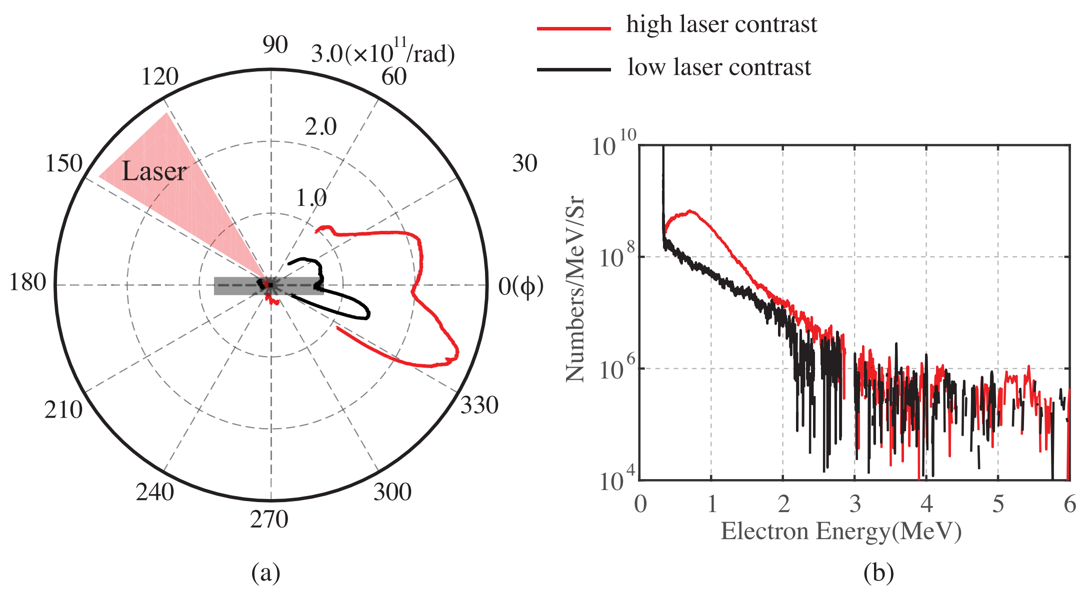

Figure 4.11: (a) Angular distributions of fast electrons generated by the Ti foil target at a laser incidence of $\alpha = 45°$. Electron energies $\varepsilon \geq$1.5 MeV. (b) Energy spectra of electrons accelerated at the rear target normal direction ($\phi = 270°$).

We notice that for the Ti target, there are more electrons emitted from the target rear side than from the target front side for both cases, for high and low laser contrast. The angular distribution of fast electrons is quite similar except the value of the fast electron flux. For a high laser contrast, the peak of the electron flux occurs at $\phi = 17°$ in the front side and $\phi = 339°$ in the rear side of the target. With the low laser contrast, the maximum flux of electrons $F_e = 1.4 \times 10^{11}$/rad occurs at $\phi = 344°$ with the FWHM divergence angle of $19°$. The total number of accelerated electrons is 1.12×10^{11}, less than 1% of which were emitted in the target normal direction.

The corresponding spectra of electrons are shown in Figure 4.11(b) for the case of laser oblique incidence with a high and a low contrast. The energy distribution of electrons accelerated with a high laser contrast is not a typical Maxwellian distribution. For the case of a low laser contrast, the effective temperatures of hot electrons is $T_e \approx 0.3$ MeV. Through the comparison of the electron angular distribution and the energy spectra, it is obvious that for a flat Ti foil target with a mediate thickness of a few μm, by improving the laser contrast the efficiency of electron acceleration will be enhanced.

Dependence of the SFE Acceleration

The acceleration of MeV electrons by ultraintense laser-solid interaction plays a crucial role in fast ignition and related high energy density science. To understand the dynamics of fast electrons, several aspects of the transport in the target, such as target materials [80], the recirculation of the hot electrons [81–83] and the transverse transport [84, 85, 87] need to be taken into account.

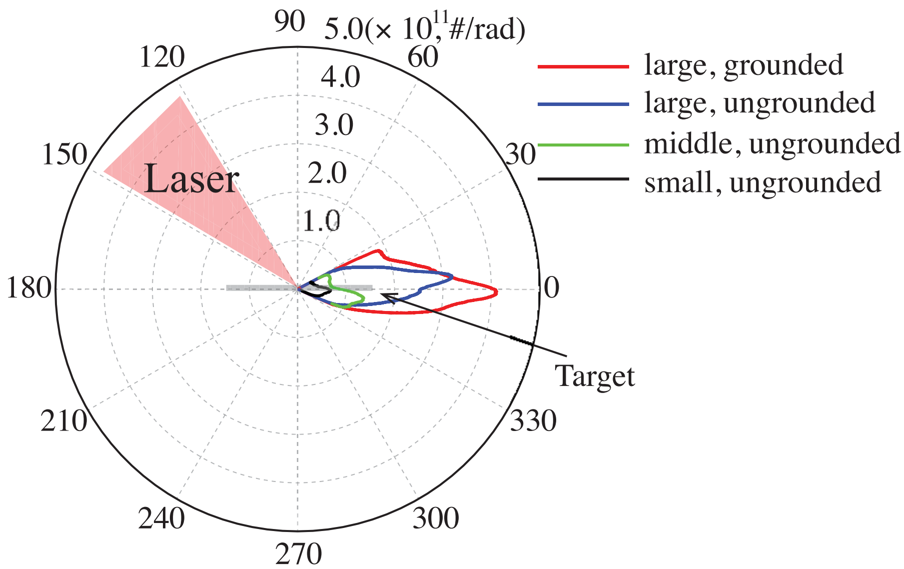

Figure 4.12: Angular distributions of fast electrons generated by thin metallic foils at oblique incidence of $\alpha = 45°$ with different target dimensions and ground conditions. Electron energies $\varepsilon \geq$1.5 MeV.

To understand the dependence of fast electrons transport on the circuit and the dimensions of the target and the cause of the appearance of target shadow, three different dimensions (large: 4.2 mm$\times$4.2 mm, middle: 1.4 mm$\times$1.4 mm and small: 0.6 mm$\times$0.6 mm) of the Ti target (5μm) with different holders (metallic and glass) were irradiated by the laser pulse at $\alpha = 45°$ in our experiments. The results shown in Figure 4.12 indicate that the shadow appearance depends on the target dimensions as well as whether the targets are grounded. The shadow will vanish whenever the target size is sufficiently small or the target is grounded.

This can be understood as follows: the average path length travelled by an electron as it slows down to stop in the material can be calculated by the continuous-slowing-down approximation (CSDA) method [86]. This length is also called CSDA range. If the target size is smaller than the CSDA range, the electrons will escape from the target edge and reach the detector. The CSDA range is a parameter of the material for certain electron energy. The lower CSDA range of the Aluminium results in the disappearance of the target shadow. On the other hand, the electrons escape from the target leading to the violation of charge neutrality and a drag field which prevents the electron from reaching to the detector results. If the target is grounded, the neutrality persists and the metallic target is an equipotential, which diminish the target resistance. This also can explain why the SFE electron acceleration efficiency by a grounded target is higher than that by an ungrounded.

It is worth noting that more SFEs emerge when the target dimension is increased as shown in Figure 4.12. It maybe connected with the quasistatic magnetic field generated self-consistently along the target surface. 2D PIC simulations indicated [43] that the peak of the quasistatic surface magnetic field moves forward along the target surface even after the pulse has been fully reflected. The field will move up to the end of the target surface and then appears at the rear surface of the target. The movement of the magnetic field increases the source size of the target, leading more electrons from the outer edge of the focus to be accelerated. Therefore the target with larger dimensions has a higher efficiency of the surface fast electron acceleration.

4.2.2 Rough Target Cu (750 nm)

Normal Incidence

In the case of a Copper foil target (with the thickness of 750 nm) is irradiated

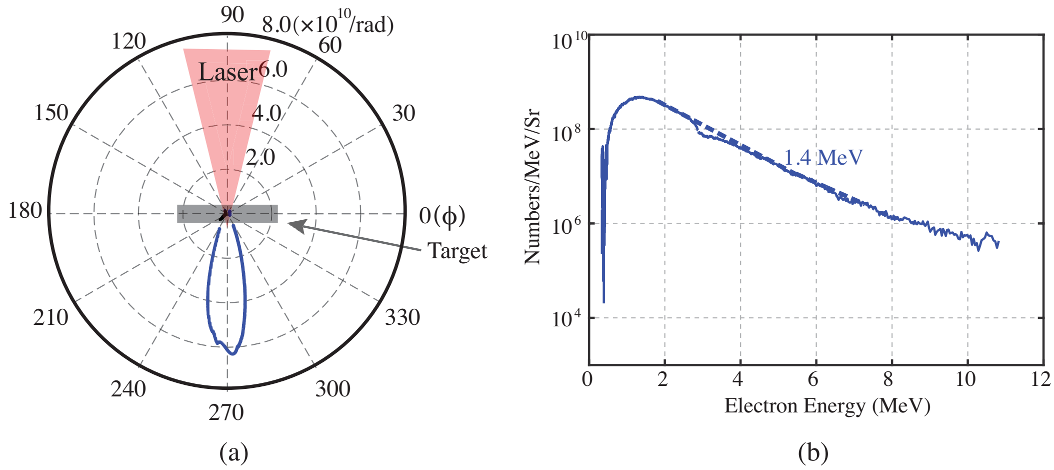

Figure 4.13: (a) Angular distributions of fast electrons generated by the Cu target at the laser normal incidence ($\alpha = 0°$). Electron energies $\varepsilon \geq$1.5 MeV. (b) Energy spectra of electrons accelerated at the rear target normal direction ($\phi = 270°$).

by the laser pulse with a high laser contrast at an angle of incidence of $\alpha = 0°$, the spacial distribution of fast electrons with energies higher than 1.5 MeV and the electron energy spectrum are shown in Figure 4.13. The total number of electrons with energies higher than 1.5 MeV is 3.6×10^{10}. Only 8% of them are emitted from the surface direction, others are all in the interval of $\phi \in$[255°,285°]. The electron beams in the target normal direction at the rear side is quite collimated.

Figure 4.14 shows typical spatial distributions of the electrons collected on the four imaging plate layers of the stack detector in the normal direction of the Cu target. The IP stack is 36 mm away from the interaction point and the size of the imaging plates is 40 mm×50 mm. The images indicate that the electrons with higher energies have a smaller divergence. In Figure 4.14, the divergence angle of electrons with energies higher than 1 MeV, 1.5 MeV, 1.7 MeV and 1.9 MeV is 32°, 25.7°, 22.6° and 21.6° (FWHM), respectively.

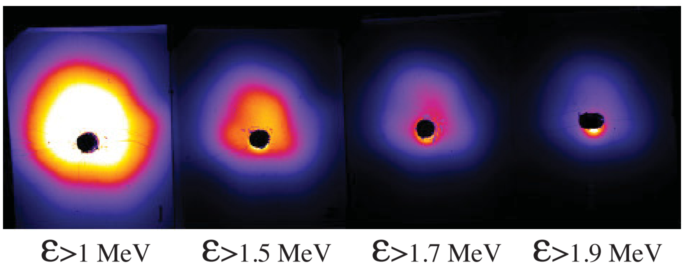

Figure 4.14: Typical images recorded by the IPs in the thin foil target normal direction. The hole corresponds to the entrance pinhole for the electron spectrometer.

Figure 4.13(b) shows the energy spectrum of electrons in the target normal direction at the rear side. After fitted by a Boltzmann disribution with an exponential decay function , the electron temperatures is ~1.4 MeV. For short pulses (of 10s fs), the laser energy is deposited before the expansion starts. The hot electron temperature can be estimated by the ponderomotive potential approximately [7]

$$T_h \approx \Phi_p \approx 1\text{MeV} \times \left(\sqrt{1 + \frac{I\lambda^2}{1.0 \times 10^{19}\text{W}\mu\text{m}^2/\text{cm}^2}}\right) \tag{4.5}$$

in the relativistic regime. For our laser parameters, the hot electron temperature is ~ 2.5 MeV obtained from Eq. (4.5), is in good agreement with the value obtained from the experiments.

Oblique Incidence

Figure 4.15 (a) shows the spatial distribution of electrons accelerated by the laser pulse at the angle of incidence of 45° with a high (in red) and low (in black) laser contrast from the rough Copper foil target. The total number of electrons accelerated to energies higher than 1.5 MeV is 2.0×10^{11} with a high contrast and 1.4×10^{11} with a low contrast pulse. The fraction of electrons emitted from the rear target normal direction is below 10% in both cases. The number of accelerated electrons is larger at $\alpha = 45°$ than that at the laser normal incidence with a high laser contrast for the rough Cu target, the same as in the case of the flat Ti target. Moreover, the Cu target is especially sensitive to the laser incidence angle when the laser contrast is high. An enhancement of the electron number by a factor of 5.5 is achieved when α is increased from $0°$ to $45°$.

We notice that the spatial distribution of electrons emitted from the rough Cu target is quite different under different laser contrast conditions. With a high laser contrast, the angular distribution of electrons shows an asymmetric feature and peak at $\phi = 32°$ in the target front side. The FWHM divergence angle of electrons is $\sim 34°$. While with a low laser contrast, the maximum flux of electrons of F_e=4.1×10^{11}/rad occurs at $\phi = 343°$ at the target rear side with the FWHM divergence angle of 12°. Therefore, to seek for a highly collimated, high flux electron beam with energies of a few MeV for an application, the rough Copper thin foil with 100s nm of thickness obliquely irradiated by a low contrast ultraintense laser pulse can be a good candidate.

In Figure 4.15 (b), the energy spectra of electrons emitted from the Cu target normal direction with different laser contrast conditions are quite similar except the electron number. After fitting the spectra, the effective temperature of fast

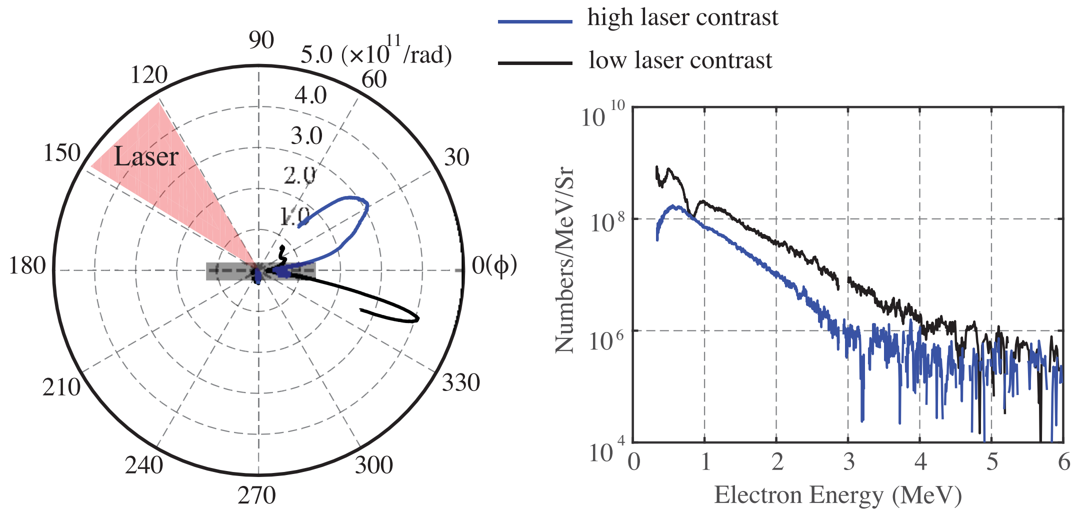

(a) (b)

Figure 4.15: (a) Angular distributions of fast electrons generated by the Ti foil target at a laser incidence of $\alpha = 45°$. Electron energies $\varepsilon \geq$1.5 MeV. (b) Energy spectra of electrons accelerated at the rear target normal direction ($\phi = 270°$).

electrons emitted from the rear target normal direction is about 0.5 MeV.

4.2.3 Flat Target Al (400 nm)

Normal Incidence

Figure 4.16 shows the angular distribution and the energy spectrum of fast electrons accelerated from the flat Al target at laser normal incidence. In Figure 4.16 (a) , the number of electrons emitted by the Al target in the target normal direction is 1.3$\times$10^{10} and amounts to the charge of 2 nC. The total number of electrons (including the surface fast electrons) is 1.5$\times$10^{10}. The FWHM divergence angle of the electrons at the target normal direction is 49°. The shadow of the target at the target surface direction vanishes for the Al target. In Figure 4.16 (b), the effective temperature is 1.6 MeV obtained after fitting the curve.

Oblique Incidence

The experimental results of the angular distribution of electrons accelerated from an Al thin foil at oblique laser incidence (α=45°) with different laser contrast conditions are shown in Figure 4.17(a). The number of electrons per radian

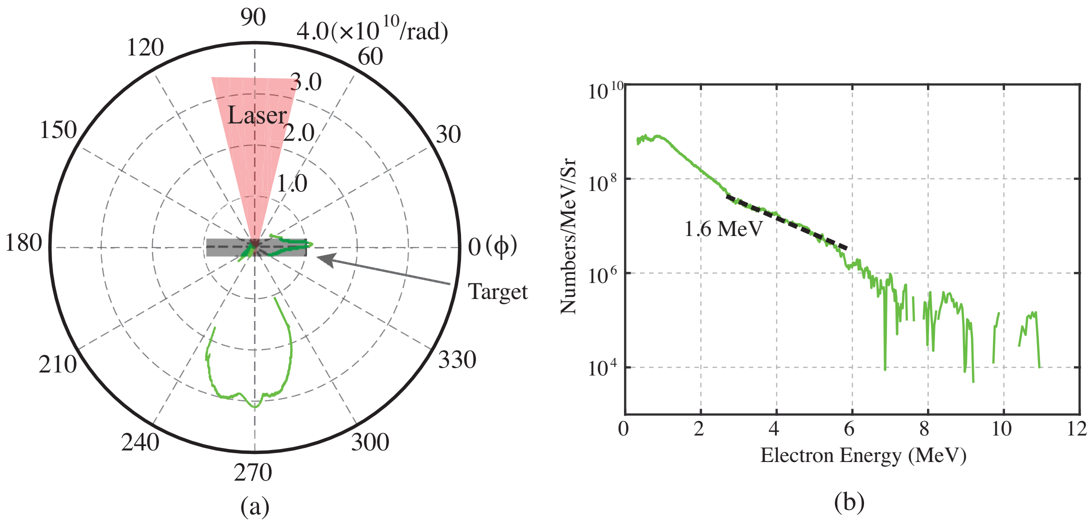

Figure 4.16: (a) Angular distributions of fast electrons generated by the Al target at the laser normal incidence ($\alpha = 0°$). Electron energies $\varepsilon \geq$1.5 MeV. (b) Energy spectra of electrons accelerated on the rear target normal direction ($\phi = 270°$).

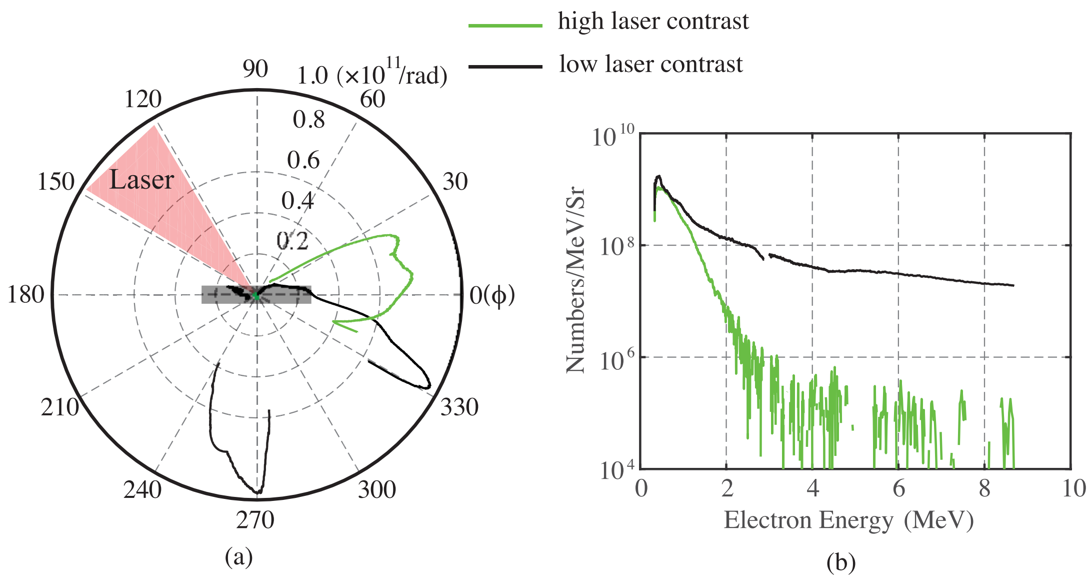

Figure 4.17: (a) Angular distributions of fast electrons generated by the Al target at the laser normal incidence ($\alpha = 0°$). Electron energies $\varepsilon \geq$1.5 MeV. (b) Energy spectra of electrons accelerated at the rear target normal direction ($\phi = 270°$).

is obtained in the same way as for the other targets. It shows that with a high laser contrast, almost all of the electrons are emitted along the target surface direction with the total number of 6.3×10^{10}, and most of them distribute in the target front side. However, with a low laser contrast, about half of electrons emerge in the target normal direction with the total number of 9.4×10^{10}, and a very limited number of electrons are found in the target front side. The electron energy spectra shown in Figure 4.17(b) indicate that the temperature of electrons accelerated from the Al target with a low laser contrast is about 2.5 MeV, much higher than the case with a high laser contrast of 0.3 MeV and very close to the value obtained from Eq. (4.5). Therefore, to obtain electron beams with a high electron temperature, the optimal experimental conditions are 100s nm thin foil targets with a low atomic number and oblique incidence with a low laser contrast.

In summary, we have investigated the electron acceleration in metallic thin foils irradiated by ultraintense laser pulses with different laser incidence and contrast conditions. We tried two different target thickness regimes, i.e. a few μm and 100s nm, different target surface conditions and different target materials. In order to obtain a deeper understanding of the underlying physical processes during the interaction of a short laser pulse with solid thin foil targets, a full parameter scan is necessary.

Chapter 5

Laser Energy Absorption Measurements

Due to the considerable potential applications in inertial confinement fusion (ICF), particle beam acceleration and ultrafast X-ray sources [1, 88, 89], the interaction regime of laser pulses with overdense plasmas is of great interest in recent decades. Vigorous theoretical and experimental efforts have been devoted to identify the interaction conditions for an efficient coupling of the laser energy to solid matters. The influence of the vacuum-plasma interface morphology on the efficiency of the absorption processes was recognized in experiments at low and moderate intensities. Different methods and target engineering have been proposed to enhance the energy fraction deposited on the target including the control of pre-formed plasmas [14, 90], employing targets with surfaces randomly or periodically modulated. Experimental results [19, 91] reported more than 90% energy absorption if ultrashort laser pulses of moderate intensities($\sim 10^{16}\mathrm{W/cm^2}$) are focused onto grating targets or metallic clusters. The role of the target surface topology on the absorption process was revealed indirectly in the experiments where the enhanced soft and hard X-ray yield [92, 93] and the hot electron production [94] have been measured by making use of targets with either randomly modulated surfaces or manufactured structures (array of nanotubes, nanowires, or porous targets).

In this chapter, measurements of the absorption energy fraction of laser pulses for different types of solid targets and geometries are presented. The dependence of the fraction of absorption on different parameters, such as laser intensities, polarization, angles of incidence and different types of targets with flat mirrors, gratings, metallic thin foils and CNTs (carbon nanotubes) are investigated in detail. The motivation of the experimental investigations is to understand the physical processes involved in the transport of laser energy to the overdense plasma under different laser parameters and target surface conditions. The experimental setup of absorption measurements reported in this chapter was introduced in section 3.3. The measurements covered the angle of incidence α between 20° and 70°.

For grating targets, the most efficient absorption up to 65% at an angle of incidence 45° for $P-$polarization was observed. The behaviors of the absorption fraction are mainly dependent on the target surface conditions. The absorption increases with the angle of incidence if the target surface is flat, while for the random rough targets, the absorption is almost independent on the angle of incidence.

5.1 Angular and Polarization Dependence – Grating and Flat Targets

Figure 5.1 shows the angular dependence of the absorbed energy fraction of laser pulses with the plasma mirror in both $P-$ and $S-$ polarization incident onto the grating target G833 and flat Au mirror. The measurements were performed with an average laser intensity of $2.3-2.8\times10^{20}\mathrm{W/cm^2}$ corresponding to the target position in the laser focus. The experimental data are collected on average of $\sim$ 4 shots.

For the grating target G833 in the case of the $S-$polarization laser beam, the absorption drops from $\approx$ 26% at $\alpha = 30^{\circ}$ to $\approx$ 5% at $\alpha = 70^{\circ}$ as the angle of incidence increases. Absorption of the $P-$polarized laser pulse increases for larger angles, from approximately the same values as in $S-$polarization at small angles, reaching its maximum value of $\sim$ 63% at 45°, and decreasing to $\sim$ 28% at $\alpha = 70^{\circ}$. For the flat Au target (the vertical amplitude $h \simeq$ few nm), one may identify a similar angular dependence of the absorption with the grating target in the case of $S-$polarization incidence, i.e. the absorption drops from $\approx$ 22% at $\alpha = 30^{\circ}$ to $\approx$ 5% at $\alpha = 70^{\circ}$. In the case of the $P-$polarized laser beam, the absorption fraction increases monotonously with the increase of the angle of incidence. The maximum absorption for the flat Au target occurs at $\alpha = 60^{\circ}$ with the value of $\approx$ 50%, lower than the grating target value of 63%. It is worth noting here that

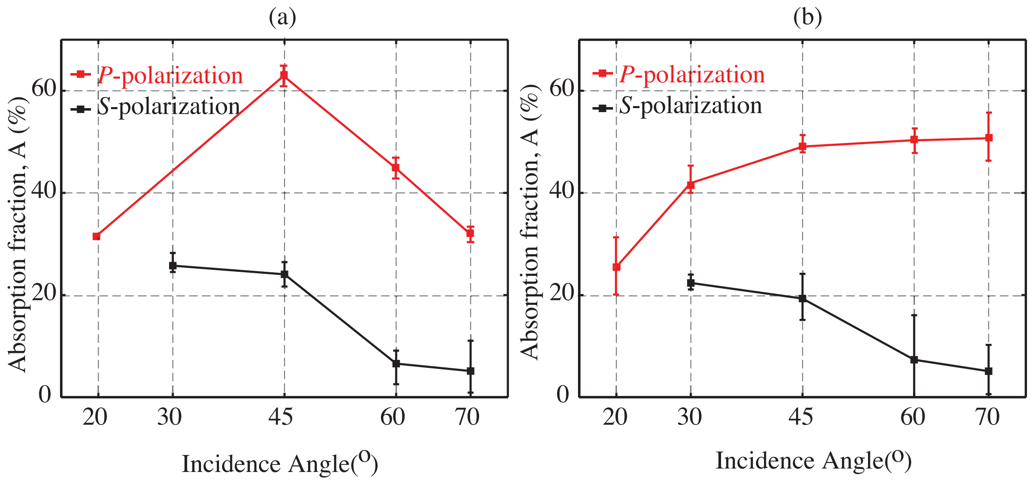

Figure 5.1: Experimental angular dependence of the absorbed fraction A of laser pulse energy by (a) grating target G833 and (b) flat Au target. The data points correspond to an average laser intensity of $2.6 \times 10^{20}\mathrm{W/cm^2}$ with a laser contrast $\sim 10^{-12}$ on a ns timescale.

the larger angle of incidence (>60° and the grazing incidence) is experimentally difficult due to the lateral partial beam distortion by the finite target dimension, such that measuremental errors at $\alpha = 70°$ might be significant.

In the case of the interaction of high intensity $P-$polarized laser pulses with plasmas of very small scalelengths due to our ultra-high laser contrast ($\sim 10^{-12}$), collisionless processes like vacuum heating (Brunel effect), $\boldsymbol{j} \times \mathbf{B}$ heating and anomalous skin effect (ASE) [95] may represent the main absorption processes. Depending on the scalelength of the preplasma, the absorption of the vacuum heating is characterized by a strong angular dependence with the maximum reached at high angles of incidence [96], similar to our experimental observations for flat Au targets. For our interaction conditions, the electron oscillation amplitude ($X_{osc} = eE/m_e\omega_L^2$) which is about 1 μm at the peak of the pulse exceeds the estimated plasma scalelength ($L_n \sim 30$nm), as a prequisite for the vacuum heating process. In the case of a steep plasma profile, the Brunel-like mechanism predicts an enhanced absorption from about 18% at 20° angle of incidence up to 50% at 60°.

We also measured the absorbed energy fraction by different grating targets, and the experimental results are shown in Figure 5.2. We can see that the absorption fractions by different gratings display similar angular dependence. The peak of the laser energy absorption occurs at $\alpha = 45°$ for all the three gratings in contrast with the flat targets where the absorption fraction increases monotonously

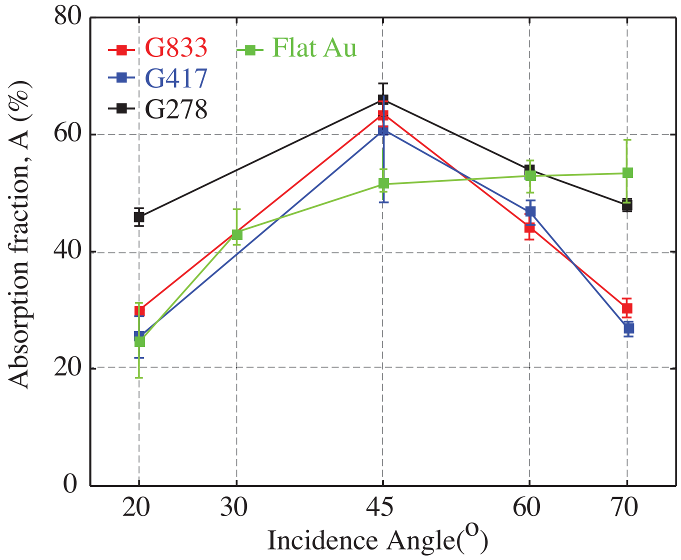

Figure 5.2: Angular dependence of the absorption fraction by different gratings and flat Au targets with the P−polarized laser pulse. The data points correspond to an average laser intensity of $2.7 \times 10^{20}\mathrm{W/cm^2}$ with a laser contrast $\sim 10^{-12}$. The numbers after "G" denotes the groove spacing of the different gratings in unit of nm.

with the angle of incidence. For grating targets at small angles, electrons can be dragged out from the target into the vacuum by $\boldsymbol{j} \times \mathbf{B}$ heating and then reenter into the neighbour cells of the grating to deliver the energy, leading to the higher efficiency of energy absorption by grating targets compared with the flat target at small angles of incidence. The vacuum heating is dominant at large angles of incidence by driving the electron motion in the component of $\boldsymbol{E}$ perpendicular to the target surface. In this case, the grating targets behave similar to the flat target. These observations imply that the optimum angle of incidence of grating targets does not show up at very large angles. It is worth noting that in Figure 5.2 the grating target G278 shows the best absorption performance. Such high energy absorption is perhaps because the more laser energy is converted into kinetic energy of the extremely high energetic electrons in the laser specular direction as the experimental results presented in Section 4.1.1.

It is notable that all three grating targets exhibit higher energy absorption fractions (>60%) than the flat Au mirror (∼50%) at $\alpha = 45°$. Although the absorption fraction of flat Au mirror increases with the angle of incidence larger than 45°, and reach the maximum of ∼55% at the incidence angle of 70°, but it still lower than that of the grating targets at 45°. These results clearly indicate that the targets with periodically modulated surfaces can enhance the energy deposited on the target in agreement with the experimental results of our fast electron acceleration measurements in Section 4.1.2.

Andreev *et al.* [98] found that the periodical target structure with optimum parameters can increase the short-pulse laser absorption and developed an analytical model [99] to explain the absorption dependence on the dimensions of the target structure (h and σ). Compared with the numerical simulation results, they revealed that under our experimental conditions with the laser intensity $\sim 10^{20}\mathrm{W/cm^2}$ and the laser wavelength λ_L =800 nm , the absorption fraction increases first to $\sigma \approx 550$ nm and then decrease while increases linearly with h first and then reaches saturation at $h \gtrsim 0.5$ μm afterwards. The analytical model considers a small angle of incidence and the results are in agreement with our experimental results. The high absorption of structured target compared with a flat one is attributed to the enhancement of electron motions between the neighbour cells and the existence of the modulated structure transferring to the regime of "laser piston" for a long time (~100 fs).

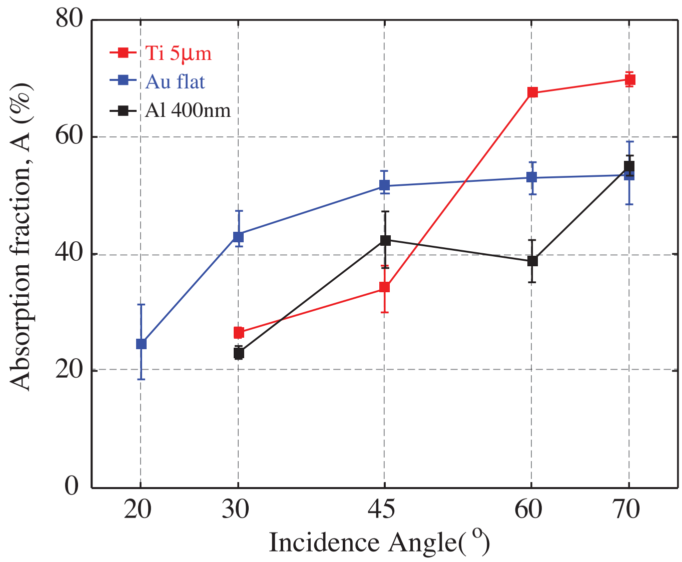

Figure 5.3: Angular dependence of the absorption fraction by different flat targets with the $P-$polarized laser pulse. The data points correspond to an average laser intensity of $2.7\times10^{20}\mathrm{W/cm^2}$ with a laser contrast $\sim 10^{-12}$.

The angular dependence of the energy absorption fraction of flat targets with different geometries and materials is shown in Figure 5.3. All of the three flat targets show a similar angular dependence ignoring shot-by-shot laser energy fluctuations, no matter the target geometries and materials. The energy absorption fraction of flat targets increases with the angle of incidence. However, the absorption variation between different target materials and geometries deserves a more detail study.

5.2 Angular Dependence – Surface Modulation

In the last section, we compared the energy absorption fractions of flat Au targets and surface periodical modulation targets (gratings), and showed that grating targets can improve the energy absorption at an optimum incidence angle of 45°. In this section, we consider the randomly rough targets. As described in Section 3.5, the rough Al plate target used in the experiment has the roughness of $h \approx$1.6 μm, much larger than the scale-length of the preplasma with a high laser contrast, i.e. $L_n \approx$30 nm. The absorption comparison of the rough Al plate with flat Al foil is shown in Figure 5.4.

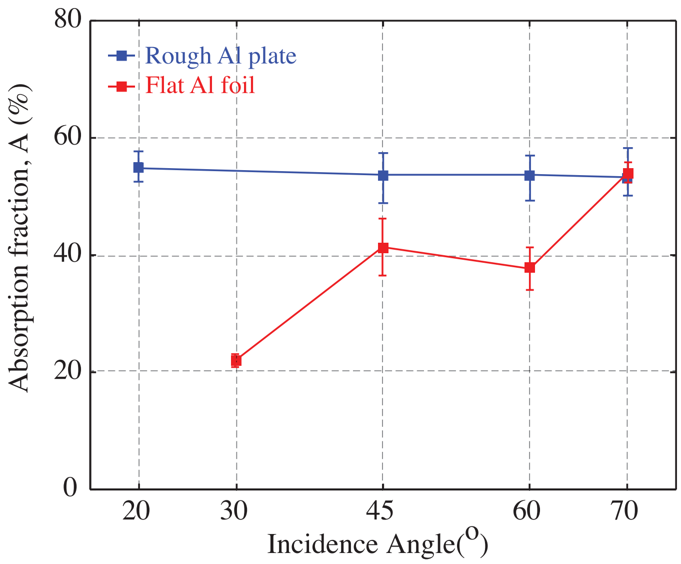

Figure 5.4: Angular dependence of the absorption fraction by Al targets with different surface conditions.

Different from the absorption of the flat Al foil target increasing with the angle of incidence, the energy absorption of the rough Al plate target, as shown in Figure 5.4 in blue, saturates at about 55% of the incident laser energy, and nearly is independent on the angle of incidence. However, at large angles of incidence ($\alpha \sim$70°), the absorption fractions of the two targets reach almost the same level (55%). The random non-uniformity of a rough surface can be described by two spatial parameters: the roughness h and the parameter σ that defines the periodicity of longitudinal modulations along the surface. A laser pulse incident on a rough surface experiences different geometrical structures which can influence the absorption, from various aspects such as incidence under multiple angles, higher order scattering or shadowed areas of the surfaces, strongly depending on the characteristic surface slope h/σ [97]. Within our experimental range of angles of incidence (20° ∼60°), the multiple scattering events are expected to contribute to the angular dependence of the rough Al plate target. The random multiple scattering events attenuate the influence of laser pulse incidence and lead the absorption fraction of rough Al target to be independent almost of the incidence angle.

The laser pulse contrast plays an important role in the interaction of a laser pulse with surface modulated targets. As an effect of the laser prepulse, an expanded preplasma is created in the front of a target which may reduce the longitudinal and transversal surface modulations before the interaction with the main pulse. We estimated that the scalelength of the electron density L_n of the preplasma is the order of 10s of nm. For the target with a roughness h =1.6 μm$> L_n$, the roughness manifests itself by influencing the absorption process.

In the following, the experimental results of the angular dependence of energy absorption by targets with different surface modulations and different roughnesses are discussed. The experimental study of the laser energy absorption by various targets at high intensities ($I > 10^{20}\mathrm{W/cm}^2$) with high contrast ($\sim 10^{-12}$) demonstrates that the angles of incidence and the target surface modulations are affecting the laser energy transfer process.

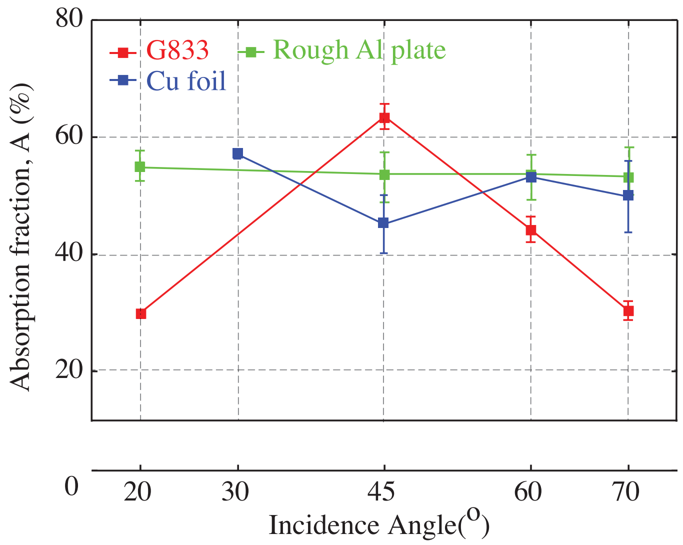

Figure 5.5: Angular dependence of the absorption fraction by rough targets with different surface conditions.

In Figure 5.5, the angular dependence of the laser energy absorbed by rough targets with different surface conditions is shown. As mentioned before, our rough targets have different modulations and roughnesses. The grating targets have periodical structures with the roughness $h \sim 60$ nm. The roughnesses of the Al plate and the Cu foil are 1.6 μm and $\sim$ 30 nm, respectively. In Figure 5.5, one can see that despite the various roughnesses, the absorption fraction of rough targets shows angular independence except for the grating targets, of which the optimum incidence angle occurs at α=45°. The periodical modulation effects may be related to the mechanism of surface plasma waves excited on the grating target surface.

Cerchez *et al.* [100] have investigated the angular dependence of absorption by targets with different roughnesses and shown that once the roughness of the target is comparable to the scale-length of the preplasma, the absorption will be angular independent. Our experimental results also support this description. The Cu foil target with a roughness of 50 nm has an absorption which is angularly independent (Figure 5.5 in blue).

We also measured the energy absorption fraction by CNTs targets. The slightly lower and larger error bar of absorption of CNTs targets mainly comes from the focus uncertainty. The thickness of the CNTs targets is about 100μm, much larger than the Rayleigh length of our laser pulse ($z_R \approx 50\mu$m). Due to its small density ρ <0.3 g/cm^3, the CNTs pile up very loosely. This increases the difficulties to focus the laser pulse on the CNTs target surface. The estimated focal intensity on the CNTs targets is only about $5 \times 10^{19}\mathrm{W/cm}^2$, much lower than that on the metallic thin foil targets with the thickness below few microns.

In summary, the absorption fraction of laser pulse energy by targets with different surface structures were investigated and compared. The angular dependence of absorption by gratings and flat targets is similar when the laser pulse is $S-$ polarized. For $P-$polarized laser pulses with high laser contrast, the target surface periodical modulation can improve efficiently the laser energy coupling to the target at the optimal incidence angle of $\alpha = 45°$. The angular dependence of absorption by grating targets is regardless of the grating periodicity. The absorption fraction of flat targets increases with the angle of incidence and is independent on the target geometries. The absorption by random rough targets is angularly independent.

Chapter 6

Comparison of Simulations with Experimental Results

In order to understand deeply the dynamics of the processes during the interaction of a relativistic short laser pulse and a solid target, additional 2D PIC simulations were performed. Particle-In-Cell code can handle self-consistently the scenario of relativistic electrons by employing the kinetic model instead of classical fluid model. In this chapter, we study numerically the high-intensity laser interacting with the overdense plasma from solid targets and compare with the experimental results in Chapter 4. All calculations in this dissertation were performed on supercomputers using the 2D particle-in-cell code EPOCH [101].

6.1 Simulation Setup

When a ultrashort (with the duration τ_L a few tens of femtoseconds) laser pulse with the intensity $I_L > 10^{20}\mathrm{W/cm}^2$ irradiates a solid target, the target is ionized within one laser cycle. In the simulations the flat and grating targets irradiated at different angles of incidence with the initial electron density $n_e > 100n_c$ (where n_c is critical density) have been considered. The intensity of the laser pulse on the target is $2.5 \times 10^{20}\mathrm{W/cm}^2$ which is sufficiently high to ionize the target within one laser cycle, and the focal spot size is 5 μm (if not stated differently). The other parameters are chosen to match the experimental conditions. The numerical box size was 50 $\times$ 50 μm^2, which is large enough to minimize the boundary influences. A spatial resolution of 50 points per wavelength $\lambda = 0.8\mu$m in each direction and 45 particles per cell have been used. We set the maximum of the laser pulse reaching the target surface at the time of $t = 0$. Figure 6.1 illustrates the simulation box where the laser pulse, propagating from the left-hand side, is focused at $(x, y) = (0, 0)$. The grating target has a sinusoidal profile with the thickness of 14 μm and 4 times ionised gold which corresponds to $n_e = 139n_c$. Field ionisation has been used in the code.

The peak-to-valley depth h measured by AFM are 50 nm for G278, 60 nm for G833 and 80 nm for G1667, respectively. The target geometry in the simulation was designed in agreement with the real target. Figure 6.1(a) shows the electron density of the target in the course of the interaction with the 28 fs long laser pulse at $t = 0$, and (b) depicts the electric field E_y at the same time step as (a). Various simulations were performed in order to study the influence of the grating periodicity, preplasma conditions and the angles of incidence on the electron acceleration. The results are discussed in the following sections.

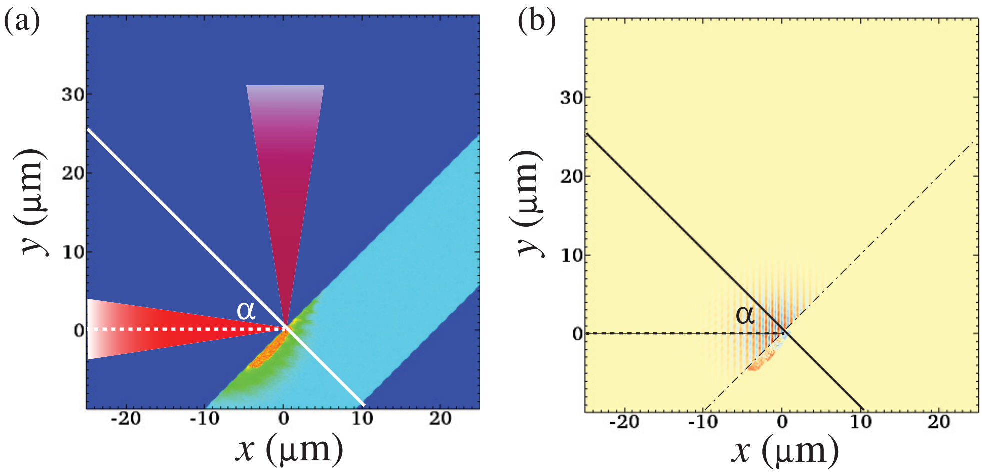

Figure 6.1: Schematics of the simulation box used in the 2D PIC simulations with the EPOCH code. Laser incident from the left-hand side. The angle of incidence α is towards the target normal.
(a) The geometry of the incoming and reflected laser beams and the electron density ($t = 0$).
(b) The electric field E_y. Snapshot is taken at the same time step as (a).

6.2 The Grating Target Compared with the Flat Target

It is well known that the electron acceleration will be more efficient by introducing the periodically modulated target surface (see Ref. [19, 20] and Section 4.1). In this section, the phase diagram, the density, the energy distribution, the angular distribution and the number of electrons generated by the grating target G833 are compared with the data from the flat target in detail to understand the mechanism of electron acceleration in the laser-solid interaction.

To simulate the realistic experimental conditions, the scalelength of the preplasma is set to 30nm which was obtained by 1D MULTI-fs simulation results [103], smaller than the vertical amplitude h of the gratings employed in the experiment. MULTI-fs [102] is a non-relativistic hydrodynamic code for the simulation of the interactions of pico- and femtosecond lasers with matter, especially suitable to calculate the influence of a non-relativistic prepulse on the target. The scalelength of the preplasma ($L_n = n_e/\nabla n_e|_{n_e=n_c}$) calculated by MULTI-fs with the ARCTURUS laser parameters is about 1.5 μm with the low contrast (without the plasma mirror) and about 30 nm with the best contrast (by implanting a plasma mirror with an anti-reflective coated substrate, see Figure 3.2). In this section, we mainly study the enhancement of electron production by the grating target G833 at $\alpha = 45^\circ$ since it showed the best performance in electron acceleration in our measurements and compare it with the flat target.

First, we focus on the acceleration of fast surface electrons which is the characteristic of intense laser beam interacting with dense matter. The Brunel effect, or so-called vacuum heating, one of the collisionless absorption processes, interprets well the mechanism of the intense laser pulse obliquely incident on the steep highly overdense plasma profiles. The electrons are dragged out by the normal component of the electric field to the vacuum and reenter to the target where they deposit the energy, which clearly shows the important role of electric field in the electron acceleration. Figure 6.2 shows the reflected laser pulse at the $t = 32$ fs in the case of $\alpha = 45^\circ$ for (a) the flat target and (b) the grating target G833. In Figure 6.2, it is evident that the localized quasistatic electric field generated close to the surface of the grating target G833 is stronger than that generated by the flat target. Moreover, the reflected laser light is modified by the surface structure of

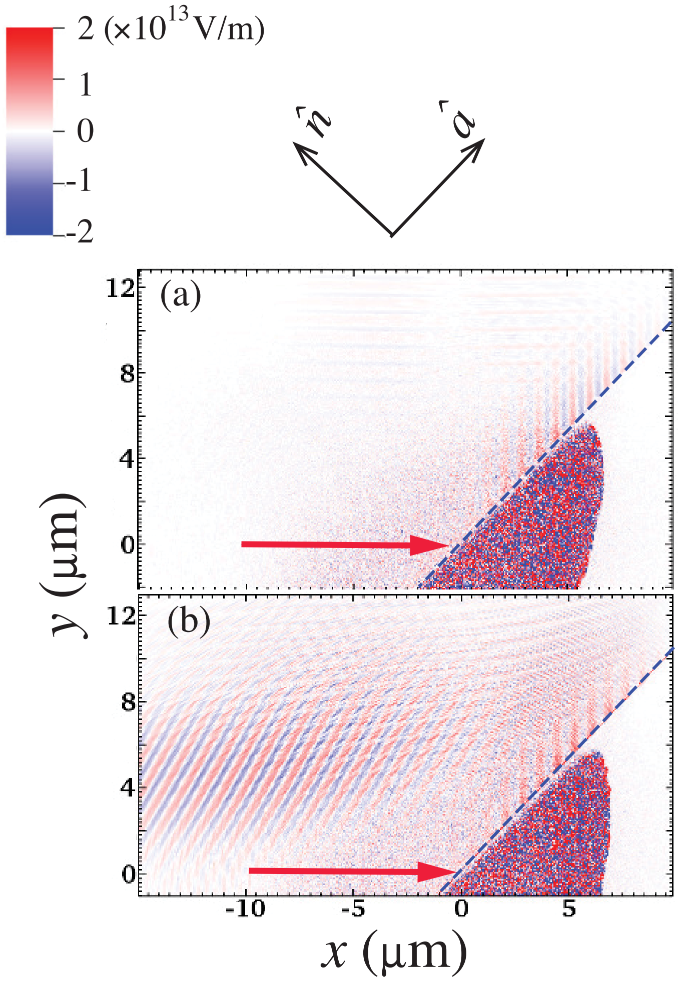

Figure 6.2: 2D-PIC simulation results: snapshots of the component of the electric field normal to the target surface E_n at t=32 fs and $\alpha = 45°$. The dashed blue line is the initial front target surface. $\hat{a}$ is the direction along the target surface and $\hat{n}$ is the direction normal to the target surface. (a) Flat target; (b) Grating target G833.

the grating target, which produces the "fine structure" wave attached to the front side of the grating target. However, the "fine structure" wave propagating along the surface with a velocity close to the light speed does not emerge in the case of the flat target. The electric field shown in Figure 6.2(a) is simply superimposed by the incident and reflected fields.

It is worth noting that the electric field E_y along the front surface of the grating target is unipolar. Figure 6.3 shows the profile of E_y along the target surface direction. The profile of E_y at the front surface of the flat target is nearly symmetric with respect to the polarity as expected. However, this symmetry is broken for the grating target surface as indicated by the red line in Figure 6.3. In the latter case, the amplitude of the positive component is significant compared with the negative part leading to the unipolarity of the electric field. Such that the normal component of the electric field is high enough to extract electrons from the target to vacuum in a long way and the longitudinal asymmetric component accelerates

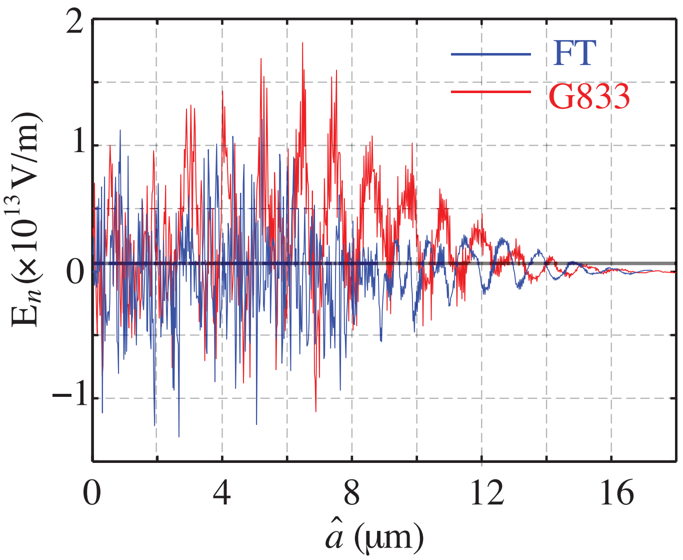

Figure 6.3: The profile of E_n along the target surface direction $\hat{a}$ shown by the blue dashed line in Figure 6.2.

them along the surface incessantly. Consequently, a large number of fast electrons emerge along the target surface direction.

Experiments have shown that the higher-order harmonic radiation can be generated by periodically modulated targets (gratings) irradiated by relativistic, ultrashort (<30 fs), high intensity ($I\lambda^2 > 10^{20}\mathrm{W/cm^2}\mu\mathrm{m}^2$) laser pulses [103]. Figure 6.2(b) shows the fine structures in the right side corresponding to the high harmonics generated by the grating target. These fine structures distribute in a small angular range close to the target surface direction in agreement with the experimental investigations [103] that the high harmonics are emitted along the target surface. However, such a structure is absent in the case of the flat target.

In our experimental results in Figure 4.2, a large fraction of electrons generated by the grating targets with higher energies are emitted close to the laser "specular" direction. The deviation from the specular direction can be attributed to the influence of the modification of the target surface. The laser light pressure ($p = 2I/c$) induces the deformation of the electron density profile on the target surface. Such deformation superimposed on the target original density profile modifies the target surface. To understand such influence, the simulations of the fast electron density and phase diagram are shown in the Figure 6.4, where one can see that the direction of propagation of the most energetic electrons is slightly different from the "specular" one. The alteration of the propagating direction of the reflected light is related to the modification of the target surface. Tuning the initial parameters of the grating target results in the modifications in the phase diagrams of the reflected light and the generated fast electrons.

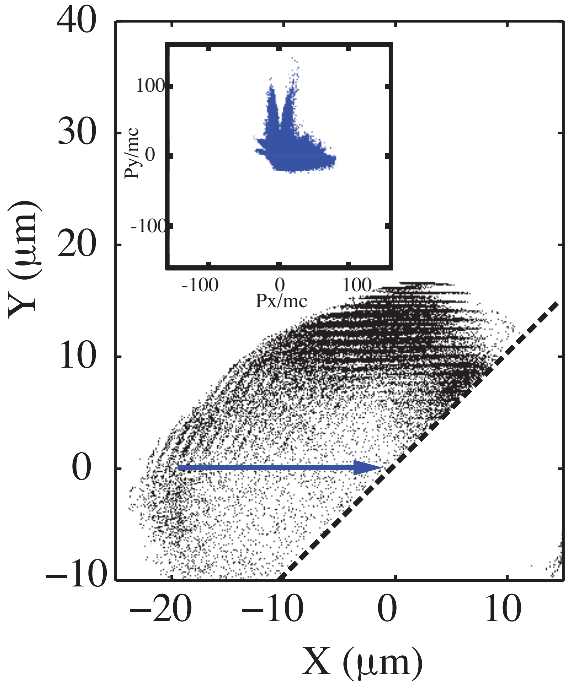

Figure 6.4: 2D-PIC simulations of the electron density spatial distribution at t = 32 fs, filtered at the electron energy ε >1.7 MeV. The blue arrow is the laser propagating direction and the dashed black line is the initial front target surface. The inset shows the electron phase diagram.

6.3 The Effect of Preplasma Conditions

Many experiments and simulations have been devoted to the study the impacts of an underdense, pre-formed plasma in laser-solid interactions and show that the pre-plasma can affect the acceleration and transport of fast electrons drastically [40, 104–108]. The preplasma diminishes the number of electrons with energies between 1-3 MeV while enhances the energy absorbed into the electrons which are hotter than 3 MeV. Note that the energy of the generated electrons is higher than that predicted by ponderomotive scaling ($T_h = \sqrt{1+a_0^2} - 1$, [40]). The preplasma is caused by the laser pedestal arising from intrinsic amplified spontaneous emission (ASE) processes which arrives at the target nanoseconds prior to the main pulse and the prepulses ($-100 \sim -10$ ps). They have sufficient energy to ionize the target surface prior to the arrival of the main pulse. In addition, the "preplasma" can extend hundreds of microns in front of the intended interaction surface .

In our experiments, the plasma mirror is always utilised to preserve the surface structure of the grating targets until the main pulse arrives. Under such conditions, the preplasma is from tens of nanometers to few microns estimated by 1D hydrocode MULTI-fs simulations. Following this estimation, different scalelengths of the preplasma from 0 to 50 nm are chosen to study the influence on the fast electron acceleration is this section. Different grating targets, i.e. sub- (G278), near (G833) and double-(G1667) wavelength gratings are tested with different angles of incidence $\alpha = 30°$ and $45°$.

Electron Energy Spectra vs. Preplasma

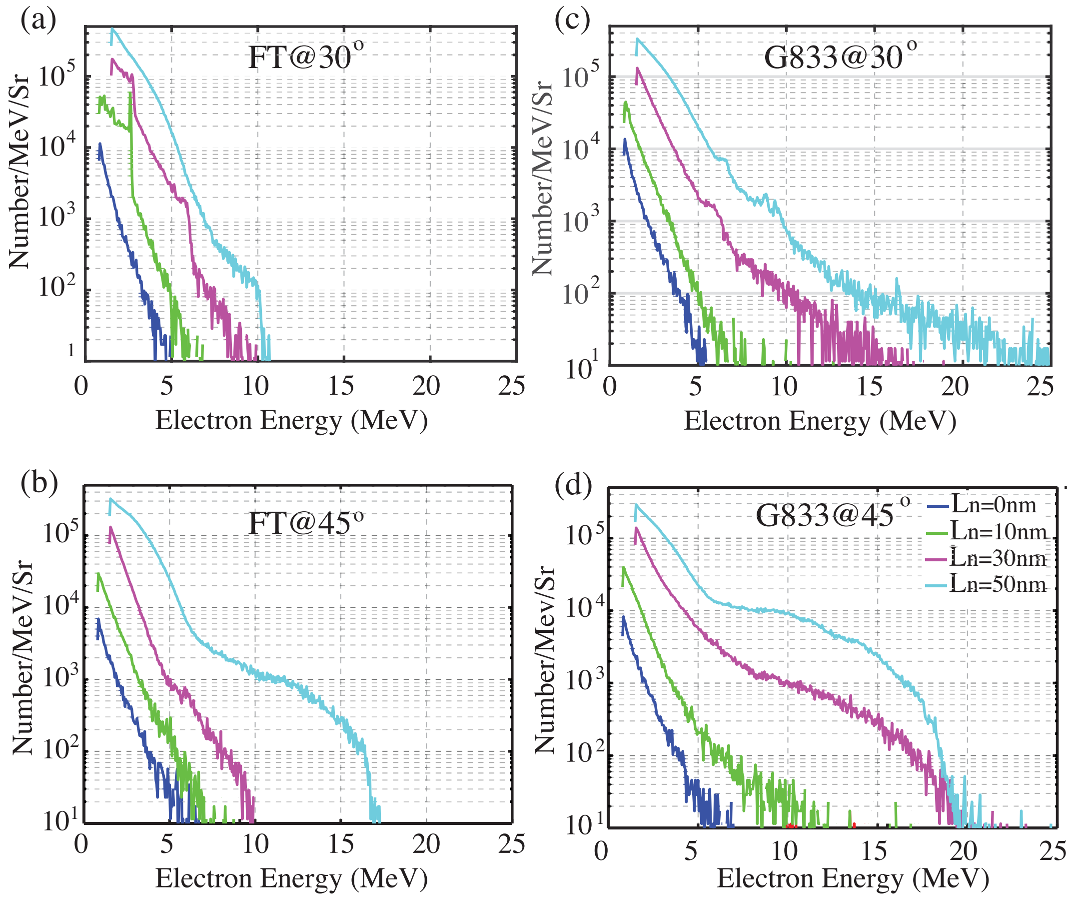

Figure 6.5: The electron energy spectra obtained for (a, b) the flat target and (c, d) the grating target G833 irradiated at $\alpha = 30°$ and $45°$ with different scalelengths L_n of the preplasma. The data are collected in the angular range $\phi = [0°, 10°]$.

Figure 6.5 shows the influence of the preplasma scalelength on the electron energy spectra for the grating target G833 and the flat target with the angle of incidence $\alpha = 30°$ and $45°$ where the absolute value of the slope in the energy spectra corresponds to the effective electron temperature. Obviously, the grating target G833 has a higher efficiency of electron acceleration than the flat target and the hot electrons have a higher effective temperature in the all four cases, which is in agreement with our experimental data (see Section 4.1). For small angle of incidence $\alpha = 30°$, both the FT and G833 are less sensitive to the variations of the preplasma scalelength. From Figure 6.5 (a, c), larger scalelength of the preplasma increases only the number of generated fast electrons but leave the effective temperature of electrons almost intact. When the angle of incidence is increased to $\alpha = 45°$, the electron energy spectra of both the grating target and the flat target change significantly due to the increase of the preplasma scalelength. For the flat target in Figure 6.5 (b), when the scalelength of the preplasma is increased from $L_n = 30$nm to 50 nm, a larger number of electrons with a higher effective electron temperature are generated. Also, the number of hotter electrons with energies $\varepsilon \gtrsim 7$ Mev is increased. In the case of the grating target at larger angle of incidence in Figure 6.5 (d), G833 shows more sensitivity to the preplasma scalelength at $\alpha = 45°$. When the preplasma scalelength $L_n \sim 30$nm, the effective temperature of electrons increases and more electrons hotter than 8 MeV emerges. In the case of $L_n \sim 50$nm, the number of electrons hotter than 6 MeV increases dramatically. By fitting the electron energy spectra in the range of 1−5 MeV, we determined the hot electron temperatures to be $T_e \sim 900$ keV and $T_e \sim 3.3$ MeV in the range of 5−25 MeV.

The sensitivity of energy spectra to the preplasma scalelength increases with the angles of incidence, in a similar way as vacuum heating predicts for electron acceleration (Eq. 2.69, $\eta_{VH} \propto \sin^3\theta/\cos\theta$). The vacuum heating is sensitive to the structure of the target surface [18]. The temperature of the surface fast electrons generated by the grating target is higher than that by the flat target. On the other hand, the efficiency of electron acceleration, as well as the kinetic energy the surface fast electrons obtain in the course of acceleration, increases with the angles of incidence due to the “dragging force” coming from the normal component of the laser electric field.

The Number of Surface Fast Electrons vs. Preplasma

Figure 6.6 shows the dependence of the production efficiency of the surface fast electrons on the preplasma scalelength of the grating target G833 and the flat target at $\alpha = 30°$ and $45°$. It is evident that both the grating and the flat target respond to the scalelength of the preplasma similarly. The efficiency of the surface fast electron acceleration increases with the scalelength of the preplasma both for the grating and the flat target for both angles of incidence. However, the large scalelength of the preplasma has more effects on the large angle of incidence

($\alpha = 45°$). In Figure 6.6, the number of generated SFEs increases almost linearly with the scalelength of the preplasma at $\alpha = 30°$. When $L_n \leq 30$nm, there is no significant difference in the number of generated surface fast electrons at the angles of incidence between $30°$ and $45°$. A dramatic enhancement of SFE generation occurs at $\alpha = 45°$ when the scalelength is increased to 50nm.

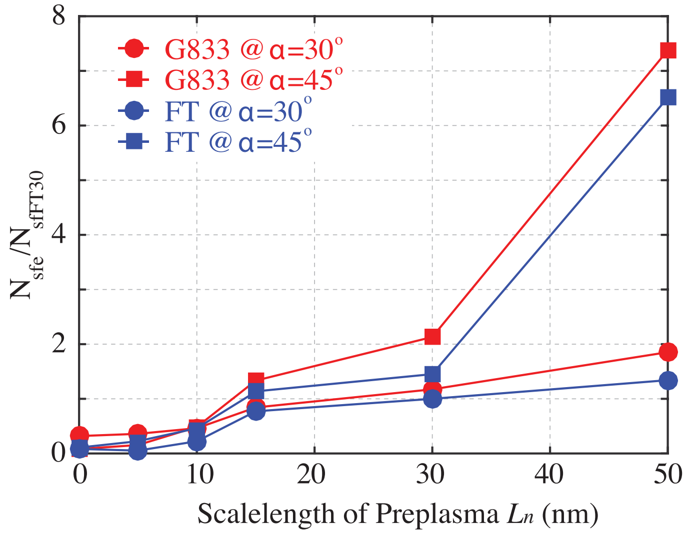

Figure 6.6: 2D-PIC simulation results of the dependence of the number of surface fast electrons ($\phi = [0°, 10°]$) on the scalelength of the preplasma. The electron numbers are normalized by the number of SFEs generated by the FT at $\alpha = 30°$ with $L_n = 30$ nm.

When an ultrahigh ($> 10^{18}\mathrm{W/cm^2}$), ultrashort ($\sim$ femtoseconds) laser pulse interacts with the solid targets, the anomalous skin effect, the vacuum heating (Brunel effect) and $\boldsymbol{j} \times \mathrm{B}$ heating constitute the main mechanisms of the laser energy absorption. In very short scalelength of the preplasma, $\boldsymbol{j} \times \mathrm{B}$ heating is more significant and less dependent on angles of incidence compared with the anomalous skin effect and the vacuum heating. While the vacuum heating becomes dominant when the angles of incidence and the scalelength of the preplasma increase, in agreement with our simulation results shown in Figure 6.6 at $\alpha = 45°$ and $L_n = 50nm$. The acceleration by vacuum heating is angular dependent (Eq. 2.68) and the driving field increases with the angle of incidence.

Therefore, in steep density profiles ($L_n/\lambda < 0.1$), the effective temperature and the number of surface fast electrons are strongly dependent on the scalelength of the preplasma. In particular, for the large angle of incidence, the energy absorption is enhanced evidently in view of that the vacuum heating is efficient at short scalelengths. However, for further larger scalelengths, the above mechanisms are no longer valid. The fraction of the vacuum heating will decrease as L_n increases, leading the temperature and the number of the fast electrons to decrease.

In [22], Gibbon calculated the absorption fraction of both $S-$ and $P-$ polar-

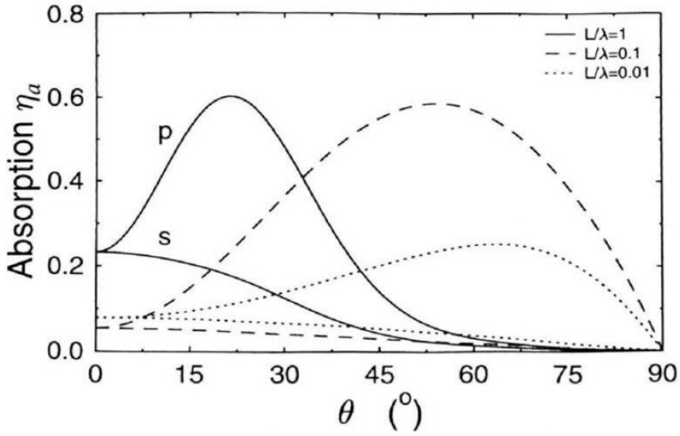

Figure 6.7: Angular absorption dependence for various density scale-length: $L/\lambda_L = 1$ (solid curves), $L/\lambda_L = 0.1$ (dashed) and $L/\lambda_L = 0.01$ (dotted). Figure from [22].

ization for three different scale-lengths as shown in Figure 6.7. It is clear that for $P-$light and oblique incidence, the optimum absorption occurs at mediate value of $L/\lambda_L = 0.1$ which corresponds to the density scale-length of 10s nm. The absorption will decreases for steeper density gradient. Since the number and effective temperature of fast electrons are proportional to the energy absorption fraction, our simulation results support the above analytical curves.

6.4 Resonant Surface Plasma Waves Excitation

In Section 4.1.3, the experimental results indicate that there are additional interaction conditions and effects which influence the excitation of SPWs at the laser intensity $I_L > 10^{20}\mathrm{W/cm^2}$. In order to quantitively understand the SPWs excitation in this new regime, in this section, the parameters such as laser intensities and the angles of incidence are scanned with the 2D PIC code EPOCH to confirm the impact of nonlinear effects of SPWs excitation in electron acceleration mechanism and investigate the characteristic of electron acceleration of SPWs excitation in the nonlinear regime.

We pay close attention to the surface fast electrons accelerated by the SPWs excitation. Figure 6.8 shows the simulation results of the number of SFEs in the interval $\phi \in [0°, 10°]$ generated by the G1667 with energies higher than 1.5 MeV at $\alpha = 20°$, $30°$ and 45°. In case of a preplasma of 30nm scale-length (which was obtained from the 1D hydrocode MULTI-fs simulation using our laser pulse parameters) and the low laser intensity of $2.5 \times 10^{18}\mathrm{W/cm^2}$, the simulation in Figure 6.8 (right *y*-axis) shows the most efficient angle peaks at $\alpha = 30°$ indicating

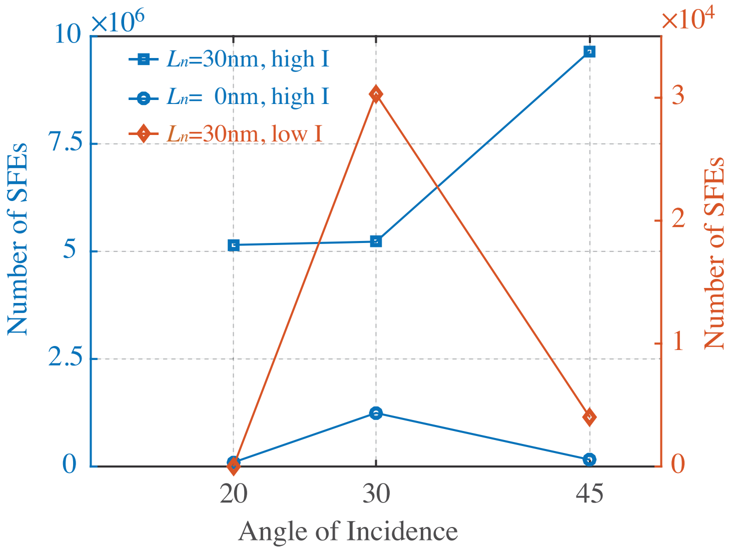

Figure 6.8: 2D PIC simulation results of the number of SFEs. Here high I: $I_L = 2.5 \times 10^{20}\mathrm{W/cm^2}$, low I: $I_L = 2.5 \times 10^{18}\mathrm{W/cm^2}$. The electron energies$\geq$ 1.5 MeV.

the SPWs excitation takes place. The efficient peak also appears at a high laser intensity of $2.5 \times 10^{20}\mathrm{W/cm^2}$ (left *y*-axis) without the preplasma. However, when the scalelength of the preplasma is 30 nm, the resonant peak vanishes and the number of SFEs increases with the angle of incidence at the high laser intensity (left *y*-axis). The number of SFEs generated at $\alpha = 45^\circ$ is larger than that at 30°. Moreover, the number of SFEs generated in the presence of the preplasma is larger compared with the case without the preplasma at the same laser intensity. In the absence of a preplasma and low laser intensity, no electrons with energies higher than 1.5 MeV are produced. The total number of electrons emitted in the target surface direction exhibits similar behaviors with the case of a preplasma with the scale-length of 30 nm and high laser intensity. The disappearance of the resonance peak and the increase of the number of SFEs when the laser intensity is higher than $10^{20}\mathrm{W/cm^2}$ also indicate the extra effects have to be considered in the laser-grating interaction when the preplasma emerges.

To understand the acceleration mechanism driven by the SPWs excitation on the target G1667, two typical electron energy evolution and their trajectories in space are plotted in Figure 6.9 without preplasma, i.e. $L_n \approx 0$. The representative trajectory of electron e1 (red) is parallel to the target surface plane and adhere to it. The electron e1 is accelerated continuously along the oscillating trajectory with the frequency $\omega = 1/2\omega_L$ and the energy increases slowly when the electron moves far away from the laser focal spot where the laser fields and quasistatic fields become weak. However, the electron e2 experiences first the betatron acceleration inside a laser self-focusing channel (in a scheme similar to that proposed

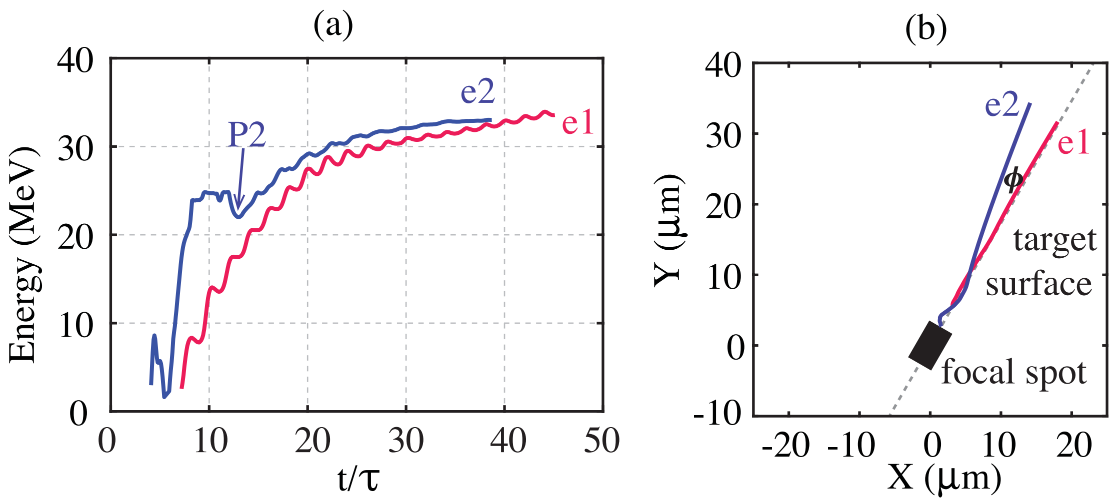

Figure 6.9: The typical energy evolution and trajectories in space of the electrons generated by the SPWs excitation at $L_n \approx 0$. The target $\lambda_g \approx 2\lambda_L = 1667$ nm, the angle of incidence $\alpha = 30°$. (a) The temporal evolution of electron energies; (b) The spatial electron trajectories.

by Pukhov *et al.* [109]) in the initial stage (before positions P2), then the SPWs excitation acceleration follows afterwards. The betatron acceleration is found near the laser focal spot where both the laser fields and quasistatic fields are strong. Since the electron e2 is in the motion away from instead of adhere to the target surface plane, the SPWs excitation acceleration decays quickly compared with electron e1 and the final energy of e1 is larger than that of e2.

The angle ϕ between the trajectory of e2 and the target surface plane is determined by the velocity of the electron when it escapes the scope of the betatron acceleration. Larger ϕ and less SPWs excitation acceleration result in the lower final electron energy. It is obvious that these two acceleration processes are dominant in different regions. For the two electron trajectories given in Figure 6.9, it appears that e1 is accelerated dominantly by the SPWs excitation in the second stage, while e2 is accelerated dominantly in the betatron oscillation process.

To figure out the influence of the preplasma on the electron acceleration by the SPWs excitation mechanism, the electron energy evolution and their trajectories in the presence of the preplasma with $L_n = 30$ nm are shown in Figure 6.10 for comparisons. The electron e1 coming from the laser focal spot region first undergoes the betatron acceleration achieving kinetic energy, then it is confined by the quasistatic surface magnetic field and moves along the target surface where it

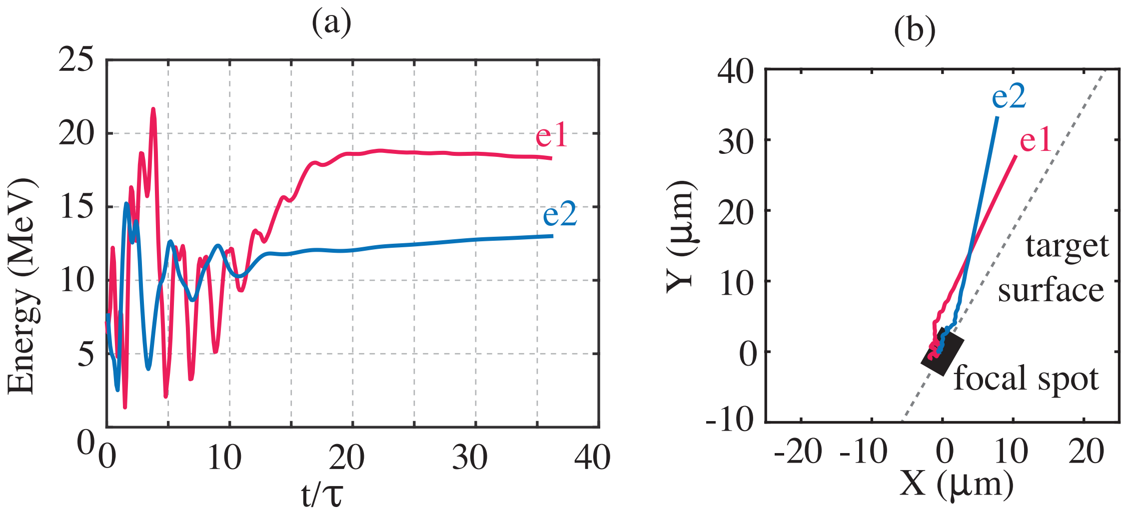

Figure 6.10: The typical energy evolution and trajectories in space of the electrons generated by the SPWs excitation at $L_n = 30$ nm. The target $\lambda_g \approx 2\lambda_L = 1667$ nm, the angle of incidence $\alpha = 30°$. (a) The temporal evolution of electron energies; (b) The spatial electron trajectories.

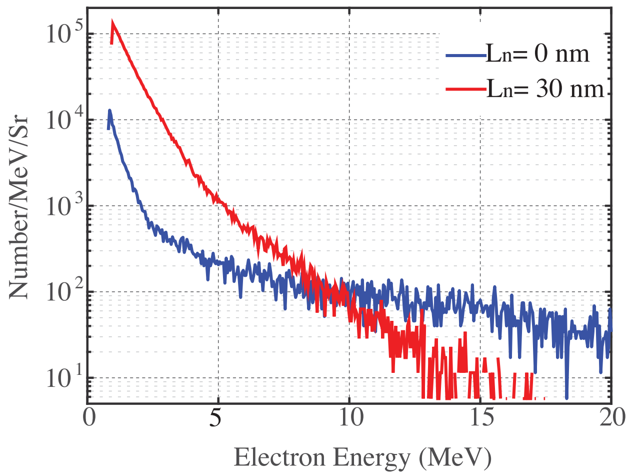

Figure 6.11: The electron energy spectra of the grating target G1667 under resonant SPWs condition with different scalelengths of the preplasma. The data are collected in the angular range $\phi = [0°, 10°]$

is accelerated by the SPWs excitation. Due to the preplasma, the electron cannot adhere the target surface and the effects of SPWs acceleration are weak. When the electron propagates away from the target (e2), the SPWs acceleration can be negligible and lower final electron energy results. The electron spectra with $L_n = 0$ and 30nm are shown in Figure 6.11. The simulations show that SPWs excitation accelerates the electrons efficiently to high energy without the preplasma. However, a larger number of electrons can be generated in the presence of a preplasma with proper scalelength ($L_n/\lambda_L < 0.1$)

6.5 Analytical Model for the Nonlinear Regime

In order to analytically approach the SPWs excitation in our new relativistic regime, we revised the linear model of SPWs and its simple scaling discussed in Refs.[25, 30] by taking into account the finite value of the parameter $\eta = n_e/n_c$ (see Eq. 2.99). This condition is rather close to the realistic experimental conditions of high intensity laser pulses interacting with the solid targets. At these high intensities ($I > 10^{20}\mathrm{W/cm^2}$), the laser pedestal (with all possible pulse cleaning techniques) is still able to generate the preplasma with $0 < L_n/\lambda_L \ll 1$. We consider a high intensity, ultrashort, P-polarized laser pulse obliquely incident from vacuum onto a solid target. Electron motion will be treated relativistically due to the high laser intensity while ion motion will be neglected during the interaction due to the ultrashort pulse length of the order of 100 fs or less. Figure 6.12 is the schematic geometry of the analytical model. The basic equations set consists of Maxwell equations and the fluids equations:

$$
\begin{aligned}
&\frac{\mathrm{d}}{\mathrm{d}t}\frac{m\mathbf{v}}{(1-\mathbf{v}^2/c^2)^{1/2}} = -\frac{e}{c}\frac{\partial \mathbf{A}'}{\partial t} + e\mathbf{E}' + \frac{e}{c}(\mathbf{v}\times\boldsymbol{\nabla}\times\mathbf{A}') - T\frac{\nabla n}{n},\\
&\frac{\partial n}{\partial t} + \boldsymbol{\nabla}\cdot(n\mathbf{v}) = 0,\\
&\boldsymbol{\nabla}\cdot\mathbf{E}' = 4\pi e(n - Zn_i),\\
&\boldsymbol{\nabla}^2\mathbf{A}' - \frac{1}{c^2}\frac{\partial^2\mathbf{A}'}{\partial t^2} = -\frac{4\pi}{c}en\mathbf{v} - \frac{1}{c}\frac{\partial \mathbf{E}'}{\partial t}.
\end{aligned}
\tag{6.1}
$$

The vector potential $\mathbf{A'}$ denotes the transverse electromagnetic field and $\mathbf{E'}$ is the longitudinal field originating from charge separation in the plasma. m, e, n, $\mathbf{v}$ and T are the mass, charge, density, velocity and temperature of electrons, respectively. The density and charge number of background ions are denoted by n_i and Z. It is more convenient to consider the wave electric field E instead of the vector potential A. We consider the fields in vacuum including the incident and the reflected waves. The incoming wave with a wave number $\mathbf{k}$ produces two new waves at $\mathbf{k}\pm\mathbf{K}$ after diffracted from a purely sinusoidal perturbation $\sin(Kz)$. Such an approximation corresponds to the two-wave theory of diffraction (see for example [110]) and is valid for the lowest order expansion in A. Therefore, the

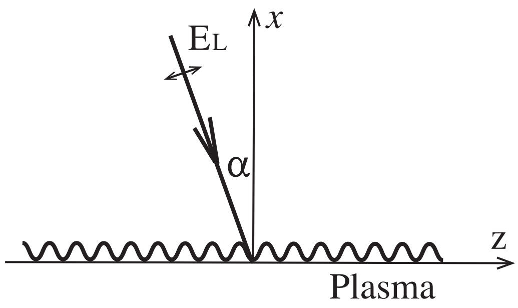

Figure 6.12: The schematic of the analytical simulation.

electric fields in the vacuum region are of the form

$$\begin{aligned}
E_x \approx & E_i \sin\alpha \exp(-ik_x x + ik_z z) + \\
& \sum_{q=0,\kappa} E_{qx} \exp(i(k_z+q)z + \Gamma_q x) + c.c. \\
E_z \approx & E_i \cos\alpha \exp(-ik_x x + ik_z z) + \\
& \sum_{q=0,\kappa} \frac{i\Gamma_q}{k_z+q} E_{qx} \exp(i(k_z+q)z + \Gamma_q x) + c.c. \\
\Gamma_q^2 = & -\omega^2/c^2 + (k_z+q)^2.
\end{aligned} \tag{6.2}$$

The first term corresponds to the incident field, $q = 0$ is the reflected field and $q = \kappa = 2\pi/d$ the surface wave field with the wave vector $k_z + 2\pi/d$ (d is the wavelength of the grating).

The electric fields in the plasma are defined as:

$$\begin{aligned}
E_x^p \approx & \sum_{q=0,\kappa} E_{qx}^p \exp(i(k_z+q)z + \gamma_q x) + c.c. \\
E_z^p \approx & \sum_{q=0,\kappa} \frac{i\gamma_q}{k_z+q} E_{qx}^p \exp(i(k_z+q)z + \gamma_q x) + c.c. \\
& \gamma_q^2 \cong -\omega^2\varepsilon(\omega)/c^2 + (k_z+q)^2.
\end{aligned} \tag{6.3}$$

In the sum term, $q = 0$ corresponds to the transverse wave field screening in the plasma and $q = \kappa = 2\pi/d$ the surface wave field propagating in the plasma with the wave vector $k_z + 2\pi/d$. The plasma permittivity is assumed large enough as $\gamma_q^2 \cong -\omega^2\varepsilon(\omega)/c^2 = \gamma^2$. The amplitudes of the field in x and z components are connected with each other because $\nabla \cdot (\varepsilon \boldsymbol{E}) = 0$. To calculate the amplitudes of spatial harmonics we use the boundary conditions on the plasma surface $x = f(z) = h/2\sin(qz)$, with the same form as that used in numerical simulations. The peak-to-valley depths $h < \lambda_L$ but $h \geq L_s = c/\omega\sqrt{\eta}$ where L_s is the skin layer depth.

We expand the exponential functions with Fourier series and take into account only two harmonics: $\exp(ik_z z)$ and $\exp[i(k_z+\kappa)z]$. Eqs.(6.2–6.3) give four equations with four unknown quantities in view of continuity of the fields on boundaries

$$
\begin{aligned}
&(E_i+E_0)\sin\alpha J_0 + E_\kappa(-iI_1(h\Gamma/2)+\frac{ih\kappa\Gamma I_0(h\Gamma/2)}{4(k_z+\kappa)})\\
&\qquad = \varepsilon E_0^p I_0 + E_\kappa^p(i\varepsilon I_1 - \frac{i\varepsilon h\kappa\gamma}{4(k_z+\kappa)}I_0),\\
&E_i(-J_1\sin\alpha-\frac{h\kappa J_0}{4}\cos\alpha)+E_0(J_1\sin\alpha+\frac{h\kappa J_0}{4}\cos\alpha)+E_\kappa I_0(h\Gamma/2)\\
&\qquad = \varepsilon E_\kappa^p I_0 + E_0^p(-i\varepsilon I_1 - \frac{i\varepsilon h\kappa\gamma}{4(k_z+\kappa)}I_0),\\
&(E_i-E_0)\cos\alpha J_0 + E_\kappa(\frac{h\kappa}{4}I_0(h\Gamma/2)-\frac{\Gamma I_1(h\Gamma/2)}{4(k_z+\kappa)})\\
&\qquad = E_0^p I_0\frac{i\gamma}{k\sin\alpha} + E_\kappa^p(-\frac{\gamma I_1}{k\sin\alpha+\kappa}+\frac{h\kappa}{4}I_0),\\
&E_i(-J_1\cos\alpha+\frac{h\kappa J_0}{4}\sin\alpha)+E_0(-J_1\cos\alpha+\frac{h\kappa J_0}{4}\sin\alpha)-E_\kappa I_0\frac{i\Gamma(h\Gamma/2)}{k_z+\kappa}\\
&\qquad = E_\kappa^p I_0\frac{i\gamma}{k\sin\alpha+1} + E_0^p(\frac{\gamma I_1}{k\sin\alpha}+\frac{h\kappa}{4}I_0),
\end{aligned}
\tag{6.4}
$$

where $J_{0,1}\equiv J_{0,1}(k_x h/2)$, $I_{0,1}\equiv I_{0,1}(\gamma h/2)$ are the Fourier function and modified Bessel functions of order 0 and 1, respectively, $\Gamma\equiv\Gamma_q$. It is worth emphasizing that the system described by Eqs. (6.4) depends in an essentially nonlinear manner on the amplitudes h. The nonlinearity starts to affect, when the surface oscillation amplitude becomes of the order of the skin layer depth, $\gamma h\sim 1$. The equation system (6.4) can be solved analytically.

The model indicates that the preplasma density parameter η plays a key role during the excitation of SPWs. In a real situation, the electron density profile is modified by the prepulse heating to the formation of an electron Debye layer, $n_e(x)=Zn_i\exp{-x/r_D}$ where $r_D=\sqrt{T_e/4\pi e^2 n_e}$ is the Debye radius. The plasma density parameter η is amended by the period surface modulation and has the form

$$\eta_{\text{eff}}\approx\frac{\eta}{\gamma_e}\sqrt{1+r_D^2/4\pi^2d^2} \tag{6.5}$$

where $\gamma_e=\sqrt{1+a_\kappa^{p2}}$ and $a_\kappa^p=eE_\kappa^p/m\omega$.

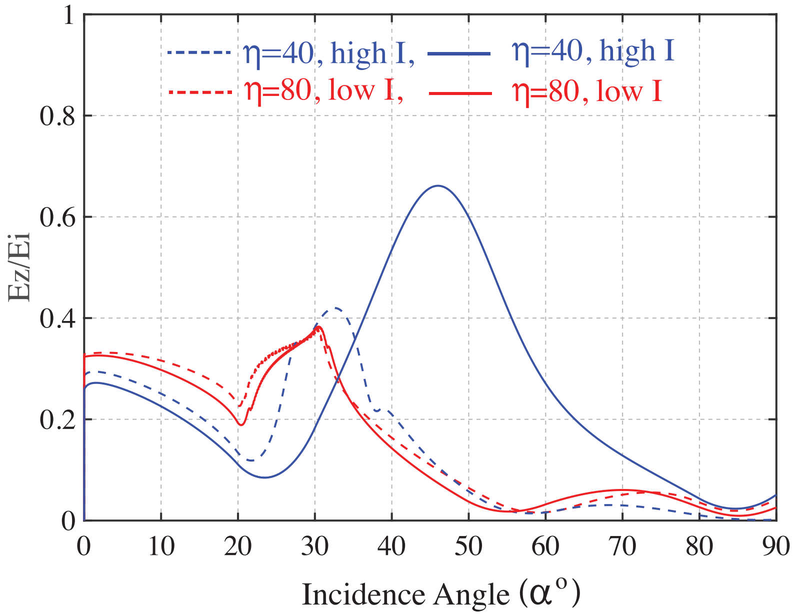

Figure 6.13: The dependence of longitudinal (along target surface) normalized electric field component E_z/E_i on α, the angle of laser incidence on grating at different laser intensities, but the same plasma inhomogeneity. Here high I: $I_L = 3 \times 10^{20}\mathrm{W/cm^2}$, low I: $I_L = 3 \times 10^{18}\mathrm{W/cm^2}$.

We pay close attention to the surface fast electrons which are corresponding to the tangent component of the surface wave. Fig. 6.13 shows the equation system (6.4) results of the tangent (z) surface wave component in a vacuum as a function of the angles of incidence α at different laser intensities ($3 \times 10^{20}\mathrm{W/cm^2}$ and $3 \times 10^{18}\mathrm{W/cm^2}$) with different parameter η (40 and 80). We choose r_D =0.1 μm and $d/\lambda_L = 2$. In this figure it is clear that at low intensities and steeper preplasma presence ($\eta = 80$), the resonance peaks occur at $\alpha = 30°$, which follows the linear SPW model. When the laser intensity increases to $3 \times 10^{20}\mathrm{W/cm^2}$, the non-linear effects shift the resonance to $\alpha = 32.5°$. In addition, the presence of moderate preplasma ($\eta = 40$) together with a high laser intensity increases the resonant angle further to $\alpha = 46°$. Besides, at high laser intensities, the preplasma leads to the increase of the value of E_z/E_i from 0.42 to 0.66, which signifies that more electrons will be accelerated to higher energies. However, it is also worth mentioning that the non-linear effects of preplasma on the SPWs resonance angle shifting take place only at high laser intensities. At low laser intensities, such impacts are very limited and can be negligible. These results indicate that the SPWs resonance angle and the efficiency of fast electron acceleration are affected by the non-linear effects induced by the ultra-relativistic laser intensity and the moderate pre-formed plasma. The non-linear effects causes the SPWs resonance angle to be larger than that predicted by the linear SPWs model and the enhancement of the electron acceleration efficiency in the SPW excitation mechanism, which is in agreement with our experimental observations.

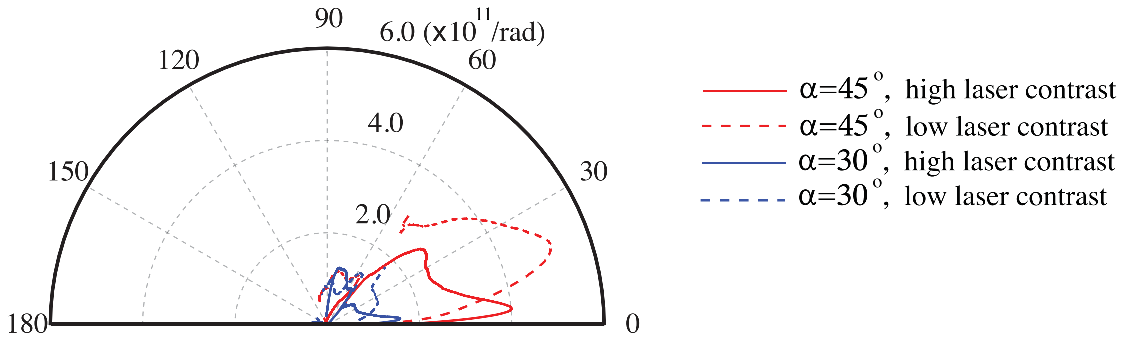

Figure 6.14: The angular distribution of fast electrons generated by the grating target G1667 at angles of incidence of 30° and 45°.

Experimentally, the fast electrons with energies higher than 1.5 MeV generated by the grating target G1667 were recorded by IPs and shown in Figure 4.4(a) and (b). The electron angular distribution at different angles of incidence for high and low laser contrasts is shown in Figure 6.14. After absolute calibration, the number of surface fast electrons ($\phi \in [0°, 10°]$) at $\alpha = 45°$ is 3.4 times of that at $\alpha = 30°$ and the total number of fast electrons ($\phi \in [0°, 180°]$) is 5.3 times. The simulation results (Figure 6.8) gives the efficiency of SFEs acceleration at $\alpha = 45°$ is about 2 times of that at $\alpha = 30°$ at a high laser intensity with the scalelength of the preplasma 30nm, which is in agreement with the experimental results quantitatively. The simulation results indicate that the ultrahigh ($I > 10^{20}\mathrm{W/cm^2}$) laser intensity and the presence of a preplasma ($L_n \sim$ tens of nanometers) will make the linear resonant SPWs invalid and the resonant angle is increased. The analytical model helps to understand such non-linear effects further in quantitative simulations. The tangent component of the surface wave field accelerates the electrons along the target surface direction which can be denoted as the efficiency of the SFE acceleration. In Figure 6.13, it is clear that the increase of the laser intensity will improve the efficiency of the SFE acceleration. Moreover, the presence of preplasma ($\eta = 40$) shifts the resonant angle towards larger angles. Both the numerical and the analytical simulations indicate that the two factors, the ultra-high laser intensity and the moderate preplasma profile, cause the SPW resonant angle to increase and the efficiency of fast electron acceleration to enhance as observed in the experiments. Both of them can trigger the non-linear effects in the SPWs excitation mechanism.

However, the very steep profile of the preplasma is still the prerequisites for generating the high flux, collimated fast electron beams. The optimal scalelength of the preplasma is of the order of $10s$ nanometer. We also investigated the fast electron acceleration on the grating targets without the plasma mirror, i.e. with the low laser contrast (shown in Figure 6.14 in dash lines). The estimated scalelength of the preplasma is $\sim 1.5\mu$m, larger than the wavelength of the laser pulse. Under these conditions, a very small number of electrons are emitted along the target surface direction. The electron flux peaks at $\phi \approx 20^\circ$ and the energies of electrons are below 3 MeV.

In summary, we have developed a new analytical model of surface fast electrons by using grating targets under SPWs resonant conditions at laser intensities higher than $10^{20}\mathrm{W/cm^2}$. At a such high relativistic laser intensity regime, a higher efficiency of fast electron acceleration is found at angles of incidence larger than the resonant angle predicted by the linear SPWs model. These results are in agreement with our experimental and numerical results. Our results also suggest that the number of fast electrons instead of their energies can be increased remarkably by using grating targets and further optimized by tuning the preplasma conditions.

Chapter 7

Summary and Outlook

In this dissertation, the interaction of high contrast, 28 fs relativistic laser pulse with solid targets was studied. The laser pulses were focused onto solid targets achieving with a focal spot of 5μm diameter (FWHM) an average intensity of $\approx 2.5 \times 10^{20}\mathrm{W/cm^2}$ with the plasma mirror and $\approx 3.5 \times 10^{20}\mathrm{W/cm^2}$ without the plasma mirror. With the main aim of understanding the fundamental physical processes occurring when an ultrashort relativistic laser pulse is focused onto a solid surface, the experiments have been conducted in two investigation directions: electron acceleration observations and laser energy absorption measurements. Benefiting from the high temporal laser contrast ($\sim 10^{-12}$) with the plasma mirror system, the experiments have been performed in a interaction regime where the influence of preplasma effects is very limited.

In the first part of this work the electron acceleration was investigated. The plasma mirror system was used in order to allow experiments with thin or structured targets with the ARCTURUS laser. An enhancement of surface accelerated fast electrons generated by grating targets irradiated by laser pulses with intensities higher than $10^{20}\mathrm{W/cm^2}$ was observed. The surface fast electron flux peaks along the grating surface direction while a fraction of electrons with higher energies concentrates close to the laser specular direction. The wavelength-scale grating shows the best performance in surface fast electron acceleration at an angle of incidence of $45°$ compared with the sub- and double-wavelength grating targets. However, larger angles of incidence are desired to obtain higher collimated and larger flux electron beams. The results also indicate that we are able to increase the number of fast electrons by using grating targets compared with the flat targets. No grating effects were observed with low laser contrast since the surface structures are smoothed due to the prepulse heating before the main pulse arrives at the target surface.

The number and the effective temperature of fast electrons generated by thin foil targets is strongly dependent on the thickness of the thin foil target and the laser beam incidence angle with a high laser contrast. Moreover, the target dimensions and ground conditions also influence the SFE acceleration. Larger dimension and grounded targets show a higher efficiency of SFE acceleration.

In the second part of this work the absorbed energy fraction coupling to the targets A was measured. $A = 1 - R$ where R is the reflected laser energy fraction which was measured by an Ulbricht sphere. The absorbed fraction is dependent on several physical parameters, such as laser polarization, laser incidence angle, target type and surface roughness. In measurements these parameters were taken into account.

The absorbed laser energy fraction by grating targets and flat mirror targets was investigated and compared. For these two types of targets, the absorption of the $P-$polarization laser pulses exceeds the $S-$polarization absorption significantly. The experimental results proved that the energy of the $P-$polarization laser pulses can be absorbed increasingly with the laser incidence angle by the flat mirror targets. However, the grating targets show an optimal angle of incidence of $45°$ for the absorption fraction up to 65% regardless of the grating periodicity.

For the thin foil targets, the dependence of energy absorption is similar with the bulk targets, which is strongly influenced by the roughness of the target surface. For flat foil targets, the energy absorption increases with the thin foil target thickness and the angle of incidence. While for rough foil targets, the absorption fraction is independent on the laser incidence angle. The variation in the energy coupling to the target between the flat metallic thin foils and flat bulk targets indicates alternative absorption mechanisms exist for the former targets which deserves a deeper investigation.

The experimental results were compared and interpreted by the numerical and analytical simulations. The interaction of the ultrashort laser pulses with grating targets was simulated using the EPOCH PIC code. The self-sustained surface electric and magnetic fields, electron diagram and density spatial distribution were used to explain the more efficient SFE acceleration. The influence of the preplasma conditions is studied comprehensively on the influence of the electron energy spectra and SFE acceleration. At last, the numerical and analytical simulation gave results in agreement with the experimental results, and interpreted the resonant angle shifting and non-linear effects of preplasma in SPWs excitation mechanism theoretically.

Appendix:

Introduction to the Particle-In-Cell Code EPOCH

EPOCH is a plasma physics simulation code which uses the Particle in Cell (PIC) method. In this method, collections of physical particles are represented using a smaller number of pseudoparticles, and the fields generated by the motion of these pseudoparticles are calculated using the finite difference time domain technique on an underlying grid with a fixed spatial resolution. The forces on the pseudoparticles due to the calculated fields are then used to update the pseudoparticle velocities, and these velocities are then used to update the pseudoparticle positions. This leads to a scheme which can reproduce the full range of classical micro-scale behaviour of a collection of charged particles.

The EPOCH family of PIC codes is based on the older PSC code written by Harmut Ruhl [111] and retains almost the same core algorithm for the field updates and particle push routines. Two coupled solvers are the core of a PIC code: the particle pusher and the field solver. From the movements of charged particles in space due to the EM fields the currents can be calculated using Maxwell's equations on a fixed spatial grid. Between these two solvers the full collisionless behaviour a kinetic plasma can be simulated.

Maxwell's equations are solved numerically by the finite difference time-domain method (FDTD) with second order terms. For example, the $\partial_x E_y$ is defined as:

$$(\frac{\partial E_y}{\partial x})_{i,j,k} = \frac{E_{y_{i+1,j,k}} - E_{y_{i,j,k}}}{\Delta x} \tag{7.1}$$

where Δx is the distance between cells in the *x*-direction. The EPOCH uses a modified version of the leapfrog scheme in which the field is updated at both the full time-step and the half time-step. Firstly, the fields are advanced one half time-step from n to $n+1/2$:

$$\mathbf{E}^{n+\frac{1}{2}} = \mathbf{E}^{n} + \frac{\Delta t}{2}(c^2\nabla \times \mathbf{B}^{n} - \frac{\mathbf{J}^{n}}{\epsilon_0}) \tag{7.2}$$

$$\mathbf{B}^{n+\frac{1}{2}} = \mathbf{B}^{n} - \frac{\Delta t}{2}(\Delta \times \mathbf{E}^{n+\frac{1}{2}}) \tag{7.3}$$

At this stage, the current is uploaded to $\mathbf{J}^{n+1}$ by the particle pusher and the fields are updated from $n+1/2$ to $n+1$ to complete the step:

$$\mathbf{B}^{n+1} = \mathbf{B}^{n+\frac{1}{2}} - \frac{\Delta t}{2}(\Delta \times \mathbf{E}^{n+\frac{1}{2}}) \tag{7.4}$$

$$\mathbf{E}^{n+1} = \mathbf{E}^{n+\frac{1}{2}} + \frac{\Delta t}{2}(c^2\nabla \times \mathbf{B}^{n+1} - \frac{\mathbf{J}^{n+1}}{\epsilon_0}) \tag{7.5}$$

where Δt is the Courant-Friedrichs-Lewy (CFL) limited time-step. The time-step is restricted to $\Delta t < c^{-1}(\Delta x^{-2} + \Delta y^{-2} + \Delta z^{-2})^{-1/2}$.

The particle pusher solves the relativistic equation of motion under the Lorentz force for each particle in the simulation. In order to calculate the particle trajectory to second order accuracy, the electric and magnetic fields at the half time-step are used after they are calculated in the first half of the Maxwell solver:

$$\boldsymbol{p}_\alpha^{n+1} = \boldsymbol{p}_\alpha^{n} + q_\alpha \Delta t[\mathbf{E}^{n+\frac{1}{2}}(\boldsymbol{x}_\alpha^{n+\frac{1}{2}}) + \boldsymbol{v}_\alpha^{n+\frac{1}{2}} \times \mathbf{B}^{n+\frac{1}{2}}(\boldsymbol{x}_\alpha^{n+\frac{1}{2}}))] \tag{7.6}$$

where $\boldsymbol{p}_\alpha$ is the particle momentum, q_α the particle's charge, $\boldsymbol{x}_\alpha$ the particle position and $\boldsymbol{v}_\alpha$ the particle velocity. The particle velocity can be calculated directly from the particle momentum using $\boldsymbol{p}_\alpha = \gamma_\alpha m_\alpha \boldsymbol{v}_\alpha$, where m_α is the particle mass and $\gamma_\alpha = [(\boldsymbol{p}_\alpha/m_\alpha c)^2 + 1]^{1/2}$.

A binary collision algorithm has been implemented in EPOCH which assumed that the collision frequency between a particle *i* of species α and a particle *j* of species β (with $\alpha = \beta$ possibility) is given by:

$$\nu_{\alpha\beta} \propto \frac{(n_j}{4\pi(\epsilon_0\mu)^2 v_r^3} \tag{7.7}$$

where $\mu = m_\alpha m_\beta/(m_\alpha + m_\beta)$ is the reduced mass, v_r is the relative velocity of *i* and *j* and n_j is the density of particle j. A number of ionisation models are included in EPOCH to account for the different modes by which electrons ionise in the field of an intense laser and through collisions. In 1965, Keldysh derived formulae describing field ionisation for a hydrogen atom in the low frequency regime where the photon energy is beneath the binding energy of the electron. The Keldysh parameter γ is introduced to separate field ionisation into the multi-photon and tunnelling regimes. In Hartree atomic units the Keldysh parameter is given by [65]:

$$\gamma = \frac{\omega\sqrt{2m_e\epsilon}}{eE} \tag{7.8}$$

where ω is the photon frequency, m_e the electron mass, ϵ the ionisation energy for the electron, *e* the electron charge, and *E* the magnitude of the electric field at the electron. When an electron absorbs a photon that does not have enough energy to cause ionisation or excitation to a higher energy state, multi-photon ionisation ($\gamma \gg 1$) occurs. In this case electrons can be excited to virtual energy states and it is possible for electrons to absorb further photons and ionise before the virtual states decay. Tunnelling ionisation ($\gamma \ll 1$) considers the deformation of the atomic Coulomb potential by the imposed electric field which can create a finite potential energy barrier through which electrons may tunnel. EPOCH models multi-photon ionisation with a semi-empirical WKB approximation [66] and tunnelling ionisation with ADK ionisation rate equation[67].

The simulations shown in this work have been carried out on the HPC cluster of the “Centre for Information and Media Technology” (ZIM) at the Heinrich Heine University of Düsseldorf (Germany). The HPC-System “HILBERT” consists of a Shared-Memory-Part (SGI UV2000 Intel Xeon with 512 Cores and 16 TByte RAM) and a MPI-Part (Bull INCA Intel Xeon with 2688 Cores and 128 GByte RAM each node).

Depending on the simulation resolution, size and the number of particles chosen, the computational time of the simulations varied from a few hours to a few days and most of the results are in a 2 dimensional geometry due to the computational restriction.

Bibliography

[1] M. Tabak, J. Hammer, M. E. Glinsky, W. L. Kruer, S. C. Wilks, J. Woodworth, E. M. Campbell, M. D. Perry, and R. J. Mason, *Ignition and high gain with ultrapowerful lasers*, Phys. Plasmas **1**, 1626–1634 (1994).

[2] R. Kodama, P. Norreys, K. Mima, A. Dangor, R. Evans, H. Fujita, Y. Kitagawa, K. Krushelnick, T. Miyakoshi, N. Miyanaga, *et al.*, *Fast heating of ultrahigh-density plasma as a step towards laser fusion ignition*, Nature **412**, 798–802 (2001).

[3] S. Wilks, A. Langdon, T. Cowan, M. Roth, M. Singh, S. Hatchett, M. Key, D. Pennington, A. MacKinnon, and R. Snavely, *Energetic proton generation in ultra-intense laser–solid interactions*, Phys. Plasmas **8**, 542–549 (2001).

[4] H. Daido, M. Nishiuchi, and A. S. Pirozhkov, *Review of laser-driven ion sources and their applications*, Rep. Prog. Phys. **75**, 056401 (2012).

[5] J. Fuchs, Y. Sentoku, S. Karsch, J. Cobble, P. Audebert, A. Kemp, A. Nikroo, P. Antici, E. Brambrink, A. Blazevic, *et al.*, *Comparison of laser ion acceleration from the front and rear surfaces of thin foils*, Phys. Rev. Lett. **94**, 045004 (2005).

[6] A. Macchi, M. Borghesi, and M. Passoni, *Ion acceleration by superintense laser-plasma interaction*, Rev. Mod. Phys. **85**, 751 (2013).

[7] S. P. Hatchett, C. G. Brown, T. E. Cowan, E. A. Henry, J. S. Johnson, M. H. Key, J. A. Koch, A. B. Langdon, B. F. Lasinski, R. W. Lee, *et al.*, *Electron, photon, and ion beams from the relativistic interaction of Petawatt laser pulses with solid targets*, Phys. Plasmas **7**, 2076–2082 (2000).

[8] M. Allen, P. K. Patel, A. Mackinnon, D. Price, S. Wilks, and E. Morse, *Direct*

experimental evidence of back-surface ion acceleration from laser-irradiated gold foils, Phys. Rev. Lett. **93**, 265004 (2004).

[9] H. Schwoerer, P. Gibbon, S. Düsterer, R. Behrens, C. Ziener, C. Reich, and R. Sauerbrey, *MeV X rays and photoneutrons from femtosecond laser-produced plasmas*, Phys. Rev. Lett. **86**, 2317 (2001).

[10] P. Audebert, R. Shepherd, K. Fournier, O. Peyrusse, D. Price, R. Lee, P. Springer, J.-C. Gauthier, and L. Klein, *Heating of thin foils with a relativistic-intensity short-pulse laser*, Phys. Rev. Lett. **89**, 265001 (2002).

[11] W. Kruer and K. Estabrook, *$J \times B$ heating by very intense laser light*, Phys. Fluids **28**, 430–432 (1985).

[12] T. Nakamura, K. Mima, H. Sakagami, and T. Johzaki, *Electron surface acceleration on a solid capillary target inner wall irradiated with ultraintense laser pulses*, Phys. Plasmas **14**, 053112 (2007).

[13] K. Ledingham, I. Spencer, T. McCanny, R. Singhal, M. Santala, E. Clark, I. Watts, F. Beg, M. Zepf, K. Krushelnick, *et al.*, *Photonuclear physics when a multiterawatt laser pulse interacts with solid targets*, Phys. Rev. Lett. **84**, 899 (2000).

[14] Y. Ping, R. Shepherd, B. Lasinski, M. Tabak, H. Chen, H. Chung, K. Fournier, S. Hansen, A. Kemp, D. Liedahl, *et al.*, *Absorption of short laser pulses on solid targets in the ultrarelativistic regime*, Phys. Rev. Lett. **100**, 085004 (2008).

[15] R. Kodama, H. Shiraga, K. Shigemori, Y. Toyama, S. Fujioka, H. Azechi, H. Fujita, H. Habara, T. Hall, Y. Izawa, *et al.*, *Nuclear fusion: Fast heating scalable to laser fusion ignition*, Nature **418**, 933–934 (2002).

[16] A. Lei, K. Tanaka, R. Kodama, G. Kumar, K. Nagai, T. Norimatsu, T. Yabuuchi, and K. Mima, *Optimum hot electron production with low-density foams for laser fusion by fast ignition*, Phys. Rev. Lett. **96**, 255006 (2006).

[17] Y. Sentoku, K. Mima, H. Ruhl, Y. Toyama, R. Kodama, and T. Cowan, *Laser light and hot electron micro focusing using a conical target*, Phys. Plasmas **11**, 3083–3087 (2004).

[18] H. Sumeruk, S. Kneip, D. Symes, I. Churina, A. Belolipetski, T. D. Donnelly, and T. Ditmire, *Control of strong-laser-field coupling to electrons in solid targets with wavelength-scale spheres*, Phys. Rev. Lett. **98**, 045001 (2007).

[19] S. Kahaly, S. Yadav, W. Wang, S. Sengupta, Z. Sheng, A. Das, P. Kaw, and G. R. Kumar, *Near-complete absorption of intense, ultrashort laser light by sub-λ gratings*, Phys. Rev. Lett. **101**, 145001 (2008).

[20] G.-y. Hu, J.-w. Wang, L.-g. Huang, W.-t. Wang, X. Wang, Y. Xu, B.-f. Shen, J.-s. Liu, W. Yu, R.-x. Li, *et al.*, *Enhanced surface acceleration of fast electrons by using subwavelength grating targets*, Phys. Plasmas **17**, 083102 (2010).

[21] A. Macchi, *A Superintense Laser-Plasma Interaction Theory Primer* (Springer Science & Business Media, 2013).

[22] P. Gibbon, *Short pulse laser interactions with matter* (World Scientific Publishing Company, 2004).

[23] W. L. Kruer, *The physics of laser plasma interactions* (Addison-Wesley Publishing Co., 1988).

[24] P. Mulser and D. Bauer, *High power laser-matter interaction*, Vol. 238 (Springer Science & Business Media, 2010).

[25] C. Riconda, M. Raynaud, T. Vialis, and M. Grech, *Simple scalings for various regimes of electron acceleration in surface plasma waves*, Phys. Plasmas **22**, 073103 (2015).

[26] M. Raynaud, J. Kupersztych, C. Riconda, J. Adam, and A. Heron, *Strongly enhanced laser absorption and electron acceleration via resonant excitation of surface plasma waves*, Phys. Plasmas **14**, 092702 (2007).

[27] A. Sgattoni, L. Fedeli, G. Cantono, T. Ceccotti, and A. Macchi, *High field plasmonics and laser-plasma acceleration in solid targets*, Plasma Phys. Control. Fusion **58**, 014004 (2015).

[28] G. Mie, *Beiträge zur Optik trüber Medien, speziell kolloidaler Metallösungen*, Ann. Phys. (Berlin) **330**, 377–445 (1908).

[29] T. Ceccotti, V. Floquet, A. Sgattoni, A. Bigongiari, O. Klimo, M. Raynaud, C. Riconda, A. Heron, F. Baffigi, L. Labate, *et al.*, *Evidence of resonant surface-wave excitation in the relativistic regime through measurements of proton acceleration from grating targets*, Phys. Rev. Lett. **111**, 185001 (2013).

[30] L. Fedeli, A. Sgattoni, G. Cantono, D. Garzella, F. Réau, I. Prencipe, M. Passoni, M. Raynaud, M. Květoň, J. Proska, *et al.*, *Electron acceleration by relativistic surface plasmons in laser-grating interaction*, Phys. Rev. Lett. **116**, 015001 (2016).

[31] C. Liu, V. Tripathi, X. Shao, and T. Liu, *Nonlinear surface plasma wave induced target normal sheath acceleration of protons*, Phys. Plasmas **22**, 023105 (2015).

[32] M. Roth and M. Schollmeier, *Ion Acceleration?Target Normal Sheath Acceleration*, CERN Yellow Reports **1**, 231 (2016).

[33] V. Yanovsky, V. Chvykov, G. Kalinchenko, P. Rousseau, T. Planchon, T. Matsuoka, A. Maksimchuk, J. Nees, G. Cheriaux, G. Mourou, *et al.*, *Ultra-high intensity-300-TW laser at 0.1 Hz repetition rate.*, Opt. Express **16**, 2109–2114 (2008).

[34] L. D. Landau, *The classical theory of fields*, Vol. 2 (Elsevier, 2013).

[35] A. Di Piazza, *Exact solution of the Landau-Lifshitz equation in a plane wave*, Lett. Math. Phys. **83**, 305–313 (2008).

[36] C. K. Birdsall and A. B. Langdon, *Plasma physics via computer simulation* (CRC Press, 2004).

[37] J. M. Dawson, *Particle simulation of plasmas*, Rev. Mod. Phys. **55**, 403 (1983).

[38] J. D. Jackson, *Classical electrodynamics* (Wiley, 1999).

[39] P. Catto and R. M. More, *Sheath inverse bremsstrahlung in laser produced plasmas*, Phys. Fluids **20**, 704 (1977).

[40] T. M. Wilks SC, Kruer WL and L. AB, *Absorption of ultra-intense laser pulses*, Phys. Rev. Lett. **69**, 1383 (1992).

[41] H. Ruhl and P. Mulser, *Relativistic Vlasov simulation of intense fs laser pulse-matter interaction*, Phys. Lett. A **205**, 388–392 (1995).

[42] T. Nakamura, S. Kato, H. Nagatomo, and K. Mima, *Surface-magnetic-field and fast-electron current-layer formation by ultraintense laser irradiation*, Phys. Rev. Lett. **93**, 265002 (2004).

[43] M. Chen, Z.-M. Shenga, J. Zheng, Y.-Y. Ma, M. A. Bari, Y.-T. Li, and J. Zhang, *Surface electron acceleration in relativistic laser-solid interactions*, Opt. Express **14**, 3093–3098 (2006).

[44] S. Braginskii, *Transport processes in a plasma*, Rev. Plasma Phys. **1**, 205 (1965).

[45] M. E. Glinsky, *Regimes of suprathermal electron transport*, Phys. Plasmas **2**, 2796–2806 (1995).

[46] R. Mason, *Monte Carlo (hybrid) suprathermal electron transport*, Phys. Rev. Lett. **43**, 1795 (1979).

[47] D. Bond, J. Hares, and J. Kilkenny, *Demonstration of resistive inhibition of fast electrons from laser-produced plasmas in low-density gold targets*, Phys. Rev. Lett. **45**, 252 (1980).

[48] A. Bell, J. Davies, S. Guerin, and H. Ruhl, *Fast-electron transport in high-intensity short-pulse laser-solid experiments*, Plasma Phys. Control. Fusion **39**, 653 (1997).

[49] R. L. Dewar and J. Lindl, *Nonlinear frequency shift of a plasma wave*, Phys. Fluids **15**, 820–824 (1972).

[50] E. Clark, K. Krushelnick, M. Zepf, F. Beg, M. Tatarakis, A. Machacek, M. Santala, I. Watts, P. Norreys, and A. Dangor, *Energetic heavy-ion and proton generation from ultraintense laser-plasma interactions with solids*, Phys. Rev. Lett. **85**, 1654 (2000).

[51] R. Snavely, M. Key, S. Hatchett, T. Cowan, M. Roth, T. Phillips, M. Stoyer, E. Henry, T. Sangster, M. Singh, *et al.*, *Intense high-energy proton beams from petawatt-laser irradiation of solids*, Phys. Rev. Lett. **85**, 2945 (2000).

[52] A. Maksimchuk, S. Gu, K. Flippo, D. Umstadter, and V. Y. Bychenkov, *Forward ion acceleration in thin films driven by a high-intensity laser*, Phys. Rev. Lett. **84**, 4108 (2000).

[53] G. Marx, *Interstellar vehicle propelled by terrestrial laser beam*, Nature **211** (1966).

[54] J. Simmons and C. McInnes, *Was Marx right? or How efficient are laser driven interstellar spacecraft?*, Am. J. Phys. **61**, 205–207 (1993).

[55] A. Robinson, M. Zepf, S. Kar, R. Evans, and C. Bellei, *Radiation pressure acceleration of thin foils with circularly polarized laser pulses*, New J. Phys. **10**, 013021 (2008).

[56] A. Giesecke, *Propagation Dynamics and High Harmonic Generation Using High Contrast Ultrashort Laser Pulses*, Ph.D. Dissertation, Heinrich-Heine-Universität Düsseldorf (2013).

[57] M. Cerchez, *Ultrashort laser pulse interaction with overdense plasmas*, Ph.D. Dissertation, Heinrich-Heine-Universität Düsseldorf (2008).

[58] C. Freeman, G. Fiksel, C. Stoeckl, N. Sinenian, M. Canfield, G. Graeper, A. Lombardo, C. Stillman, S. Padalino, C. Mileham, *et al.*, *Calibration of a Thomson parabola ion spectrometer and Fujifilm imaging plate detectors for protons, deuterons, and alpha particles*, Rev. Sci. Instrum. **82**, 073301 (2011).

[59] N. Izumi, R. Snavely, G. Gregori, J. Koch, H.-S. Park, and B. Remington, *Application of imaging plates to x-ray imaging and spectroscopy in laser plasma experiments*, Rev. Sci. Instrum. **77**, 10E325 (2006).

[60] B. Hidding, G. Pretzler, M. Clever, F. Brandl, F. Zamponi, A. Lübcke, T. Kämpfer, I. Uschmann, E. Förster, U. Schramm, *et al.*, *Novel method for characterizing relativistic electron beams in a harsh laser-plasma environment*, Rev. Sci. Instrum. **78**, 083301 (2007).

[61] K. A. Tanaka, T. Yabuuchi, T. Sato, R. Kodama, Y. Kitagawa, T. Takahashi, T. Ikeda, Y. Honda, and S. Okuda, *Calibration of imaging plate for high energy electron spectrometer*, Rev. Sci. Instrum. **76**, 013507 (2005).

[62] B. Hidding, *En route: Elektronenbeschleuniger der nächsten generation auf laser-plasma-basis*, Ph.D. Dissertation, Heinrich-Heine-Universität, Düsseldorf (2008).

[63] A. Taniyama, D. Shindo, and T. Oikawa, *Detective quantum efficiency of the 25 μm pixel size Imaging Plate for transmission electron microscopes*, J. Electron Microsc. **46**, 303–310 (1997).

[64] I. Choi, C. Kim, J. Sung, T. Yu, S. Lee, I. Kim, Y.-Y. Jin, T. Jeong, N. Hafz, K. Pae, *et al.*, *Ion spectrometer composed of time-of-flight and Thomson parabola spectrometers for simultaneous characterization of laser-driven ions*, Rev. Sci. Instrum. **80**, 053302 (2009).

[65] L. Keldysh *et al.*, *Ionization in the field of a strong electromagnetic wave*, Sov. Phys. JETP **20**, 1307–1314 (1965).

[66] N. B. Delone and V. Krainov, *Multiphoton processes in atoms*, Vol. 13 (Springer Science & Business Media, 2012).

[67] M. Ammosov, N. Delone, V. Krainov, A. Perelomov, V. Popov, M. Terent'ev, G. L. Yudin, and M. Y. Ivanov, *Tunnel ionization of complex atoms and of atomic ions in an alternating electric field*, Sov. Phys. JETP **64**, 1191–1194 (1987).

[68] D. Margarone, O. Klimo, I. Kim, J. Prokupek, J. Limpouch, T. Jeong, T. Mocek, J. Psikal, H. Kim, J. Proska, *et al.*, *Laser-driven proton acceleration enhancement by nanostructured foils*, Phys. Rev. Lett. **109**, 234801 (2012).

[69] M. Kuzelev, R. Romanov, A. Rukhadze, and N. Khundzhua, *Surface waves and space charge layers in a spatially inhomogeneous plasma*, Plasma Phys. Rep. **33**, 982–989 (2007).

[70] F. Zheng, S. Wu, H. Zhang, T. Huang, M. Yu, C. Zhou, and X. He, *Preplasma effects on the generation of high-energy protons in ultraintense laser interaction with foil targets*, Phys. Plasmas **20**, 123105 (2013).

[71] V. Ovchinnikov, D. Schumacher, M. McMahon, E. Chowdhury, C. Chen, A. Morace, and R. Freeman, *Effects of preplasma scale length and laser intensity on the divergence of laser-generated hot electrons*, Phys. Rev. Lett. **110**, 065007 (2013).

[72] R. Nuter, L. Gremillet, P. Combis, M. Drouin, E. Lefebvre, A. Flacco, and V. Malka, *Influence of a preplasma on electron heating and proton acceleration in ultraintense laser-foil interaction*, J. Appl. Phys. **104**, 103307 (2008).

[73] S. Atzeni, A. Schiavi, J. Honrubia, X. Ribeyre, G. Schurtz, P. Nicolai, M. Olazabal-Loumé, C. Bellei, R. Evans, and J. Davies, *Fast ignitor target studies for the HiPER projecta)*, Phys. Plasmas **15**, 056311 (2008).

[74] M. Hegelich, S. Karsch, G. Pretzler, D. Habs, K. Witte, W. Guenther, M. Allen, A. Blazevic, J. Fuchs, J. Gauthier, *et al.*, *MeV ion jets from short-pulse-laser interaction with thin foils*, Phys. Rev. Lett. **89**, 085002 (2002).

[75] M. Roth, A. Blazevic, M. Geissel, T. Schlegel, T. Cowan, M. Allen, J.-C. Gauthier, P. Audebert, J. Fuchs, J. Meyer-ter Vehn, *et al.*, *Energetic ions generated by laser pulses: A detailed study on target properties*, Phys. Rev. Spec. Top. AC **5**, 061301 (2002).

[76] E. Lefebvre and G. Bonnaud, *Transparency/opacity of a solid target illuminated by an ultrahigh-intensity laser pulse*, Phys. Rev. Lett. **74**, 2002 (1995).

[77] E. d'Humières, E. Lefebvre, L. Gremillet, and V. Malka, *Proton acceleration mechanisms in high-intensity laser interaction with thin foils*, Phys. Plasmas **12**, 062704 (2005).

[78] J. Santos, F. Amiranoff, S. Baton, L. Gremillet, M. Koenig, E. Martinolli, M. R. Le Gloahec, C. Rousseaux, D. Batani, A. Bernardinello, *et al.*, *Fast electron transport in ultraintense laser pulse interaction with solid targets by rear-side self-radiation diagnostics*, Phys. Rev. Lett. **89**, 025001 (2002).

[79] H. Nishimura, Y. Inubushi, M. Ochiai, T. Kai, T. Kawamura, S. Fujioka, M. Hashida, S. Simizu, S. Sakabe, R. Kodama, *et al.*, *Study of fast electron transport in hot dense matter using x-ray spectroscopy*, Plasma Phys. Control. Fusion **47**, B823 (2005).

[80] J. Fuchs, T. Cowan, P. Audebert, H. Ruhl, L. Gremillet, A. Kemp, M. Allen, A. Blazevic, J.-C. Gauthier, M. Geissel, *et al.*, *Spatial uniformity of laser-accelerated ultrahigh-current MeV electron propagation in metals and insulators*, Phys. Rev. Lett. **91**, 255002 (2003).

[81] A. Mackinnon, Y. Sentoku, P. Patel, D. Price, S. Hatchett, M. Key, C. Andersen, R. Snavely, and R. Freeman, *Enhancement of proton acceleration by hot-electron recirculation in thin foils irradiated by ultraintense laser pulses*, Phys. Rev. Lett. **88**, 215006 (2002).

[82] J. Myatt, W. Theobald, J. Delettrez, C. Stoeckl, M. Storm, T. Sangster, A. Maximov, and R. Short, *High-intensity laser interactions with mass-limited solid targets and implications for fast-ignition experiments on OMEGA EPa)*, Phys. Plasmas **14**, 056301 (2007).

[83] H. Chen and S. C. Wilks, *Evidence of enhanced effective hot electron temperatures in ultraintense laser-solid interactions due to reflexing*, Laser Part. Beams **23**, 411–416 (2005).

[84] D. Forslund and J. Brackbill, *Magnetic-field-induced surface transport on laser-irradiated foils*, Phys. Rev. Lett. **48**, 1614 (1982).

[85] S. Buffechoux, J. Psikal, M. Nakatsutsumi, L. Romagnani, A. Andreev, K. Zeil, M. Amin, P. Antici, T. Burris-Mog, A. Compant-La-Fontaine, *et al.*, *Hot electrons transverse refluxing in ultraintense laser-solid interactions*, Phys. Rev. Lett. **105**, 015005 (2010).

[86] H. Bichsel, *Straggling in thin silicon detectors*, Rev. Mod. Phys. **60**, 663 (1988).

[87] P. McKenna, D. Carroll, R. Clarke, R. Evans, K. Ledingham, F. Lindau, O. Lundh, T. McCanny, D. Neely, A. Robinson, *et al.*, *Lateral electron transport in high-intensity laser-irradiated foils diagnosed by ion emission*, Phys. Rev. Lett. **98**, 145001 (2007).

[88] A. Modena, Z. Najmudin, A. Dangor, C. Clayton, K. Marsh, C. Joshi, V. Malka, C. Darrow, C. Danson, D. Neely, *et al.*, *Electron acceleration from the breaking of relativistic plasma waves*, Nature **377**, 606–608 (1995).

[89] M. M. Murnane, H. C. Kapteyn, *et al.*, *Ultrafast X-ray pulses from laser-produced plasmas*, Science **251**, 531 (1991).

[90] M. Cerchez, R. Jung, J. Osterholz, T. Toncian, O. Willi, P. Mulser, and H. Ruhl, *Absorption of ultrashort laser pulses in strongly overdense targets*, Phys. Rev. Lett. **100**, 245001 (2008).

[91] M. Murnane, H. Kapteyn, S. Gordon, J. Bokor, E. Glytsis, and R. Falcone, *Efficient coupling of high-intensity subpicosecond laser pulses into solids*, Appl. Phys. Lett. **62**, 1068–1070 (1993).

[92] T. Nishikawa, H. Nakano, N. Uesugi, M. Nakao, and H. Masuda, *Greatly enhanced soft x-ray generation from femtosecond-laser-produced plasma by using a nanohole-alumina target*, Appl. Phys. Lett. **75**, 4079 (1999).

[93] G. Kulcsar, D. AlMawlawi, F. Budnik, P. Herman, M. Moskovits, L. Zhao, and R. Marjoribanks, *Intense picosecond X-ray pulses from laser plasmas by use of nanostructured ?velvet? targets*, Phys. Rev. Lett. **84**, 5149 (2000).

[94] P. Rajeev and G. R. Kumar, *Polarization independent hot electron production from modulated solid surfaces*, Opt. Commun. **222**, 9–15 (2003).

[95] W. Rozmus and V. Tikhonchuk, *Skin effect and interaction of short laser pulses with dense plasmas*, Phys. Rev. A **42**, 7401 (1990).

[96] F. Brunel, *Not-so-resonant, resonant absorption*, Phys. Rev. Lett. **59**, 52 (1987).

[97] D. Bergström, J. Powell, and A. Kaplan, *A ray-tracing analysis of the absorption of light by smooth and rough metal surfaces*, J. Appl. Phys. **101**, 113504 (2007).

[98] A. Andreev and K. Y. Platonov, *Interaction of Ultra High Intensity Laser Pulse with Structured Target and Fast Particle Generation in a Stable Mode*, Contrib. Plasma Phys. **53**, 173–178 (2013).

[99] A. Andreev, N. Kumar, K. Platonov, and A. Pukhov, *Efficient generation of fast ions from surface modulated nanostructure targets irradiated by high intensity short-pulse lasers*, Phys. Plasmas **18**, 103103 (2011).

[100] M. Cerchez, M. Swantusch, M. Toncian, T. Toncian, O. Willi, C. Rodel, O. Jackel, G. Paulus, and A. Andreev, *Enhanced energy absorption of high intensity laser pulses by modulated target surfaces*, unpublished.

[101] T. Arber, K. Bennett, C. Brady, A. Lawrence-Douglas, M. Ramsay, N. Sircombe, P. Gillies, R. Evans, H. Schmitz, A. Bell, *et al.*, *Contemporary particle-in-cell approach to laser-plasma modelling*, Plasma Phys. Control. Fusion **57**, 113001 (2015).

[102] K. Eidmann, J. Meyer-ter Vehn, T. Schlegel, and S. Hüller, *Hydrodynamic simulation of subpicosecond laser interaction with solid-density matter*, Phys. Rev. E **62**, 1202 (2000).

[103] M. Cerchez, A. Giesecke, C. Peth, M. Toncian, B. Albertazzi, J. Fuchs, O. Willi, and T. Toncian, *Generation of laser-driven higher harmonics from grating targets*, Phys. Rev. Lett. **110**, 065003 (2013).

[104] T. Ma, H. Sawada, P. Patel, C. Chen, L. Divol, D. Higginson, A. Kemp, M. Key, D. Larson, S. Le Pape, *et al.*, *Hot electron temperature and coupling efficiency scaling with prepulse for cone-guided fast ignition*, Phys. Rev. Lett. **108**, 115004 (2012).

[105] H.-S. Park, D. Chambers, H.-K. Chung, R. Clarke, R. Eagleton, E. Giraldez, T. Goldsack, R. Heathcote, N. Izumi, M. Key, *et al.*, *High-energy Kα radiography using high-intensity, short-pulse lasersa)*, Phys. Plasmas **13**, 056309 (2006).

[106] K. Ivanov, S. Shulyapov, P. Ksenofontov, I. Tsymbalov, R. Volkov, A. Savel'ev, A. Brantov, V. Y. Bychenkov, A. Turinge, A. Lapik, *et al.*, *Comparative study of amplified spontaneous emission and short pre-pulse impacts onto fast electron generation at sub-relativistic femtosecond laser-plasma interaction*, Phys. Plasmas **21**, 093110 (2014).

[107] K. Tanaka, R. Kodama, H. Fujita, M. Heya, N. Izumi, Y. Kato, Y. Kitagawa, K. Mima, N. Miyanaga, T. Norimatsu, *et al.*, *Studies of ultra-intense laser plasma interactions for fast ignition*, Phys. Plasmas **7**, 2014–2022 (2000).

[108] S. Baton, M. Koenig, J. Fuchs, A. Benuzzi-Mounaix, P. Guillou, B. Loupias, T. Vinci, L. Gremillet, C. Rousseaux, M. Drouin, *et al.*, *Inhibition of fast electron energy deposition due to preplasma filling of cone-attached targets*, Phys. Plasmas **15**, 042706 (2008).

[109] A. Pukhov, Z.-M. Sheng, and J. Meyer-ter Vehn, *Particle acceleration in relativistic laser channels*, Phys. Plasmas **6**, 2847–2854 (1999).

[110] A. Andreev, K. Y. Platonov, and R. Salomaa, *Backscattering of ultrashort high intensity laser pulses from solid targets at oblique incidence*, Phys. Plasmas **9**, 581–588 (2002).

[111] H. Ruhl, *Classical Particle Simulations with the PSC code*, Ruhr-Universität Bochum (2005).

[112] H. Bethe, *Moliere's theory of multiple scattering*, Phys. Rev. **89**, 1256 (1953).

Acknowledgement

The writing and completion of this Dissertation would not have been possible without the assistance, support and guidance of a few very special people in my life. First of all, I would like to express my sincere gratitude to my supervisor Prof. Dr. Oswald Willi for offering me this great opportunity to work in this interesting research field. I am deeply grateful to his continuous support and careful supervision over these years. Secondly, thanks to Prof. Dr. Alexander Pukhov for being the second referee. I am also grateful to Prof. Alexander Andreev for shedding a new light on the interpretation of the results.

I owe my deepest gratitude to Dr. Mirela Cerchez for her invaluable and never-ending support in the lab and in general.

Thanks a lot to my colleagues who shared time with me in the bunker and/or laser room and contributed to the results of the experiments: Dr. Rajendra Prasad, Dr. Bastian Aurand, Marco Swantusch, Sven Spickermann, Stephanie Brauckmann, Anna-Marie Schroer, Marius Blecher and also my friend Kunaree Wongrach. Working in such a lovely group is full of unforgettable memories.

I would like to acknowledge the support from the team operating the ARCTURUS laser: Monika Toncian, Dr. Toma Toncian, Farzan Hamzehei and Thomas Wowra.

My special thanks go to the secretary team and especially Claudia Dingle and Katherina Lanzer.

Last but not least, I would like to thank my family. The biggest acknowledgement to my husband, Hengyi. He gives me the never-ending courage, patience and support at each stage of this long journey, and enables me overcome the most persistent obstacles during thesis completion.

I dedicate this thesis to my beloved daughter Nennen. She is such a sweetheart, cheers me up, lights up my life and makes all these things meaningful.

Die hier vorgelegte Dissertation habe ich eigenständig und ohne unerlaubte Hilfe angefertigt. Die Dissertation wurde in der vorgelegten oder in ähnlicher Form noch bei keiner anderen Institution eingereicht. Ich habe bisher keine erfolglosen Promotionsversuche unternommen.

Düsseldorf, 03.03.2017

(Xiaoming Zhu)

List of Figures

List of Tables